

UNIVERSITY OF CINCINNATI

Date: _____

I, _____,
hereby submit this work as part of the requirements for the degree of:

in:

It is entitled:

This work and its defense approved by:

Chair: _____

The Development of Semi-Analytical Solutions for 3-D Contact Problems

A dissertation submitted to the

Division of Research and Advanced Studies
of the University of Cincinnati

In partial fulfillment of the
requirements for the degree of

DOCTORATE OF PHILOSOPHY

In the Department of Mechanical, Industrial
and Nuclear Engineering
Of the College of Engineering

2004

by

Junshan Li

M.S., Beijing University of Aeronautics and Astronautics, 1990

B.S., Nanjing University of Aeronautics and Astronautics, 1984

Committee Chair: Dr. Edward J. Berger

Abstract

The dissertation is to address the need, in contact mechanics, of efficient and effective solutions to certain 3-D contact problems. The solutions developed here are based on underlying analytical solutions to pyramidal loading elements. This feature, along with other characteristics, distinguishes this method from other numerical solutions. The research work is logically divided into three subsequent parts, each of which addresses a particular aspect of the project:

- (1) Developed analytical solution sets in closed form to pyramidal loading profiles. First, a set of Boussinesq-Curruti equations to linear/bilinear distribution of normal and tangential loading over a triangular area are derived and evaluated. Second, solution sets to normal and tangential surface loading pyramids are constructed. The work provides a solution set to a basic loading element, which is the foundation of the development of effective and efficient semi-analytical solutions to 3-D contact problems with general geometry and loading profile.
- (2) Developed a semi-analytical approach (non-incremental algorithm) to 3-D normal contact problems with friction. This approach treats normal contact (indentation) phenomenon as a static problem. Based on fully

coupled governing equations, the algorithm of contact detecting and stick/slip partitioning is designed as nested iterations, to fulfill contact boundary conditions. The computation shows that it is an efficient algorithm. Numerical examples are presented to show the accuracy and efficiency of the method.

- (3) Developed a semi-analytical approach (incremental algorithm) to 3-D contact problems with friction. This approach treats contact as a dynamic problem. The general dynamic models are simplified into quasi-static models in many practical cases that inertial force can be ignored. The incremental algorithm is designed to solve the quasi-static problems. The computation shows that the algorithm works very well for cases featuring both similar and dissimilar materials. Results are favorably compared with Mindlin's analytical solution, Munisamy's approach for axisymmetric contact subject to shear forces. Nowell's analytical approach for 2-D case is used for comparison in an analogous manner.

Computational practice shows that the semi-analytical approaches are efficient and robust, yielding very good results. They have wide range of potential applications.

Copy Right © 2004, Junshan Li, All Right Reserved

Acknowledgement

I would take this opportunity to express my sincerest gratitude to my advisor and dissertation committee chair, Dr. Edward J. Berger, for his consistent support, encouragement, and guidance through the entire dissertational research. I have been benefited from his knowledge and insight, commitment and positive attitude towards work, willingness to provide help and advise in my graduate study at University of Cincinnati.

I am grateful to my dissertation supervisory committee, Dr. Ronald L. Huston, Dr. Yijun Liu and Dr. Kumar Vemaganti. They have been always supportive to my dissertational research, providing me valuable suggestions, advises, and taking time to review my documents. Sincere thanks goes to the Department of Mechanical, Industrial and Nuclear Engineering and University Research Council for the financial supports.

Most of all, I am very grateful to my wife, Juncheng Tang, for her love, care, and long term understanding and support. I am deeply in debt to my family, the dissertation would be impossible without their patience and encouragement. Thanks also go to my parents, for their support to my education pursuit since I was a child.

Table of Contents

Table of Contents	(1)
List of Figures	(6)
List of Tables	(10)
Part I Introduction and Literature Review	(11)
Chapter 1. Introduction	(12)
Chapter 2 Literature Review on the Research Project	(16)
2.1 Theoretical Research on Contact Problems	(16)
2.1.1 Frictional Contact.....	(16)
2.1.2 Arbitrary Surface Traction Distributions or Arbitrary Surface Shapes	(19)
2.2 Numerical Approaches on 3-D Contact Problems.....	(21)
2.2.1 FEM, BEM, Mesh-free and Other Numerical Methods	(21)
2.2.2 Non-Incremental versus Incremental Algorithm.....	(22)
2.2.3 Existence and Uniqueness Issue	(23)
Part II A Study on Elasticity --- the Analytical Solution in Closed Form to a Pyramid Surface Loading Profile	(25)
Chapter 3 Elastic Solution to a Concentrated Load and Distributed Loads ...	(27)

3.1 Potential Functions	(28)
3.2 Displacement Field in Terms of Potential Function.....	(30)
3.2.1 Concentrated Force P Normal to the Surface Only (z-Direction) ...	(30)
3.2.2 Concentrated Tangential Force Q_x Only (x-Direction)	(31)
3.3 The Surface Displacements Produced by the Distribution of Surface Tractions	(32)
3.3.1 Distribution of Normal Pressure over Area S Only	(32)
3.3.2 Distribution of Tangential Loading over Area S Only	(32)
Chapter 4 The Surface Displacements Due To Distribution of Surface Tractions Over a Triangular Area	(34)
4.1 Integration Technique over a Triangular Area.....	(34)
4.1.1 Geometry and Notation	(34)
4.1.2 The Consistency of Formulae.....	(37)
4.1.3 The Notation of Various Integrals	(39)
4.2 Displacement Field Due To a Distribution of Normal Pressure $P(\xi, \eta)$ Over Sub-Triangle Δ_i	(40)
4.2.1 Constant $P(\xi, \eta) = 1$	(40)
4.2.2 Linear Distribution $P(\xi, \eta) = y - \eta$	(40)
4.2.3 Bilinear Distribution $P(\xi, \eta) = (x - \xi)(y - \eta)$	(41)
4.3 Displacement Field Due To Tangential Pressure $Q_x(\xi, \eta)$ over Sub-Triangle Δ_i	(42)

4.3.1 Constant $Q_x(\xi, \eta) = 1$	(42)
4.3.2 Linear Distribution $Q_x(\xi, \eta) = y - \eta$	(42)
4.3.3 Bilinear Distribution $Q_x(\xi, \eta) = (x - \xi)(y - \eta)$	(43)
4.4 The Applications of the Solutions	(44)
4.5 The Evaluations of Various Integrals over Sub-Triangles	(45)
Chapter 5 Surface Displacement Solution Set Due to a Pyramidal Load Profile	(49)
5.1 Coordinate System.....	(49)
5.2 The Development of Solutions to a Normal Pyramidal Load Element ...	(54)
5.2.1 Normal Tetrahedral Pressure Distribution on Equilateral Triangle Base.....	(54)
5.2.2 Normal Pyramidal Pressure Distribution on Hexagonal Base.....	(59)
5.3 The Development of Solutions to a Tangential Pyramidal Load Element	(61)
5.3.1 The Solution to Tetrahedral Element No.1 on an Equilateral Base .	(61)
5.3.2 The Solution to Tetrahedral Element No.2 on an Equilateral Base .	(63)
5.3.3 The Solution to Tetrahedral Element No.6 on an Equilateral Base .	(64)
5.3.4 Construction of Solution to Tangential Pyramidal Load Element ..	(65)
Chapter 6 Discussion and Conclusion	(68)
 Part III The Development of a Semi-Analytical Approach to 3-D Frictional Normal Contact Problem --- Non-Incremental Algorithm	(71)

Chapter 7 Introduction.....	(72)
7.1 Contact Model	(72)
7.2 The Technique of Overlapping Load Elements.....	(73)
Chapter 8 Algorithms for Contact Area Detecting, Stick/Slip Zone Partitioning, and Field Variables Computation.....	(78)
8.1 Surface Displacements Due to Normal Traction.....	(81)
8.2 Surface Displacements Due to Tangential Traction.....	(82)
8.3 Governing Equations for a Point to Fall within the Contact Area.....	(83)
8.4 Governing Equations for a Point to Fall into Sticking Area	(86)
8.5 Discrete Equations	(89)
8.6 Numerical Approach.....	(91)
Chapter 9 Numerical Examples	(95)
9.1 Normal Contact of Elastic Spheres Without Friction.....	(95)
9.2 Normal Contact of Elastic Spheres With Friction	(99)
9.3 Contact of Crossed Elastic Cylinders	(101)
Chapter 10 Discussion and Conclusion.....	(105)
 Part IV The Development of a Semi-Analytical Approach to 3-D Frictional Contact Problem with Tangential Load --- Incremental Algorithm	 (110)
Chapter 11 Modeling of Frictional Contact.....	(111)
11.1 Elastodynamic Model.....	(111)

11.2 Quasi-Static Model.....	(114)
11.3 Contact Conditions on Contact Boundary	(115)
11.4 Incremental Model.....	(118)
Chapter 12 The Incremental Algorithm for Contact Boundary Problems	(121)
12.1 The Derivation of Contact Model for Two Elastic Bodies.....	(121)
12.2 Algorithms for Contact Area Detecting, Stick/Slip Zone Partitioning, and Field Variables Computation	(123)
12.3 Discrete Equations and Numerical Approach.....	(128)
12.3.1 Iteration on Expanding Contact Area	(129)
12.3.2 Iteration on Shrinking Contact Area	(130)
12.3.3 Iteration on Partitioning Stick / Slip Zone.....	(131)
Chapter 13 Numerical Examples	(134)
13.1 Contact Problem with Similar Materials	(135)
13.1.1 Cattaneo-Mindlin's Solution	(135)
13.1.2 Numerical Example	(138)
13.2 Contact Problem with Dissimilar Materials.....	(141)
Chapter 14 Discussion and Conclusion.....	(152)
References.....	(154)

List of Figures

Figure 3.1	The Coordinate System and Senses of Applied Loads.....	(28)
Figure 4.1	The Geometry and Notation of the Loading Triangle.....	(36)
Figure 4.2	The Geometry and Notation of the Sub-Triangle Δ_1	(36)
Figure 4.3	The Convention of Sign of n_i	(37)
Figure 4.4	The Study of Consistency of Formula (a) Point B Is Inside Triangle $A_1A_2A_3$, (b) Point B Is Outside Triangle $A_1A_2A_3$	(38)
Figure 4.5	Loading Elements Assembled from Simpler Triangular Elements: (a) Tetrahedral Element, (b) Pyramidal Element.....	(44)
Figure 5.1	The Coordinate Systems Used in This Part and Subsequent Discuss. Note: the x-y Coordinate System Is NOT Orthogonal, But $\pi/3$ Apart. Coordinate (ξ, η) Are Defined for the Contact Area Only, Which Has the Same Orientation as X-Y System	(51)
Figure 5.2.	A Linear Loading Profile over an Equilateral Triangle Base: (a) Tetrahedral Pressure Distribution, (b) Linear Loading Profile in η	(55)
Figure 5.3	The Geometry and Notation of Equilateral Triangular Base.....	(56)
Figure 5.4	(a) The Pyramid Consists of Six Tetrahedrons; (b) The Hexagonal Base Consists of Six Equilateral Triangles.....	(58)

- Figure 5.5 (a) The Tangential Pyramidal Load Element Consists of Six Tetrahedrons; (b) The Hexagonal Base Consists of Six Equilateral Triangles(62)
- Figure 5.6 Displacement Profiles Due to a Single Pyramidal Load profile (Arbitrary Vertical Scaling): (a, b) Surface Displacements Due to Normal Load Pyramid, (c, d) Surface Displacements Due to Tangential Load Pyramid in X-Direction(67)
- Figure 7.1 The Contact Model to be Solved(72)
- Figure 7.2 Overlapped Pyramidal Load Elements to Approximate C^0 Continuity Loading Profile; Adjacent Load Pyramids with Vertices at (ξ_i, η_j) and (ξ_k, η_m) Have Nodal Pressure values p_{ij} and p_{km} , Respectively(75)
- Figure 7.3 Modeling of Surface Load (a) Concentrated Forces; (b) Piecewise Constant; (c) C^0 Continuity; (d) C^n ($n \geq 1$) Continuity(76)
- Figure 7.4 A Set of Overlapped Triangular Elements Approximates Continuous Surface Load Profile.....(77)
- Figure 8.1 Relationships Among Far-Field Normal Motion Δz , Surface Displacements $\bar{U}_{1,z}$ and $\bar{U}_{2,z}$; Inset: Separation Distance $h(X,Y)$ Measured from the Initial Configuration(85)
- Figure 8.2 Tangential Interface Behavior Showing Points A_1 and A_2 , Originally Coincident, Undergoing Tangential Displacements $\bar{U}_{1,x}$ and $\bar{U}_{1,x}$.

	Sticking Regions Can Be Determined by Considering Interface Displacements Relative to Far-Field Displacements $\delta_{1,x}$ and $\delta_{2,x}$	(89)
Figure 8.3	Flowchart for the Numerical Framework. An Internal Loop over Contact Area (A) Is Nested Within the Stick-slip Region Iteration (B)	(94)
Figure 9.1	Contour Plot of Tangential Interface Traction q_0 for Normal Indentation of Dissimilar Materials (with Friction)	(98)
Figure 9.2	Crossed Cylinder Contact Analysis: (a) Contact Schematic, (b) Ellipse Fitting from Computational Results.....	(101)
Figure 9.3	Crossed Cylinder Contact Results for Contact and Stick Zone Size with $\mu = 0; 0.25; 0.5$ and $\phi = 30^\circ; 45^\circ; 60^\circ; 90^\circ$. Ee is the Curve Fit Error from Equation (9.5)	(102)
Figure 11.1	The Elastodynamic Model	(104)
Figure 11.2	The Contact Problem of Two Infinity Half Spaces.....	(117)
Figure 12.1	The Flowchart of Numerical Framework.....	(132)
Figure 12.2	The Expanding of Contact Area.....	(133)
Figure 13.1	Cattaneo-Mindlin's Solution	(138)
Figure 13.2	Numerical Results Compare with Cattaneo-Minlin's Solution, Along X- Direction.....	(140)
Figure 13.3	The Analytical Solutions for 2-D Cases. (Above) Solution to Dissimilar Materials Obtained from Goodman's Approximation, It	

Shows That the Shape and Location of Stick Zone Change When Tangential Force Is Applied; (Bottom) Mindlin's Solution for Similar Materials (From [Hills, Nowell, and Sackfield, 1993]) ... (142)

Figure 13.4 Initial Tangential Compliance of the Numerical Scheme Compared with Mindlin's Approximation (From [Munisamy, Hill, and Nowell, 1994]). δ_x Is the Bulk Relative Shear Displacement, δ_{mind} Is the Value Given by Mindlin's Approximation. (144)

Figure 13.5 Evolution of Stick Zone for Contact Between Dissimilar Elastic Materials. Dashed Line Corresponds to Normal Loading Alone and Chain Line to a Subsequent Infinitesimal Tangential Force (From [Munisamy, Hill, and Nowell, 1994]) (144)

Figure 13.6 The History of Contact Area and Normal Traction (147)

Figure 13.7 History of Contact and Stick Area, * -- Nodes Immediately Inside Contact Boundary; ∇ -- Nodes Immediately Inside Stick Boundary; Solid Line --- Curve fit of Nodes (148)

Figure 13.8 The Illustration of the Change of Stick Zone (151)

List of Tables

Table 4.1	Displacements in Terms of Applied Normal Load.....	(41)
Table 4.2	Displacements in Terms of Applied Tangential Load.....	(43)
Table 5.1	Entities in Matrix \mathbf{T}_{xy} When α Takes the Value of $n\pi/3$	(53)
Table 8.1	Displacement Fields Due to Unit Pyramid Traction Elements	(79)
Table 8.2	The effect of Poisson's ratio on $G(X, Y, \nu_0)$	(80)
Table 9.1	Properties of Material and Geometries.....	(95)
Table 9.2	Convergence Study, No Friction Case	(97)
Table 9.3	Numerical Result Comparing to Previous Analytical and Numerical Solutions	(100)
Table 13.1	Contact Configuration Data	(139)
Table 13.2	Loading Step.....	(139)
Table 13.3	Contact Configuration Data	(145)
Table 13.4	Loading Step.....	(145)
Table 13.5	Comparison Between Non-incremental, Incremental and Spence Solution.....	(147)

Part I

Introduction and Literature Review

This part presents a thorough literature review concerning the dissertational research project. The literature review highlights the need for efficient and accurate solutions for general 3-D contact problems.

Chapter 1

Introduction

The general problem of compliant bodies in contact with friction remains one of the most difficult areas in elastostatics. The Boussinesq - Cerruti integral equations seem to provide a way to solve any 3-D contact problem. With the contact area known, and the required boundary conditions given, theoretically the solutions can be achieved by integrating these equations. The solutions in closed form, however, are generally unavailable due to the following facts: (i) the normal and tangential surface tractions are fully coupled in Boussinesq - Cerruti integral equations; (ii) the equations can only be evaluated analytically for some very simple contact configuration (geometry and loading profile); (iii) for a contact problem, neither the contact area nor surface traction is known in advance. Therefore, a 3-D contact problem generally requires a numerical solution.

The numerical method for contact analysis fall into one of following category: (i) finite element method (FEM); (ii) boundary element method (BEM); (iii) mesh less method; (iv) various other methods; (v) combinations of more than one method, such as FEM + BEM, BEM + domain decomposition, etc. The FEM has been fully developed; some software packages have the function of contact

analysis, which use gap elements to determine contact area. FEM is believed not good for contact analysis due to the high pressure gradient within contact area. BEM can handle the problem much better; recently some research works using BEM combined with other method give satisfactory result (see literature review). Mesh less method for contact is under development; only a few works have been reported in literature. Most of these methods are quite time consuming, for example, FEM requires lots of computational time, as well as notable human effort for modeling. The accuracy is another concern. Increasing accuracy requires higher element density or element order, and therefore more solution time. The fact motivates the research work to find better numerical solutions. There are some other methods, such as so called domain-decomposition method, Kalker's method for rolling contact, etc, each of which suits some particular situation and yields good result. In order to investigate in detail general 3-D contact area, however, it is still necessary to find efficient numerical solutions.

Although many contact problems can be dealt with using 2-D models, there are still many cases that need to use 3-D models. Therefore, 3-D models are receiving more and more attention. However, 3-D analysis is not a simple extension of 2-D one; it introduces non-linear governing equations in slip zone. This understanding motivates the current research work also.

In the dissertational project, a new computational approach for general 3-D frictional contact problem with non-conformal surfaces has been developed. The method applies to any 3-D non-conforming continuous contact geometry, and explicitly determines sticking and slipping zones in the presence of friction. This approach, which algorithmically follows along the lines discussed in Chapter 5 of Johnson's book [Johnson, 1985], provides a numerical framework for contact problems, which allows easy surface modeling and discretization, as well as a computationally efficient solution of the governing equations. The approach describes the interface tractions using a set of overlapping pyramid load profiles (with hexagonal base) whose boundaries are defined by a background grid on the contact surfaces. A key distinction between this approach and other numerical procedures, including the FEM, BEM, and mesh less methods, is that this method does not require an underlying interpolation scheme for the field variables, rendered unnecessary by the analytical solutions for surface displacements. A numerical iteration scheme has been developed to accurately determine the contact area, to partition the contact area into sticking and slipping zones, and to determine the interface normal and shear tractions. A number of example problems have been examined to verify the accuracy, sensitivity, and convergence behavior of this method, and the numerical results and discussion indicate excellent comparison with analytical solutions, as well as previous numerical ones. The current result shows that the method features high efficiency and high accuracy. The 3-D contact analysis method serves as a basic

research tool for possible future research work, such as contact analysis for coated/layered surfaces, or micro contact mechanics.

The dissertation is organized as follows: The first part of the document is the introduction of dissertational research project and relevant literature review; the second part reports the research work on a topic in elasticity---analytical solutions to linear and bilinear normal and shear loading profile over a triangular base have been achieved in a closed form. Based on this, the normal and tangential pyramid loading profiles have been studied; the solutions are obtained by linear superposition technique. The third part reports the development of a semi-analytical approach to 3-D frictional normal contact problems --- non-incremental algorithm. In this part, an overlapping technique is introduced to approximately achieve C^0 continuity representation of the surface traction distributions. A contact detection and stick/slip-partitioning algorithm have been studied. The fourth part reports the development of another semi-analytical approach to 3-D frictional contact problems --- incremental algorithm. This method has been developed primarily to address a very important characteristic of frictional force: path-dependence. The static friction contact problem with shear (tangential) force existing must be dealt with using either dynamic or quasi-static model. The incremental method is the most accepted method for quasi-static models. In this section, an incremental model has been “derived” from a general dynamic model. The different contact detection and

stick/slip-partitioning algorithm from non-incremental algorithm has been studied.

Chapter 2

Literature Review on the Research Project

2.1 Theoretical Research on Contact Problems

It is well known that Hertz's remarkable work, which founded contact mechanics, was based on a set of somewhat restricted assumptions. Among the six essential assumptions, the most significant ones are frictionless and nonconforming quadratic surface. Over the last century, many important extensions have been achieved to relax Hertz's assumptions, and formed branches of non-Hertzian contact. The relevant achievements are briefly reviewed as follows.

2.1.1 Frictional Contact

The frictional analysis is the most important feature of non-Hertzian contact. In this field, the most important work can be traced back to Cattaneo [Cattaneo, 1938] and Mindlin [Mindlin, 1949]. Cattaneo realized that the contact zone must be divided into regions of slip and regions of stick, in order to fulfill Coulomb's law in a point-wise manner. He solved the three-dimensional contact problem for quadratic surface (as in Hertzian contact) by making a guess of a distribution of tangential traction to fulfill the requirements of displacement field. Mindlin

independently obtained the same result. The experimental work by Mindlin [Mindlin and Dereciwicz, 1953] and Johnson [Johnson, 1955] supported the theory in two respects: the tangential compliance and the appearance of annular slip regions. The discovery of existence of slip zone in contact area is important, because it brought us the understanding of the mechanics of frictional energy dissipation, fretting damage, wear, the formation and growth of cracks, etc.

Cattaneo and Mindlin's solution related c (the radius of stick zone) and a (radius of contact zone) by the relation: $c/a = (1 - Q/\mu P)^{1/2}$ for cylinders in contact, and $c/a = (1 - Q/\mu P)^{1/3}$ for elastic spheres in contact, where P and Q are normal and tangential force respectively, μ is the coefficient of friction. Both normal and tangential traction distributions are symmetric/axisymmetric. However, the solution is only valid for the case that the materials of contacting bodies are similar. Goodman [Goodman, 1962], Hills [Hills and Sackfield, 1987] and Hills, Nowell, et al [Hills, Nowell and Sackfield, 1993] showed that in a dissimilar material case, (1) the slip regions exist even though no tangential force is exerted onto the contacting bodies; (2) surface traction distributions are no longer symmetric as Cattaneo-Mindlin solution predicts. Several other numerical works [Guyot, Kosior and Maurice, 2000], [Kosior, Guyot, and Maurice, 1999] and Li and Berger [Li, Berger, 2002] reach the same conclusion.

The governing equations of contact problems are fully coupled in normal and tangential traction. This makes the equations very difficult to solve even for quadratic surfaces. Goodman [Goodman, 1962] made a simplification to neglect the effect of shear tractions on normal displacements and therefore decoupled one of the governing equations and recovered the Hertzian solution for normal traction. This simplification is often known as the Goodman approximation and is followed by many researchers.

Poisson's ratio is the key factor of decoupling. Ciavarella [Ciavarella, 1998] showed that only when Poisson's ratio ν is 0, as well as Dundurs' constant β (used to measure the dissimilarity of materials) is 0, that the integral equations can be fully decoupled. He also indicated if $\nu \neq 0$, even the Cattaneo-Mindlin solution for Hertzian contact is approximate.

Spence [Spence, 1975] studied the problem of a rigid indenter on an elastic foundation, and derived the stick/slip solution for both flat punch and power law curved indenter. He concluded that the same expression worked for both cases and showed that for monotonic loading, the ratio of stick radius to contact radius c is uniquely determined by the material properties, namely coefficient of friction μ and Poisson's ratio ν . The relation can be applied to the case of two contacting elastic bodies, provided the coefficient γ (a composite material property) is replaced by modified value. This gives the solution more practical values, therefore is often used in indentation analysis.

For years, people have been using Coulomb's law of friction: $q = \pm \mu p$. Oden and his colleagues' work [Oden and Martins, 1984] provided a deeper understanding of frictional contact behavior. On summarizing their experimental work, they proposed a non-local and nonlinear friction laws, usually referred as power law of friction:

$$-\sigma_N = c_N (U_N - g)_+^{m_N} \quad (2.1)$$

where $c_N > 0$, $m_N > 0$ relate to the physical characteristics of the surface. The friction law is then generalized into the form:

$$\begin{cases} |\bar{\sigma}_T| < c_T (u_N - g)_+^{m_T} & \text{then } \dot{u}_T = 0 \\ |\bar{\sigma}_T| = c_T (u_N - g)_+^{m_T} & \text{then } \dot{u}_T = -\lambda \bar{\sigma}_T \text{ for some } \lambda \geq 0 \end{cases} \quad (2.2)$$

The classic Coulomb's law of friction can be retrieved by setting $c_T = \mu c_N$, and $m_T = m_N$.

2.1.2 Arbitrary Surface Traction Distributions or Arbitrary Surface Shapes

Obviously, the non-quadratic surface changes the distribution of tractions; therefore, Hertzian solution is no longer valid. In the real world, the contacting surface and contact region could be arbitrary in shape. To solve the problem requires the extensions to Hertzian solution.

The classical approach to finding stress and displacement solutions due to surface tractions can be tracked back to Boussinesq and Cerruti. They employed the theory of potential to get components of displacement and stress. Boussinesq and Cerruti both obtained solutions to a distributed normal and tangential load over area S on an elastic half space, although their methods are different. The results were presented in Love's book [Love, 1927]. The displacement expressions were given in terms of the integrals of the loading distribution over S . Hence, theoretically, if the distributions of loading within the area S are known explicitly, the displacements and stresses at any point in the solid can be found by evaluating the integrals. Unfortunately, these tools are best suited for simple loading profiles and geometrically easily described loading areas. Non-constant loading (i.e., linear or higher order) and non-elliptic loading areas significantly increase the difficulties and in general prohibit closed form solutions.

Since Boussinesq and Cerruti's work, a number of researchers have tried to resolve these problems. Many attempts involve solutions for simple loading descriptions applied over geometrically simple domains, from which solutions for general loading profiles over general domains can be constructed via superposition. Love [Love, 1929] provided the integral for a rectangular and circular area with constant normal pressure. The solution for first order polynomial load applied to rectangular surface patch has been recently completed by Dydo and Busby [Dydo and Busby, 1995]. The stress and deformation produced by a pressure distribution of the form $P_0 \sqrt{1 - x^2/a^2}$ acting on the rectangle $x = \pm a, y = \pm b$ have been calculated by Kunert (as described in Johnson [Johnson, 1985]). The explicit solution for normal deflection due to a polynomial distribution of pressure acting on a triangular region has been given by Svec and Gladwell [Svec and Gladwell, 1971]. Influence coefficients for the surface normal deflection due to a linear pressure distribution acting on a triangular element has been calculated by Kalker and van Randen [Kalker and van Randen, 1972]. Johnson and Bentall (again as discussed by Johnson [Johnson, 1985]) considered the deflection of a surface under the action of a pyramid distribution of pressure on a uniform hexagonal base.

2.2 Numerical Approaches to 3-D Contact Problems

As addressed in Chapter 1, there has been a need for solutions to general 3-D contact problem, which can not be simplified to be 2-D models. Any extension of Hertzian contact turns out to be difficult to get analytical solution in closed form; therefore, numerical approach to general contact problem becomes essential.

2.2.1 FEM, BEM, Mesh-free and Other Numerical Methods

Campos et al. [Campos, Oden and Kikuchi, 1982] produced a numerical solution to contact problems with friction based upon the finite element method (FEM) and variational inequalities. They used a friction regularization scheme to produce a smooth perturbation of the non-smooth frictional work, and a key result of their numerical solutions is the observation that in the presence of friction, contact area decreases and peak contact normal stress increases as compared to the Hertz (frictionless) solution.

More recent additions to the literature include the works of Kosior, Guyot and Maurice [Kosior, Guyot and Maurice, 1999], [Guyot, Kosior and Maurice, 2000], which present analyses of frictional contact problems using different numerical approaches. One approach [Kosior, Guyot and Maurice, 1999] is based upon the boundary element method (BEM) and enables the total solution to be stated only

in terms of unknown quantities on the contact surface. As a result, computational efficiency can be achieved as compared to domain discretization methods such as the FEM. The second approach [Guyot, Kosior and Maurice, 2000] uses a coupled FEM-BEM approach to study friction contacts, in which the BEM is used to calculate stresses. In each of these two approaches, the numerical results are compared with the Hertz solution (for the frictionless case) and with the analytical solution of Spence [Spence, 1975] for the cases with friction. The agreement in all cases is reasonable, and they also observe a decrease in contact area (and consequent increase in peak normal contact pressure) for the cases with friction, as compared to the frictionless case.

2.2.2 Non-Incremental versus Incremental Algorithm

Due to the non-conservative property of frictional force, in general, any frictional contact problem should be treated using an elastodynamic model. In other words, the frictional contact is a path-dependent problem; all the field variables are functions of time. If the loading time is long enough to neglect inertial force, the elastodynamic model can be simplified to be quasi-static model. The description of such elastodynamic and quasi-static model can be found in Oden's work [Oden and Martins, 1984]. The two methods in literature were considered to solve the quasi-static model: the incremental algorithm and the so called rate problem [Klarbring, 1990]. The latter has mathematical value but not adopted by

any other researchers, and the former is widely accepted by researchers and commercial software packages.

The path dependence issue has been investigated by many researchers. Saeedvafa and Dundurs [Saeedvafa and Dundurs, 1988] extensively examined the path dependent behavior of a contact model. They found out that path dependence occurs when the stick zone expands into slip zone. When slip zone expands into stick zone, the path dependence is very weak. They further partitioned in p - q plane the extremely path-dependent zones and loosely path-dependent zones [Saeedvafa and Dundurs, 1988].

Spense studied power-law indenter contacting with a flat foundation (See 2.1.1). He derived an analytical solution, which related the ratio of stick zone radius to contact area radius to the coefficient of friction and material properties. His work showed that the indentation problems (no global shear force exists) are essentially path-independent, as long as the loading procedure is done monotonically, which is the case in many practical situations.

2.2.3 Existence and Uniqueness Issue

One of the most important characteristics of a numerical solution to a contact problem, which was found in early 1980s and has then been extensively studied,

is the existence and uniqueness issue. As reviewed by Klarbring [Klarbring, 1988], the first example presented in the literature of non-uniqueness of solutions to static frictional contact problems of linear elastic structures was given by Janovsky [Janovsky 1980, 1981]. Since then other examples have been given by Alart and Curnier [Alart and Curnier, 1986], and Mitsopoulou and Doudoumis [Mitsopoulou and Doudoumis, 1987]. The problems studied by these researchers were special cases of the finite-dimensional counterpart of the static friction problem of Duvaut and Lions [Duvaut and Lions, 1976]. Since the load-path-dependent nature of friction was not taken into account, it was suspicious at first that the non-uniqueness was raised by the static assumption. However, later on Klarbring's work [Klarbring, 1984] showed that in the finite-dimensional quasi-static problems non-uniqueness of solutions could also occur. Klarbring further showed [Klarbring, 1987] that in quasi-static problems non-existence of solutions could also occur in certain cases.

Beside above works on finite-dimensional problems, the existence and uniqueness issues have been studied in a wide range. For the continuous static friction problems, Necas et al [Necas et al, 1980], Duvaut [Duvaut, 1980], Jarusek [Jarusek, 1983, 1984], Demkowicz and Oden [Demkowicz and Oden, 1982], Cocu [Cocu, 1984] and Kato [Kato, 1987] made contributions to various contact configuration. For the corresponding quasi-static problems, Klarbring et al [Klarbring et al, 1988, 1989] and Andersson [Andersson, 1989, 1991] proved the

existence and found sufficient conditions for uniqueness. For the dynamic problems, Martin and Oden [Martin and Oden, 1987] made an important contribution by proposing and experimentally proving a non-local and non-linear frictional law, and studying the existence and uniqueness of the solution under such friction law. The result for the static problems commonly shows that uniqueness is only achieved under the restriction of a sufficiently small coefficient of friction, leaving open the possible non-uniqueness for large friction coefficients.

Part II

A Study on Elasticity --- the Analytical Solution in Closed Form to a Pyramid Surface Loading Profile

This part presents a contribution to elasticity --- a set of Boussinesq-Curruti solutions to linear/bilinear distribution of normal and tangential loading over a triangular area. Based on that, solution sets to normal and tangential surface loading pyramids have been constructed. The importance of the work is that it provides a displacement solution set in closed form for a basic loading element, which is of great importance in a numerical solution to a general 3-D contact problem. Normal and tangential loading are considered, and both normal and tangential displacements are calculated. The triangular loading element will be useful in describing complicated contact domains, and the first-order loading functions will help accurately capture arbitrary loading profiles. In fact, the work is the fundamental part to the research work to develop an effective and efficient semi-analytical solutions 3D contact problems with general geometry and loading profile.

As examples, the solution set to normal and tangential tractions over equilateral triangular bases have been presented. Base on the fundamental work, the solution sets to normal and tangential pyramidal loads have been developed, which serve as load elements in subsequent parts and play a key role in the success of Semi-Analytical Method for contact problems.

Chapter 3

Elastic Solution to a Concentrated Load and Distributed Loads

The basis of the solutions presented here is the classical point-load problem attributed to Boussinesq, which is briefly reviewed below. Consider a continuous distribution of load over a surface area S of an elastic body. The coordinate system is chosen as shown in Figure 3.1. The x - y plane is on the surface, while the z -axis points into the body. Variables (ξ, η) refer to the surface points within area S , and the coordinates (x, y) refer to any surface point either inside or outside the contact area. The senses of loads and displacements are the same as the directions of the coordinate axes. The concentrated force is modeled by letting S approach 0 such that the force acts at the origin.

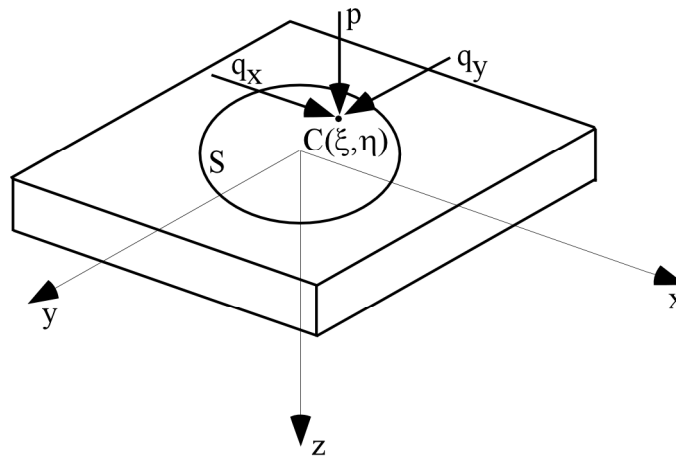


Figure 3.1 The Coordinate System and Senses of Applied Loads

3.1 Potential Functions

For the problem of a distributed load applied to an area S on an elastic half space, Love showed that the elastic displacement U_x , U_y , and U_z at any point in the solid can be expressed in terms of derivatives of a group of potential functions [Love 1927]. Johnson systematically expressed the procedure in a simpler way [Johnson 1985]. If we consider normal and tangential loading separately (which is a practical approach), the notation suggested by Dydo and Busby is a further simplification [Dydo and Busby 1995].

We define the potential functions as follows:

$$\rho = \sqrt{(x - \xi)^2 + (y - \eta)^2 + z^2} \quad (3.1)$$

$$\Psi = \iint_S \frac{F(\xi, \eta)}{\rho} d\xi d\eta \quad (3.2)$$

$$X = \iint_S F(\xi, \eta) \ln[\rho + z] d\xi d\eta \quad (3.3)$$

$$\Omega = \iint_S F(\xi, \eta) [z \ln(\rho + z) - \rho] d\xi d\eta \quad (3.4)$$

where, $F(\xi, \eta)$ is the loading profile over surface area S . The following relations hold:

$$\frac{\partial \Omega}{\partial z} = X, \quad \frac{\partial X}{\partial z} = \Psi \quad (3.5)$$

Functions (3.2) - (3.4) satisfy the Laplace equation.

As a concentrated load at the origin is considered, the three potential functions are simplified to:

$$\Psi = \frac{F}{\rho} \quad (3.6)$$

$$X = F \ln[\rho + z] \quad (3.7)$$

$$\Omega = F[z \ln(\rho + z) - \rho] \quad (3.8)$$

Here,

$$\rho = \sqrt{(x - \xi)^2 + (y - \eta)^2} \quad (3.9)$$

and F is the magnitude of concentrated force.

3.2 Displacement Field in Terms of Potential Function

3.2.1 Concentrated Force P Normal to the Surface Only (z-Direction)

The displacement components at any point (x,y,z) in the solid can be found as:

$$\begin{aligned}
 U_x &= \frac{1}{4\pi G} \left\{ (2\nu - 1) \frac{\partial X}{\partial x} - z \frac{\partial \Psi}{\partial x} \right\} \\
 &= \frac{P}{4\pi G} \left\{ \frac{xz}{\rho^3} - (1 - 2\nu) \frac{x}{\rho(\rho + z)} \right\}
 \end{aligned} \tag{3.10}$$

$$\begin{aligned}
 U_y &= \frac{1}{4\pi G} \left\{ (2\nu - 1) \frac{\partial X}{\partial y} - z \frac{\partial \Psi}{\partial y} \right\} \\
 &= \frac{P}{4\pi G} \left\{ \frac{yz}{\rho^3} - (1 - 2\nu) \frac{y}{\rho(\rho + z)} \right\}
 \end{aligned} \tag{3.11}$$

$$\begin{aligned}
 U_z &= \frac{1}{4\pi G} \left\{ 2(1 - \nu) \Psi - z \frac{\partial \Psi}{\partial z} \right\} \\
 &= \frac{P}{4\pi G} \left\{ \frac{z^2}{\rho^3} + \frac{2(1 - \nu)}{\rho} \right\}
 \end{aligned} \tag{3.12}$$

By setting $z = 0$, the components of displacement of a surface point (x,y) are obtained immediately:

$$\bar{U}_x = -(1 - 2\nu) \frac{P}{4\pi G} \frac{x}{\rho^2} \tag{3.13}$$

$$\bar{U}_y = -(1 - 2\nu) \frac{P}{4\pi G} \frac{y}{\rho^2} \tag{3.14}$$

$$\bar{U}_z = \frac{P(1 - \nu)}{2\pi G} \frac{1}{\rho} \tag{3.15}$$

where the over-bar notation indicates a quantity evaluated at the surface $z = 0$.

3.2.2 Concentrated Tangential Force Q_x Only (x-Direction)

The displacement components at any point (x,y,z) in the solid can be found as:

$$U_x = \frac{1}{4\pi G} \left\{ 2\Psi + 2\nu \frac{\partial^2 \Omega}{\partial x^2} - z \frac{\partial^2 X}{\partial x^2} \right\} \quad (3.16)$$

$$= \frac{Q_x}{4\pi G} \left\{ \frac{1}{\rho} + \frac{x^2}{\rho^3} + (1-2\nu) \left[\frac{1}{\rho+z} - \frac{x^2}{\rho(\rho+z)^2} \right] \right\}$$

$$U_y = \frac{1}{4\pi G} \left\{ 2\nu \frac{\partial^2 \Omega}{\partial x \partial y} - z \frac{\partial^2 X}{\partial x \partial y} \right\} \quad (3.17)$$

$$= \frac{Q_x}{4\pi G} \left\{ \frac{xy}{\rho^3} - (1-2\nu) \frac{xy}{\rho(\rho+z)^2} \right\}$$

$$U_z = \frac{1}{4\pi G} \left\{ (1-2\nu) \frac{\partial X}{\partial x} - z \frac{\partial \Psi}{\partial x} \right\} \quad (3.18)$$

$$= \frac{Q_x}{4\pi G} \left\{ \frac{xz}{\rho^3} + (1-2\nu) \frac{x}{\rho(\rho+z)} \right\}$$

Again, by setting $z = 0$, the displacements of a surface point (x,y) are obtained immediately:

$$\bar{U}_x = \frac{Q_x}{2\pi G} \left\{ \frac{1-\nu}{\rho} + \nu \frac{x^2}{\rho^3} \right\} \quad (3.19)$$

$$\bar{U}_y = \frac{\nu Q_x}{2\pi G} \left\{ \frac{xy}{\rho^3} \right\} \quad (3.20)$$

$$\bar{U}_z = \frac{(1-2\nu)Q_x}{4\pi G} \left\{ \frac{x}{\rho^2} \right\} \quad (3.21)$$

The displacement field, due to a concentrated tangential force in y-direction Q_y exerted at origin, can be derived similarly.

3.3 The Surface Displacements Produced by the Distribution of Surface Traction

3.3.1 Distribution of Normal Pressure over Area S Only

By using the principle of superposition, the components of surface displacement can be obtained from (3.13) - (3.15) by integrating over surface area S:

$$\bar{U}_x = -\frac{1-2\nu}{4\pi G} \iint_S \frac{P(\xi, \eta)(x-\xi)}{\rho^2} d\xi d\eta \quad (3.22)$$

$$\bar{U}_y = -\frac{1-2\nu}{4\pi G} \iint_S \frac{P(\xi, \eta)(y-\eta)}{\rho^2} d\xi d\eta \quad (3.23)$$

$$\bar{U}_z = \frac{1-\nu}{2\pi G} \iint_S \frac{P(\xi, \eta)}{\rho} d\xi d\eta \quad (3.24)$$

3.3.2 Distribution of Tangential Loading over Area S Only

By using the principle of superposition, the components of surface displacement can be obtained from (3.19) - (3.21) by integrating over surface area S:

$$\bar{U}_x = \frac{1-\nu}{2\pi G} \iint_S \frac{Q_x(\xi, \eta)}{\rho} d\xi d\eta + \frac{\nu}{2\pi G} \iint_S \frac{Q_x(\xi, \eta)(x-\xi)^2}{\rho^3} d\xi d\eta \quad (3.25)$$

$$\bar{U}_y = \frac{\nu}{2\pi G} \iint_S \frac{Q_x(\xi, \eta)(x-\xi)(y-\eta)}{\rho^3} d\xi d\eta \quad (3.26)$$

$$\bar{U}_z = \frac{1-2\nu}{4\pi G} \iint_S \frac{Q_x(\xi, \eta)(x-\xi)}{\rho^2} d\xi d\eta \quad (3.27)$$

The equations (3.22)~(3.27) are the foundation of developing solutions to any distributed loading profiles. The set of equation serves as a starting point of subsequent chapters.

Chapter 4

The Surface Displacements Due To Distribution of Surface Traction over a Triangular Area

The displacement field can be obtained by evaluating integrals (3.22)~(3.27) over the triangle. The method was first used by Svec and Gladwell [Svec and Gladwell, 1971] to obtain the explicit solution of normal deflection due to a distribution of normal pressure.

4.1 Integration Technique over a Triangular Area

4.1.1 Geometry and Notation

Figure 4.1 shows the geometry and notation of triangle $A_1A_2A_3$. Denote by δ_1 , δ_2 and δ_3 the angles between positive direction of A_2A_3 , A_3A_1 , A_1A_2 and positive direction of x -axis. A point $B(x,y)$ within triangle $A_1A_2A_3$ divides it into three sub-triangles, denoted by Δ_1 , Δ_2 and Δ_3 respectively. The following procedure will be taken over three sub-triangles.

Considering Δ_1 (Figure 4.2), denote by ϵ_1 and ϵ_2 the angles between A_2A_3 and vector BA_2 , BA_3 respectively. In general these two angles in sub-triangle Δ_i are denoted by ϵ_{2i-1} and ϵ_{2i} . Denote by n_1 the normal distance from B to A_2A_3 . In

general this distance in sub-triangle Δ_i is denoted by n_i . Introduce the polar coordinate system (r, θ) with origin located at $B(x,y)$; then, the following relations hold:

$$\theta = \delta_1 - \phi \quad (4.1)$$

$$BS_1 = \frac{BN_1}{\sin \phi} = n_1 \csc \phi \quad (4.2)$$

$$\xi - x = r \cos \theta = r \cos(\delta_1 - \phi) \quad (4.3)$$

$$\eta - y = r \sin \theta = r \sin(\delta_1 - \phi) \quad (4.4)$$

The integrals are then carried out in the polar coordinate system. For example, an integral over sub-triangle Δ_i is evaluated as follows. Because $d\theta = -d\phi$,

$$\begin{aligned} \iint_{\Delta_i} \frac{1}{\rho} d\xi d\eta &= \iint_{\Delta_i} \frac{1}{r} r dr d\theta = \int_{\theta_1}^{\theta_2} d\theta \int_0^{n_i \csc \phi} dr \\ &= \int_{\varepsilon_{2i}}^{\varepsilon_{2i-1}} d\phi \int_0^{n_i \csc \phi} dr = n_i \left[\ln \left| \tan \frac{\phi}{2} \right| \right]_{\varepsilon_{2i}}^{\varepsilon_{2i-1}} \end{aligned}$$

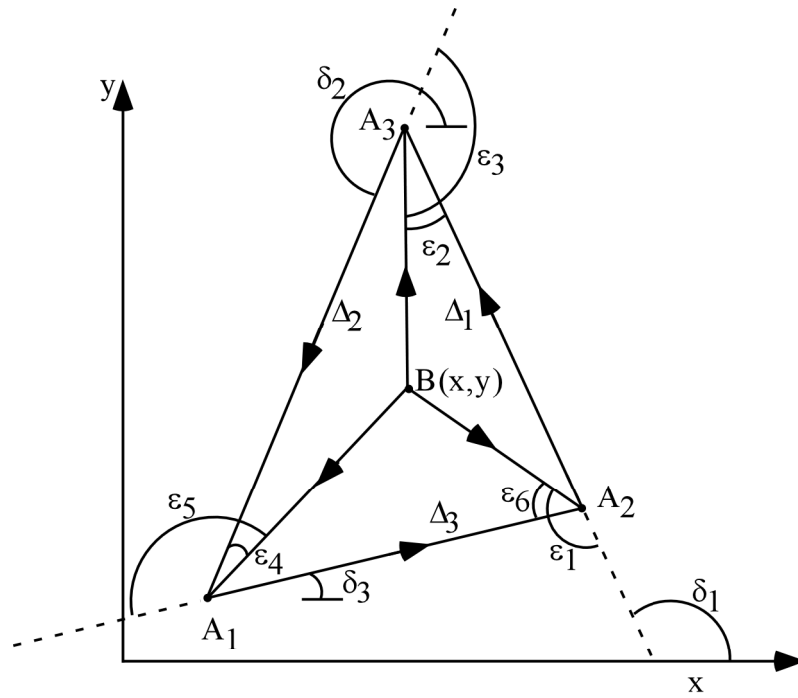


Figure 4.1 The Geometry and Notation of the Loading Triangle.

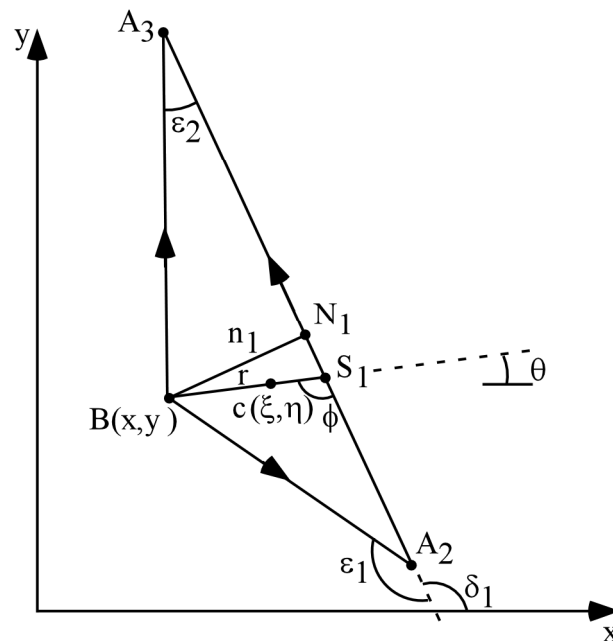


Figure 4.2 The Geometry and Notation of the Sub-Triangle Δ_1 .

4.1.2 The Consistency of Formulae

The sign of n_i is designated as shown in Figure 4.3. This convention is automatically guaranteed if one uses algebraic expression for n_i instead of absolute value.

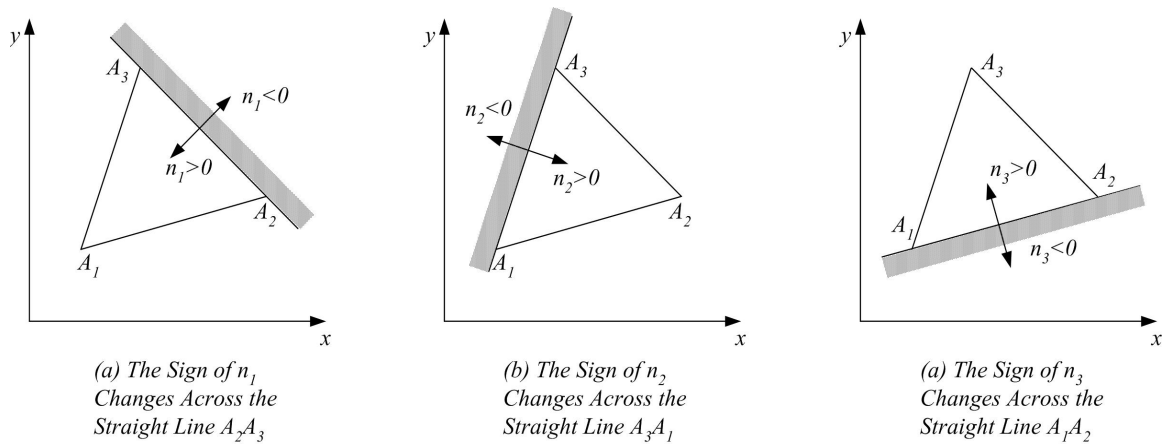


Figure 4.3 The Convention of Sign of n_i

The integrals given in this dissertation are derived for the case of point $B(x,y)$ within the triangle $A_1A_2A_3$. However, the work shows that the formulae hold outside the loading triangle if the appropriate signs are attached to the integrals over three sub-triangles, confirming the assertion made by Svec and Gladwell [Svec and Gladwell 1971]. This can be easily shown in Figure 4.4: (a) is the case that point B is within triangle $A_1A_2A_3$, while (b) is the case that point B is outside the triangle. In the second case (b), the three sub-triangles exceed the range of original triangle. However, since the loading profile is not defined outside

triangle $A_1A_2A_3$, the integration over three sub-triangles is still equivalent to the integration over the original triangle. Even though the loading profile is defined outside the original triangle, due to one of the normals such as n_1 takes negative sign while the others such as n_2 and n_3 take positive sign, the overall effect is still equivalent to the original integral.

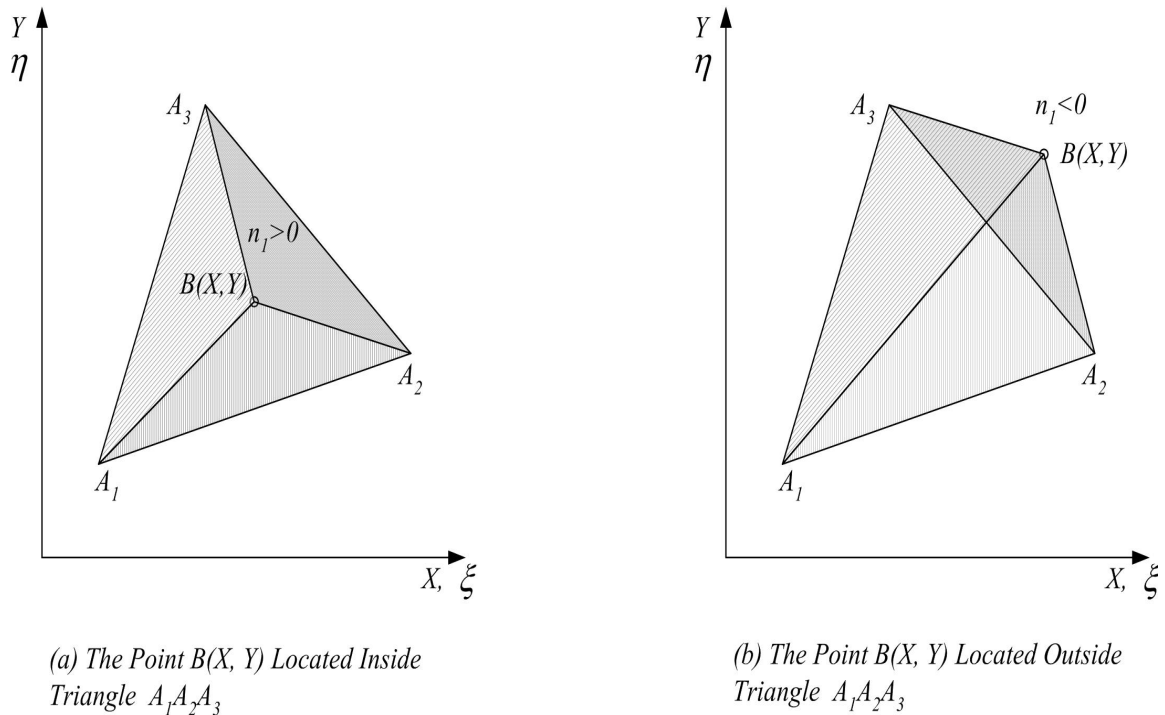


Figure 4.4 The Study of Consistency of Formula (a) Point B Is Inside Triangle $A_1A_2A_3$, (b) Point B Is Outside Triangle $A_1A_2A_3$

Therefore, we use the same formula for both inside and outside the loading area, instead of considering them separately. Svec and Gladwell [Svec and Gladwell

1971] also indicate that numerical integration gives poor results for integrals like (3.22)-(3.27), and therefore closed-form solutions are sought in the dissertation and presented next.

4.1.3 The Notation of Various Integrals

For the purpose of mathematical simplicity of expression, the following notation is introduced:

$$I_{ijkm} = \iint_{\Delta_i} \frac{(x-\xi)^k (y-\eta)^m}{\rho^j} d\xi d\eta \quad (4.5)$$

where i indicates the sub-triangle number ($i=1,2,3$), j,k,m are exponents, and

$$\rho = r = \sqrt{(x-\xi)^2 + (y-\eta)^2} \quad (4.6)$$

Note that in the integral (4.6) the integration domain is defined by (ξ, η) , and (x,y) is the point at which the displacement solution is desired. For the purposes of evaluating the integrals, the coordinates (x,y) are considered as constants.

It is also convenient to use the notation:

$$I_{Sjkm} = \sum_{i=1}^3 I_{ijkm} \quad (4.7)$$

4.2 Displacement Field Due To a Distribution of Normal Pressure

$P(\xi, \eta)$ Over Sub-Triangle Δ_i

First, some simple distributions of normal pressure are considered. More complicated linear or bilinear loading profile can be modeled using an arithmetic sum of some simple distributions. The following results are obtained by evaluating equation (3.22) - (3.24).

4.2.1 Constant $P(\xi, \eta) = 1$

$$\bar{U}_x = -\frac{1-2\nu}{4\pi G} \iint_{\Delta_i} \frac{(x-\xi)}{\rho^2} d\xi d\eta = -\frac{1-2\nu}{4\pi G} I_{i210} \quad (4.8)$$

$$\bar{U}_y = -\frac{1-2\nu}{4\pi G} \iint_{\Delta_i} \frac{(y-\eta)}{\rho^2} d\xi d\eta = -\frac{1-2\nu}{4\pi G} I_{i201} \quad (4.9)$$

$$\bar{U}_z = \frac{1-\nu}{2\pi G} \iint_{\Delta_i} \frac{1}{\rho} d\xi d\eta = \frac{1-\nu}{2\pi G} I_{i100} \quad (4.10)$$

4.2.2 Linear Distribution $P(\xi, \eta) = y - \eta$

$$\bar{U}_x = -\frac{1-2\nu}{4\pi G} \iint_{\Delta_i} \frac{(x-\xi)(y-\eta)}{\rho^2} d\xi d\eta = -\frac{1-2\nu}{4\pi G} I_{i211} \quad (4.11)$$

$$\bar{U}_y = -\frac{1-2\nu}{4\pi G} \iint_{\Delta_i} \frac{(y-\eta)^2}{\rho^2} d\xi d\eta = -\frac{1-2\nu}{4\pi G} I_{i202} \quad (4.12)$$

$$\bar{U}_z = \frac{1-\nu}{2\pi G} \iint_{\Delta_i} \frac{y-\eta}{\rho} d\xi d\eta = \frac{1-\nu}{2\pi G} I_{i101} \quad (4.13)$$

4.2.3 Bilinear Distribution $P(\xi, \eta) = (x - \xi)(y - \eta)$

$$\bar{U}_x = -\frac{1-2\nu}{4\pi G} \iint_{\Delta_i} \frac{(x-\xi)^2(y-\eta)}{\rho^2} d\xi d\eta = -\frac{1-2\nu}{4\pi G} I_{i221} \quad (4.14)$$

$$\bar{U}_y = -\frac{1-2\nu}{4\pi G} \iint_{\Delta_i} \frac{(x-\xi)(y-\eta)^2}{\rho^2} d\xi d\eta = -\frac{1-2\nu}{4\pi G} I_{i212} \quad (4.15)$$

$$\bar{U}_z = \frac{1-\nu}{2\pi G} \iint_{\Delta_i} \frac{(x-\xi)(y-\eta)}{\rho} d\xi d\eta = \frac{1-\nu}{2\pi G} I_{i111} \quad (4.16)$$

The above results are summarized in Table 4.1 for quick reference:

Table 4.1 Displacements in Terms of Applied Normal Load

Distribution of Loading (Surface Traction)	\bar{U}_x	\bar{U}_y	\bar{U}_z
<i>Constant</i> $P(\xi, \eta) = 1$	bI_{i210}	bI_{i201}	aI_{i100}
<i>Linear</i> $P(\xi, \eta) = y - \eta$	bI_{i211}	bI_{i202}	aI_{i101}
<i>Bilinear</i> $P(\xi, \eta) = (x - \xi)(y - \eta)$	bI_{i221}	bI_{i212}	aI_{i111}

Note: $a = \frac{1-\nu}{2\pi G}$, $b = -\frac{1-2\nu}{4\pi G}$

4.3 Displacement Field Due To Tangential Pressure $Q_x(\xi, \eta)$ Over Sub-Triangle Δ_i

The following results are obtained by evaluating equations (3.25) - (3.27).

4.3.1 Constant $Q_x(\xi, \eta) = 1$

$$\bar{U}_x = \frac{1-\nu}{2\pi G} \iint_{\Delta_i} \frac{1}{\rho} d\xi d\eta + \frac{\nu}{2\pi G} \iint_{\Delta_i} \frac{(x-\xi)^2}{\rho^3} d\xi d\eta = \frac{1-\nu}{2\pi G} I_{i100} + \frac{\nu}{2\pi G} I_{i320} \quad (4.17)$$

$$\bar{U}_y = \frac{\nu}{2\pi G} \iint_{\Delta_i} \frac{(x-\xi)(y-\eta)}{\rho^3} d\xi d\eta = \frac{\nu}{2\pi G} I_{i311} \quad (4.18)$$

$$\bar{U}_z = \frac{1-2\nu}{4\pi G} \iint_{\Delta_i} \frac{(x-\xi)}{\rho^2} d\xi d\eta = \frac{1-2\nu}{4\pi G} I_{i210} \quad (4.19)$$

4.3.2 Linear Distribution $Q_x(\xi, \eta) = y - \eta$

$$\bar{U}_x = \frac{1-\nu}{2\pi G} \iint_{\Delta_i} \frac{y-\eta}{\rho} d\xi d\eta + \frac{\nu}{2\pi G} \iint_{\Delta_i} \frac{(x-\xi)^2(y-\eta)}{\rho^3} d\xi d\eta = \frac{1-\nu}{2\pi G} I_{i101} + \frac{\nu}{2\pi G} I_{i321} \quad (4.20)$$

$$\bar{U}_y = \frac{\nu}{2\pi G} \iint_{\Delta_i} \frac{(x-\xi)(y-\eta)^2}{\rho^3} d\xi d\eta = \frac{\nu}{2\pi G} I_{i312} \quad (4.21)$$

$$\bar{U}_z = \frac{1-2\nu}{4\pi G} \iint_{\Delta_i} \frac{(x-\xi)(y-\eta)}{\rho^2} d\xi d\eta = \frac{1-2\nu}{4\pi G} I_{i211} \quad (4.22)$$

4.3.3 Bilinear Distribution $Q_x(\xi, \eta) = (x - \xi)(y - \eta)$

$$\begin{aligned}\bar{U}_x &= \frac{1-\nu}{2\pi G} \iint_{\Delta_i} \frac{(x-\xi)(y-\eta)}{\rho} d\xi d\eta + \frac{\nu}{2\pi G} \iint_{\Delta_i} \frac{(x-\xi)^3(y-\eta)}{\rho^3} d\xi d\eta \\ &= \frac{1-\nu}{2\pi G} I_{i111} + \frac{\nu}{2\pi G} I_{i331}\end{aligned}\quad (4.23)$$

$$\bar{U}_y = \frac{\nu}{2\pi G} \iint_{\Delta_i} \frac{(x-\xi)^2(y-\eta)^2}{\rho^3} d\xi d\eta = \frac{\nu}{2\pi G} I_{i322}\quad (4.24)$$

$$\bar{U}_z = \frac{1-2\nu}{4\pi G} \iint_{\Delta_i} \frac{(x-\xi)^2(y-\eta)}{\rho^2} d\xi d\eta = \frac{1-2\nu}{4\pi G} I_{i221}\quad (4.25)$$

The above results are summarized in Table 4.2 for quick reference:

Table 4.2 Displacements in Terms of Applied Tangential Load

Distribution of Loading (Surface Traction)	\bar{U}_x	\bar{U}_y	\bar{U}_z
<i>Constant</i> $Q(\xi, \eta) = 1$	$aI_{i100} + cI_{i320}$	cI_{i311}	bI_{i210}
<i>Linear</i> $Q(\xi, \eta) = y - \eta$	$aI_{i101} + cI_{i321}$	cI_{i312}	bI_{i211}
<i>Bilinear</i> $Q(\xi, \eta) = (x - \xi)(y - \eta)$	$aI_{i111} + cI_{i331}$	cI_{i322}	bI_{i221}

Note: $a = \frac{1-\nu}{2\pi G}$, $b = \frac{1-2\nu}{4\pi G}$, $c = \frac{\nu}{2\pi G}$

4.4 The Applications of the Solutions

The solution sets presented in section 4.3 and 4.4 are fundamentals for the construction of various sophisticated load elements, two of which are shown in Figure 4.5. The construction of pyramidal solution set is to be discussed in detail in the subsequent part (Part III).

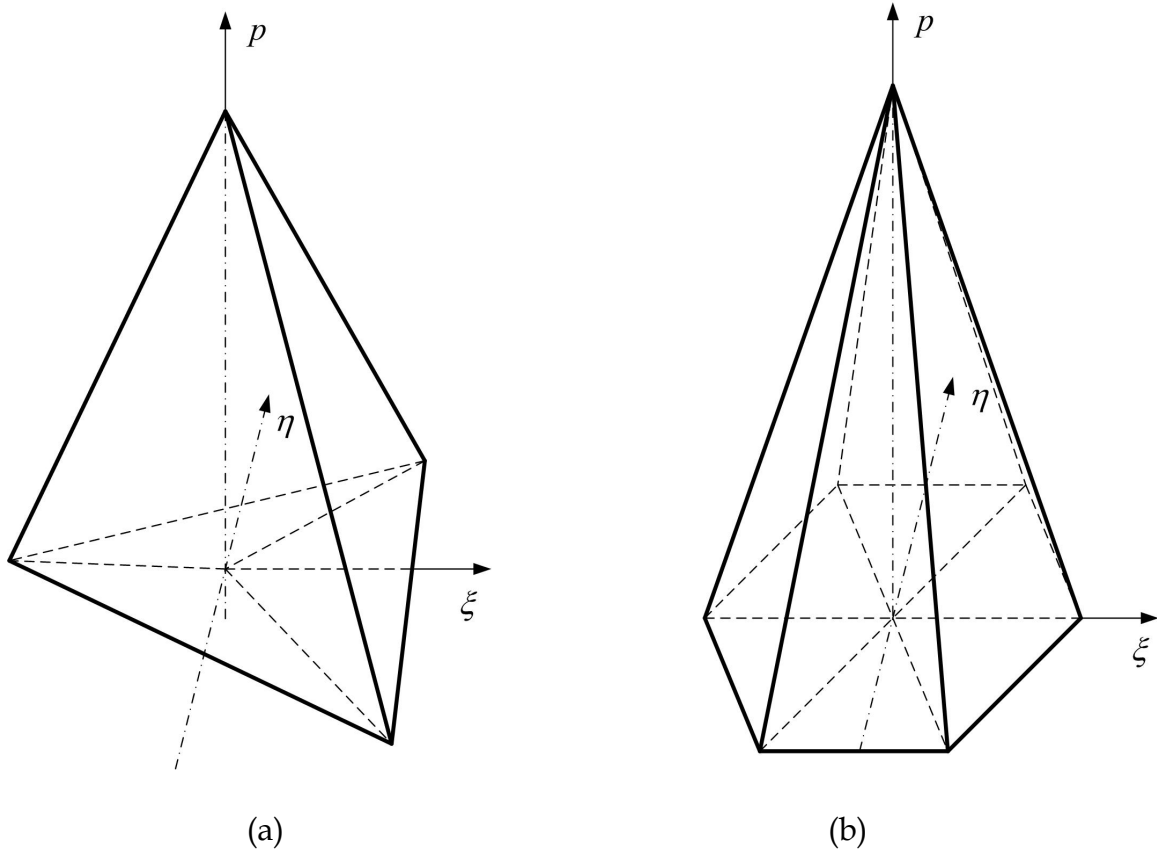


Figure 4.5 Loading Elements Assembled from Simpler Triangular Elements: (a) Tetrahedral Element, (b) Pyramidal Element

4.5 The Evaluations of Various Integrals over Sub-Triangles

The key work now is to evaluate these integrals obtained in the previous section. Here a detailed derivation is given for a typical integral I_{i211} . First, the transformation to polar coordinates is implemented, and then various trigonometric tools are applied to evaluate and simplify the integral. The results are given for other required integrals.

$$\begin{aligned}
I_{i211} &= \iint_{\Delta_i} \frac{(x-\xi)(y-\eta)}{\rho^2} d\xi d\eta \\
&= \iint_{\Delta_i} \frac{(-r \cos(\delta_i - \phi))(-r \sin(\delta_i - \phi))}{r^2} r dr d\theta \\
&= \int_{\theta_1}^{\theta_2} \cos(\delta_i - \phi) \sin(\delta_i - \phi) d\theta \int_0^{n_i \csc \phi} r dr \\
&= \frac{n_i^2}{4} \int_{\varepsilon_{2i}}^{\varepsilon_{2i-1}} \frac{\sin 2(\delta_i - \phi)}{(\sin \phi)^2} d\phi \\
&= -\frac{n_i^2}{4} \left[\sin 2\delta_i \cot \phi + 2\phi \sin 2\delta_i + 2 \cos 2\delta_i \ln |\sin \phi| \right]_{\varepsilon_{2i}}^{\varepsilon_{2i-1}}
\end{aligned}$$

List of evaluations of various integrals is given below:

$$I_{i100} = n_i \left[\ln \left| \tan \frac{\phi}{2} \right| \right]_{\varepsilon_{2i}}^{\varepsilon_{2i-1}} \quad (4.26)$$

$$I_{i101} = \frac{n_i^2}{2} \left[\frac{\sin \delta_i}{\sin \phi} + \cos \delta_i \ln \left| \tan \frac{\phi}{2} \right| \right]_{\varepsilon_{2i}}^{\varepsilon_{2i-1}} \quad (4.27)$$

$$I_{i110} = -\frac{n_i^2}{2} \left[-\frac{\cos \delta_i}{\sin \phi} + \sin \delta_i \ln \left| \tan \frac{\phi}{2} \right| \right]_{\varepsilon_{2i}}^{\varepsilon_{2i-1}} \quad (4.28)$$

$$\begin{aligned}
I_{i111} &= \frac{n_i^3}{6} \left[-\frac{\sin 2\delta_i}{2} \left[\frac{\cos \phi}{(\sin \phi)^2} + \sinh^{-1}(\cot \phi) \right] \right. \\
&\quad \left. - 2 \sin 2\delta_i \ln \left| \tan \frac{\phi}{2} \right| + \frac{2 \cos 2\delta_i}{\sin \phi} \right]_{\varepsilon_{2i}}^{\varepsilon_{2i-1}} \quad (4.29)
\end{aligned}$$

$$I_{i201} = -n_i \left[\sin \delta_i \ln |\sin \phi| - \phi \cos \delta_i \right]_{\mathcal{E}_{2i}}^{\mathcal{E}_{2i-1}} \quad (4.30)$$

$$I_{i202} = \frac{n_i^2}{4} \left[-(1 - \cos 2\delta_i) \cot \phi + 2\phi \cos 2\delta_i - 2 \sin 2\delta_i \ln |\sin \phi| \right]_{\mathcal{E}_{2i}}^{\mathcal{E}_{2i-1}} \quad (4.31)$$

$$I_{i210} = -n_i \left[\cos \delta_i \ln |\sin \phi| + \phi \sin \delta_i \right]_{\mathcal{E}_{2i}}^{\mathcal{E}_{2i-1}} \quad (4.32)$$

$$I_{i211} = -\frac{n_i^2}{4} \left[\sin 2\delta_i \cot \phi + 2\phi \sin 2\delta_i + 2 \cos 2\delta_i \ln |\sin \phi| \right]_{\mathcal{E}_{2i}}^{\mathcal{E}_{2i-1}} \quad (4.33)$$

$$I_{i212} = -\frac{n_i^3}{12} \left[\frac{(\cos \delta_i - \cos 3\delta_i)}{-2(\sin \phi)^2} - (-3 \sin 3\delta_i + \sin \delta_i) \cot \phi \right. \\ \left. + 4 \cos 3\delta_i \ln |\sin \phi| + 4\phi \sin 3\delta_i \right]_{\mathcal{E}_{2i}}^{\mathcal{E}_{2i-1}} \quad (4.34)$$

$$I_{i221} = -\frac{n_i^3}{12} \left[\frac{(\sin 3\delta_i + \sin \delta_i)}{-2(\sin \phi)^2} + (3 \cos 3\delta_i + \cos \delta_i) \cot \phi \right. \\ \left. - 4 \sin 3\delta_i \ln |\sin \phi| + 4\phi \cos 3\delta_i \right]_{\mathcal{E}_{2i}}^{\mathcal{E}_{2i-1}} \quad (4.35)$$

$$I_{i311} = \frac{n_i}{2} \left[(\sin 2\delta_i) \ln \left| \tan \frac{\phi}{2} \right| + 2 \sin 2\delta_i \cos \phi - 2 \cos 2\delta_i \sin \phi \right]_{\mathcal{E}_{2i}}^{\mathcal{E}_{2i-1}} \quad (4.36)$$

$$I_{i312} = -\frac{n_i^2}{8} \left[\frac{(\cos 3\delta_i - \cos \delta_i)}{\sin \phi} + (\sin \delta_i - 3 \sin 3\delta_i) \ln \left| \tan \frac{\phi}{2} \right| \right. \\ \left. + 4 \cos 3\delta_i \sin \phi - 4 \sin 3\delta_i \cos \phi \right]_{\mathcal{E}_{2i}}^{\mathcal{E}_{2i-1}} \quad (4.37)$$

$$I_{i320} = \frac{n_i}{2} \left[(\cos 2\delta_i + 1) \ln \left| \tan \frac{\phi}{2} \right| + 2 \cos 2\delta_i \cos \phi + 2 \sin 2\delta_i \sin \phi \right]_{\mathcal{E}_{2i}}^{\mathcal{E}_{2i-1}} \quad (4.38)$$

$$I_{i321} = \frac{n_i^2}{8} \left[\frac{(\sin 3\delta_i + \sin \delta_i)}{\sin \phi} + (3 \cos 3\delta_i + \cos \delta_i) \ln \left| \tan \frac{\phi}{2} \right| \right. \\ \left. + 4 \sin 3\delta_i \sin \phi + 4 \cos 3\delta_i \cos \phi \right]_{\mathcal{E}_{2i}}^{\mathcal{E}_{2i-1}} \quad (4.39)$$

$$I_{i330} = -\frac{n_i^2}{8} \left[-\frac{(3 \cos \delta_i + \cos 3\delta_i)}{\sin \phi} + (3 \sin \delta_i + 3 \sin 3\delta_i) \ln \left| \tan \frac{\phi}{2} \right| \right. \\ \left. - 4 \cos 3\delta_i \sin \phi + 4 \sin 3\delta_i \cos \phi \right]_{\mathcal{E}_{2i}}^{\mathcal{E}_{2i-1}} \quad (4.40)$$

$$\begin{aligned}
I_{i331} = \frac{n_i^3}{12} & \left[-\frac{1}{2}(\sin 2\delta_i + \frac{1}{2}\sin 4\delta_i) \left[\frac{\cos \phi}{(\sin \phi)^2} + \sinh^{-1}(\cot \phi) \right] \right. \\
& - (2\sin 2\delta_i + 4\sin 4\delta_i) \ln \left| \tan \frac{\phi}{2} \right| \\
& \left. + \frac{(2\cos 2\delta_i + 2\cos 4\delta_i)}{\sin \phi} - 4\sin 4\delta_i \cos \phi + 4\cos 4\delta_i \sin \phi \right]_{\mathcal{E}_{2i}}^{\mathcal{E}_{2i-1}}
\end{aligned} \tag{4.41}$$

$$I_{i322} = \frac{n_i^3}{3} \left[\ln \left| \tan \frac{\phi}{2} \right| + \cos \phi \right]_{\mathcal{E}_{2i}}^{\mathcal{E}_{2i-1}} \tag{4.42}$$

Chapter 5

Surface Displacement Solution Set Due to a Pyramidal Load Profile

In this chapter, the fundamental displacement solution set due to a pyramidal load profile of hexagonal base on an elastic half-space is presented. This result will be extended, and basic pyramidal elements will be used to represent arbitrary load profiles for the numerical examples.

5.1 Coordinate System

The origin O of an (X,Y,Z) Cartesian coordinate system is placed on the surface of an elastic body, with the Z -axis directed into the solid as shown in Figure 5.1. A second coordinate system, the (x,y) system, is oriented on the surface of the body and shares the origin O of the Cartesian system as well as the Z direction. The (x,y) coordinates are non-orthogonal, and as shown in Figure 5.1 they are chosen to be oriented an angle $\pi/3$ apart. As such, the lines of constant x and y form a grid of quadrilaterals on the surface. The transformation from the (x,y) coordinates to the (X,Y) coordinates is given by (keeping in mind that the two systems share the Z -coordinate):

$$\begin{Bmatrix} X \\ Y \end{Bmatrix} = \underbrace{\begin{bmatrix} l_e & l_e \cos \frac{\pi}{3} \\ 0 & l_e \sin \frac{\pi}{3} \end{bmatrix}}_{\equiv [R]} \begin{Bmatrix} x \\ y \end{Bmatrix} \quad (5.1)$$

where l_e is a characteristic grid spacing (Figure 5.1). X, Y, l_e all have units of length, while the surface coordinates x, y are dimensionless. Under this approach, x and y assume integer values in the non-orthogonal coordinate system at grid points.

Throughout the development of the solutions described later, it will be necessary to consider a rotated coordinate system (X', Y') oriented with an angle α from the original (X, Y) system. Similarly, a rotated coordinate system (x', y') , also oriented with an angle α from the original (x, y) system, must be defined. Then,

$$\begin{Bmatrix} X' \\ Y' \end{Bmatrix} = \underbrace{\begin{bmatrix} \cos \alpha & \sin \alpha \\ -\sin \alpha & \cos \alpha \end{bmatrix}}_{\equiv [T]} \begin{Bmatrix} X \\ Y \end{Bmatrix} \quad (5.2)$$

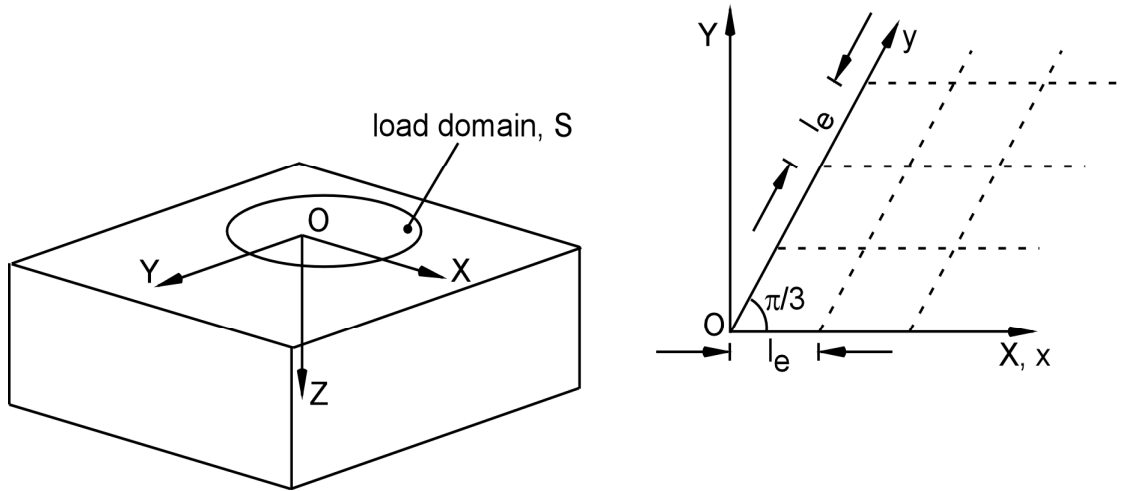


Figure 5.1 The coordinate systems used in this part and subsequent discussion.

Note: the x - y coordinate system is NOT orthogonal, but $\pi/3$ apart. Coordinate (ξ, η) are defined for the contact area only, which has the same orientation as X - Y system.

Equation (5.1) and the rotations described above imply:

$$\begin{Bmatrix} X' \\ Y' \end{Bmatrix} = [R] \begin{Bmatrix} x' \\ y' \end{Bmatrix} \quad (5.3)$$

and therefore,

$$\begin{Bmatrix} x' \\ y' \end{Bmatrix} = [R]^{-1} \begin{Bmatrix} X' \\ Y' \end{Bmatrix} = [R]^{-1} [T] \begin{Bmatrix} X \\ Y \end{Bmatrix} = \underbrace{[R]^{-1} [T] [R]}_{[T_{xy}]} \begin{Bmatrix} x \\ y \end{Bmatrix} \quad (5.4)$$

The implication here is that if we choose the rotation angle $\alpha = n\pi/3$, where n is an integer, then all the entries in the transformation matrix $[T_{xy}]$ are integers, and

grid points in the (x',y') coordinate system all coincide with grid points in the (x,y) coordinate system. To prove this, we write:

$$\mathbf{R} = \begin{bmatrix} l_e & l_e \cos \frac{\pi}{3} \\ 0 & l_e \sin \frac{\pi}{3} \end{bmatrix} = l_e \begin{bmatrix} 1 & \frac{1}{2} \\ 0 & \frac{\sqrt{3}}{2} \end{bmatrix} = \frac{l_e}{2} \begin{bmatrix} 2 & 1 \\ 0 & \sqrt{3} \end{bmatrix} \quad (5.5)$$

$$\mathbf{R}^{-1} = \frac{1}{l_e} \begin{bmatrix} 1 & -\frac{1}{\sqrt{3}} \\ 0 & \frac{2}{\sqrt{3}} \end{bmatrix} \quad (5.6)$$

$$\mathbf{T} = \begin{bmatrix} \cos \alpha & \sin \alpha \\ -\sin \alpha & \cos \alpha \end{bmatrix} = \begin{bmatrix} C & S \\ -S & C \end{bmatrix} \quad (5.7)$$

where, $C = \cos \alpha = \cos \frac{n\pi}{3}$, $S = \sin \alpha = \sin \frac{n\pi}{3}$, $n = 0,1,2,\dots,5$

$$\begin{aligned} \mathbf{T}_{xy} = \mathbf{R}^{-1} \mathbf{T} \mathbf{R} &= \frac{1}{l_e} \begin{bmatrix} 1 & -\frac{1}{\sqrt{3}} \\ 0 & \frac{2}{\sqrt{3}} \end{bmatrix} \begin{bmatrix} C & S \\ -S & C \end{bmatrix} \frac{l_e}{2} \begin{bmatrix} 2 & 1 \\ 0 & \sqrt{3} \end{bmatrix} \\ &= \frac{1}{2} \begin{bmatrix} 1 & -\frac{1}{\sqrt{3}} \\ 0 & \frac{2}{\sqrt{3}} \end{bmatrix} \begin{bmatrix} 2C & C + \sqrt{3}S \\ -2S & -S + \sqrt{3}C \end{bmatrix} \\ &= \begin{bmatrix} C + \frac{S}{\sqrt{3}} & -\frac{2S}{\sqrt{3}} \\ -\frac{2S}{\sqrt{3}} & C - \frac{S}{\sqrt{3}} \end{bmatrix} \end{aligned} \quad (5.8)$$

Table 5.1 Entities in Matrix \mathbf{T}_{xy} When α Takes the Value of $n\pi/3$

n	C	S	\mathbf{T}_{xy}
0	1	0	$\begin{bmatrix} 1 & 0 \\ 0 & 1 \end{bmatrix}$
1	$\frac{1}{2}$	$\frac{\sqrt{3}}{2}$	$\begin{bmatrix} 1 & 1 \\ -1 & 0 \end{bmatrix}$
2	$-\frac{1}{2}$	$\frac{\sqrt{3}}{2}$	$\begin{bmatrix} 0 & 1 \\ -1 & -1 \end{bmatrix}$
3	-1	0	$\begin{bmatrix} -1 & 0 \\ 0 & -1 \end{bmatrix}$
4	$-\frac{1}{2}$	$-\frac{\sqrt{3}}{2}$	$\begin{bmatrix} -1 & -1 \\ 1 & 0 \end{bmatrix}$
5	$\frac{1}{2}$	$-\frac{\sqrt{3}}{2}$	$\begin{bmatrix} 0 & -1 \\ 1 & 1 \end{bmatrix}$

It is clearly seen from Table 5.1 that the entities of $[\mathbf{T}_{xy}]$ take value 1, -1 or 0. This important property aids construction of pyramid loading solutions by superposition of fundamental tetrahedral loading solutions in rotated coordinate systems.

We further define one more coordinate system, the (ξ, η) coordinate system, which describes points within the loading domain S ; see Figure 5.1. The orientation of the (ξ, η) system is the same as the (X, Y) system; these coordinates provide for a convenient expression of the various integrals related to surface

displacement solutions and load profiles, as described next. Note that the normal and tangential tractions $P(\xi, \eta)$ and $Q(\xi, \eta)$ on the surface are expressed as functions of (ξ, η) , not as functions of (X, Y) .

5.2 The development of solutions to a normal pyramidal load element

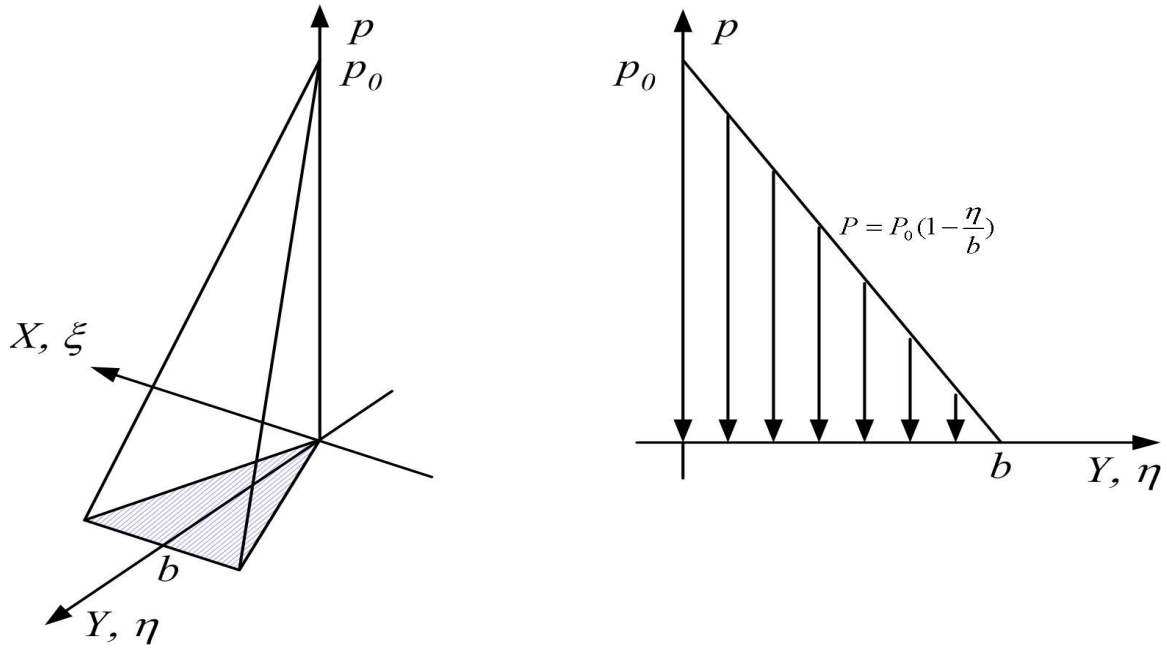
By the term “normal pyramidal load element” we mean the pyramidal load profile of normal load (pressure, in Z- direction) distribution. This section first derives the elastic solution set to a normal tetrahedral load element on equilateral base, and then presents the construction procedure of pyramidal solution.

5.2.1 Normal Tetrahedral Pressure Distribution on Equilateral Triangle Base

Consider a loading profile of normal pressure varying linearly in the η -direction according to:

$$P(\xi, \eta) = P_o \left(1 - \frac{\eta}{b} \right); \quad 0 \leq \eta \leq b \quad (5.9)$$

acting over an equilateral triangle OAB on an elastic surface (Figure 5.2). In order to determine the displacement field at a surface point with coordinates (x, y) due to the action of P , the pressure profile is re-written as:



(a) tetrahedral pressure distribution (b) linear loading profile in η
 on equilateral triangle base

Figure 5.2. A Linear Loading Profile over an Equilateral Triangle Base: (a) Tetrahedral Pressure Distribution, (b) Linear Loading Profile in η .

$$\begin{aligned}
 P(\xi, \eta) &= \frac{P_0}{b}(b - \eta) \\
 &= \underbrace{P_0\left(1 - \frac{y}{b}\right)}_{\text{Constant Part}} + \underbrace{\frac{P_0}{b}(y - \eta)}_{\text{Linear Part}}
 \end{aligned}
 \tag{5.10}$$

Recall that the (ξ, η) coordinates describe the area over which the load is applied, while the parameters (x, y) indicate the location at which the displacement solution is desired. As a result, in equation (5.10) the parameter y is considered

to be constant. Then, the components of displacement at any surface point (x,y) are readily available as the superposition of displacements due to constant normal pressure [equations (4.8) - (4.10)] and due to linear normal pressure distribution [equations (4.11) - (4.13)]:

$$\bar{U}_x(x,y) = -\frac{1-2\nu}{4\pi G} \left\{ P_0 \left(1 - \frac{y}{b}\right) I_{S210} + \frac{P_0}{b} I_{S211} \right\} \quad (5.11)$$

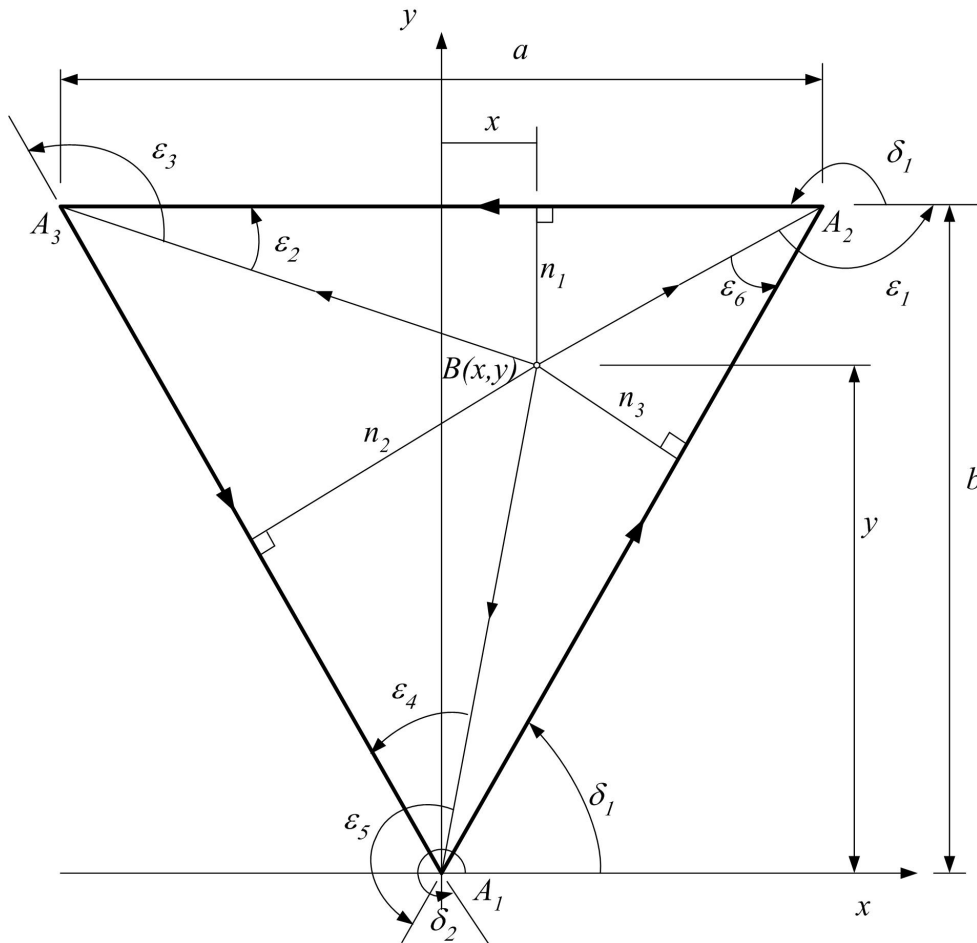


Figure 5.3 The Geometry and Notation of Equilateral Triangular Base

$$\bar{U}_y(x, y) = -\frac{1-2\nu}{4\pi G} \left\{ P_0 \left(1 - \frac{y}{b}\right) I_{S_{201}} + \frac{P_0}{b} I_{S_{202}} \right\} \quad (5.12)$$

$$\bar{U}_z(x, y) = \frac{1-\nu}{2\pi G} \left\{ P_0 \left(1 - \frac{y}{b}\right) I_{S_{100}} + \frac{P_0}{b} I_{S_{101}} \right\} \quad (5.13)$$

In this equilateral triangle, the parameters needed to evaluate the integrals are listed as follows (Figure 5.3):

The orientation angles of three triangular sides take the value:

$$\begin{cases} \delta_1 = \pi \\ \delta_2 = -\frac{\pi}{3} \\ \delta_3 = \frac{\pi}{3} \end{cases} \quad (5.14)$$

The normals of point B(X, Y) to three sides of the triangle are evaluated as:

$$\begin{cases} n_1 = b - y \\ n_2 = (w + x) \cos \alpha = x \cos \frac{\pi}{6} + y \sin \frac{\pi}{6} \\ n_3 = (w - x) \cos \alpha = -x \cos \frac{\pi}{6} + y \sin \frac{\pi}{6} \end{cases} \quad (5.15)$$

The six characteristic angles ε_i ($i=1, 2, \dots, 6$):

$$\left\{ \begin{array}{l} \varepsilon_1 = \pi - \arctan \frac{n_1}{\frac{a}{2} - x} \\ \varepsilon_2 = \arctan \frac{n_1}{\frac{a}{2} + x} \\ \varepsilon_3 = \varepsilon_2 + \frac{2}{3}\pi \\ \varepsilon_4 = \frac{2}{3}\pi - \operatorname{arc\,cot} \frac{x}{y} \\ \varepsilon_5 = \varepsilon_4 + \frac{2}{3}\pi \\ \varepsilon_6 = \varepsilon_1 - \frac{2}{3}\pi \end{array} \right. \quad (5.16)$$

The expressions (5.14~16) satisfy the requirement of formula consistency presented in section 4.1.2.

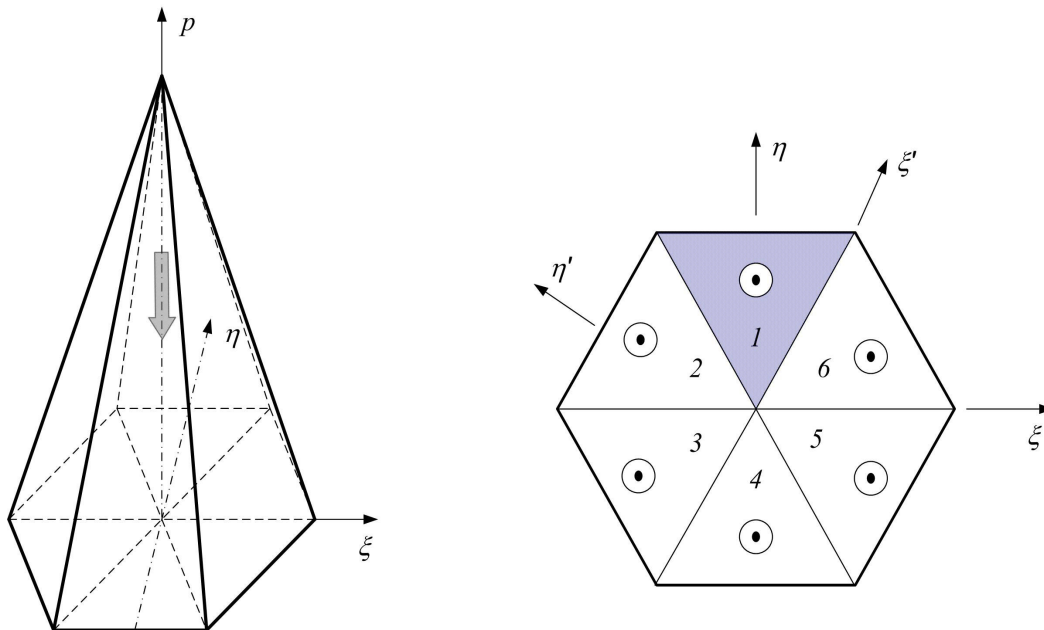


Figure 5.4 (a) The Pyramid Consists of Six Tetrahedrons; (b) The Hexagonal Base Consists of Six Equilateral Triangles

5.2.2 Normal Pyramidal Pressure Distribution on Hexagonal Base

The solution set to a normal pyramidal load element is obtained by applying principle of superposition of linear elasticity. The pyramid on a hexahedral base consists of six tetrahedrons on equilateral triangular base, as shown in Figure 5.4.

We consider the first tetrahedron, denote by $\mathbf{U}_{(1)}(\mathbf{X})$ the surface displacement solution to the first tetrahedral load element. Here,

$\mathbf{X} = \begin{Bmatrix} X \\ Y \end{Bmatrix}$ is the surface point that solution set is desired; $\mathbf{U} = \begin{Bmatrix} U_x \\ U_y \\ U_z \end{Bmatrix}$ is the surface

displacement set. We notice that, due to the symmetry, this solution set can also be used for second tetrahedron in rotated coordinate system $X'-Y'$, written as:

$$\text{If } \mathbf{X}'_B = \mathbf{X}_A, \text{ or } \begin{Bmatrix} X'_B \\ Y'_B \end{Bmatrix} = \begin{Bmatrix} X_A \\ Y_A \end{Bmatrix},$$

$$\text{then, } \mathbf{U}'_{(2)}(\mathbf{X}'_B) = \mathbf{U}_{(1)}(\mathbf{X}_A) \quad (5.17)$$

where, the prime represents the parameters measured in rotated coordinate system $X'-Y'$; the subscript (1) and (2) represent the solution due to tetrahedral load element No. 1 and No. 2 respectively.

The above relation says that the displacement solution at point B due to tetrahedron No.2 measured in $X'-Y'$ system, is the same as the one at point A due to tetrahedron No.1 measured in $X-Y$ coordinate system.

Now, suppose B is the surface point that solution is desired. From

$\mathbf{X}'_B = \mathbf{X}_A$, and $\mathbf{X}'_B = \mathbf{T}\mathbf{X}_B$, we have:

$$\mathbf{X}_A = \mathbf{T}\mathbf{X}_B \quad (5.18)$$

We also notice that the displacements measured in $X'-Y'$ need to be transformed back to global coordinate system $X-Y$ for the purpose of superposition. The following procedure completes the task:

$$\begin{aligned} \mathbf{U}_{(2)}(\mathbf{X}_B) &= \mathbf{T}_u^{-1} \mathbf{U}'_{(2)}(\mathbf{X}'_B) \\ &= \mathbf{T}_u^{-1} \mathbf{U}_{(1)}(\mathbf{X}_A) \\ &= \mathbf{T}_u^{-1} \mathbf{U}_{(1)}(\mathbf{T}\mathbf{X}_B) \end{aligned} \quad (5.19)$$

$$\text{where, } \mathbf{T}_u = \begin{bmatrix} \cos \alpha & \sin \alpha & 0 \\ -\sin \alpha & \cos \alpha & 0 \\ 0 & 0 & 1 \end{bmatrix} \quad (5.20)$$

is the transform matrix for displacement.

Equation (5.19) is valid for all tetrahedral elements, as long as α takes proper values:

$$\alpha = n \frac{\pi}{3}, \quad n = 0, 1, \dots, 5 \quad (5.21)$$

Equation (5.19) can be written as a general form:

$$\mathbf{U}_{(n)}(\mathbf{X}) = \mathbf{T}_{u(n)}^{-1} \mathbf{U}_{(1)}(\mathbf{T}_{(n)}\mathbf{X}), \quad n = 0, 1, \dots, 5 \quad (5.22)$$

Therefore, the displacement solution to the normal pyramid element centered at origin can be superposed as follows:

$$\mathbf{U}_P(\mathbf{X}) = \sum_{n=0}^5 \mathbf{T}_{u(n)}^{-1} \mathbf{U}_{(1)}(\mathbf{T}_{(n)}\mathbf{X}) \quad (5.23)$$

The above procedure allows us to get the solution to the pyramidal element from a solution to a single tetrahedral element, therefore, greatly simplifies the derivation. The solution set is visualized in Figure 5.6(a, b). It is clear that normal displacement U_z is axi-symmetric, it is steep in shape close to center; the tangential displacements U_x and U_y are skew-symmetric. They change the sign at the center.

5.3 The Development of Solutions to a Tangential Pyramidal Load Element

5.3.1 The Solution to Tetrahedral Element No.1 on an Equilateral Base

Consider a tangential (in positive X direction) tetrahedral load element shown in Figure 5.5. The linear load profile can be formulated as:

$$\bar{U}_{z_{-t(1)}} = \frac{1-2\nu}{4\pi G} \left\{ \left(1 - \frac{y}{b}\right) I_{S210} + \frac{1}{b} I_{S211} \right\} q_0 \quad (5.26)$$

The solution set to a tangential tetrahedral element in positive Y direction can be obtained in the similar way.

5.3.2 The Solution to Tetrahedral Element No.2 on an Equilateral Base

Next, we consider tangential load element No.2 shown in Figure 5.5. The linear load profile can be expressed as:

$$\begin{aligned} q(\xi, \eta) &= \frac{q_0}{2b} (2b + \sqrt{3}\xi - \eta) \\ &= -\frac{\sqrt{3}}{2b} q_0 (x - \xi) + \frac{q_0}{2b} (y - \eta) + q_0 \left(1 + \frac{\sqrt{3}}{2b} x - \frac{y}{2b}\right) \\ &= \underbrace{-\frac{1}{a} q_0 (x - \xi)}_{\text{Linear Part}} + \underbrace{\frac{q_0}{2b} (y - \eta)}_{\text{Linear Part}} + \underbrace{q_0 \left(1 + \frac{1}{a} x - \frac{y}{2b}\right)}_{\text{Constant Part}} \end{aligned} \quad (5.27)$$

Following the same procedure as previous section, the solution can be written as:

$$\begin{aligned} \bar{U}_{x_{-t(2)}} &= \frac{1-\nu}{2\pi G} \left\{ \left(1 + \frac{1}{a} x - \frac{y}{2b}\right) (I_{S100} + \nu_0 I_{S320}) \right. \\ &\quad \left. + \frac{1}{2b} (I_{S101} + \nu_0 I_{S321}) - \frac{1}{a} (I_{S110} + \nu_0 I_{S330}) \right\} q_0 \end{aligned} \quad (5.28)$$

$$\bar{U}_{y_{-t(2)}} = \frac{1-\nu}{2\pi G} \left\{ \left(1 + \frac{x}{a} - \frac{y}{2b} \right) I_{S311} - \frac{1}{a} I_{S321} + \frac{1}{2b} I_{S312} \right\} q_0 \quad (5.29)$$

$$\bar{U}_{z_{-t(2)}} = \frac{1-2\nu}{4\pi G} \left\{ \left(1 + \frac{x}{a} - \frac{y}{2b} \right) I_{S210} - \frac{1}{a} I_{S220} + \frac{1}{2b} I_{S211} \right\} q_0 \quad (5.30)$$

Again, the solution set to a tangential tetrahedral element in positive Y- direction can be obtained in the similar way.

5.3.3 The Solution to Tetrahedral Element No.6 on an Equilateral Base

Next, we consider tangential load element No.6 shown in Figure 5.5. The linear load profile can be expressed as:

$$\begin{aligned} q(\xi, \eta) &= \frac{q_0}{2b} (2b - \sqrt{3}\xi - \eta) \\ &= \frac{\sqrt{3}}{2b} q_0 (x - \xi) + \frac{q_0}{2b} (y - \eta) + q_0 \left(1 - \frac{\sqrt{3}}{2b} x - \frac{y}{2b} \right) \\ &= \underbrace{\frac{1}{a} q_0 (x - \xi)}_{\text{Linear Part}} + \underbrace{\frac{q_0}{2b} (y - \eta)}_{\text{Linear Part}} + \underbrace{q_0 \left(1 - \frac{1}{a} x - \frac{y}{2b} \right)}_{\text{Constant Part}} \end{aligned} \quad (5.31)$$

Following the same procedure as previous section, the solution can be written as:

$$\begin{aligned} \bar{U}_{x_{-t(6)}} &= \frac{1-\nu}{2\pi G} \left\{ \left(1 - \frac{1}{a} x - \frac{y}{2b} \right) (I_{S100} + \nu_0 I_{S320}) \right. \\ &\quad \left. + \frac{1}{a} (I_{S110} + \nu_0 I_{S330}) + \frac{1}{2b} (I_{S101} + \nu_0 I_{S321}) \right\} q_0 \end{aligned} \quad (5.32)$$

$$\bar{U}_{y_t(6)} = \frac{\nu}{2\pi G} \left\{ \left(1 - \frac{x}{a} - \frac{y}{2b} \right) I_{S311} + \frac{1}{a} I_{S321} + \frac{1}{2b} I_{S312} \right\} q_0 \quad (5.33)$$

$$\bar{U}_{z_t(6)} = \frac{1-2\nu}{4\pi G} \left\{ \left(1 - \frac{x}{a} - \frac{y}{2b} \right) I_{S210} + \frac{1}{a} I_{S220} + \frac{1}{2b} I_{S211} \right\} q_0 \quad (5.34)$$

Again, the solution set to a tangential tetrahedral element in positive Y- direction can be obtained in the similar way.

5.3.4 Construction of Solution to Tangential Pyramidal Load Element

First, superpose the solution to tetrahedral element No.1, No.2 and No.6, which together form the first half of the pyramidal element (Figure 5.5). Written as:

$$\mathbf{U}_{half}(\mathbf{X}) = \mathbf{U}_{(1)}(\mathbf{X}) + \mathbf{U}_{(2)}(\mathbf{X}) + \mathbf{U}_{(6)}(\mathbf{X}) \quad (5.35)$$

It is observed that the first half and the second half are symmetric to each other with respect to X-Z plane. This motivates us to use the property to simplify the construction of final solution.

The idea is: if $\underline{\mathbf{X}}$ is the mirror point of \mathbf{X} with respect to X-Z plane, then the displacements at point \mathbf{X} due to first half of pyramid is equal to the displacements at point $\underline{\mathbf{X}}$ due to second half of pyramid, except that the sign of

U_y should be different; the displacements at point \mathbf{X} due to second half of pyramid is equal to the displacements at point $\underline{\mathbf{X}}$ due to first half of pyramid, except that the sign of U_y should be different.

Therefore, the superposition of the two halves takes the form:

$$\mathbf{U}_P(\mathbf{X}) = \mathbf{U}_{half}(\mathbf{X}) + \mathbf{T}_h \mathbf{U}_{half}(\underline{\mathbf{X}}) \quad (5.36)$$

$$\text{where, } \mathbf{T}_h = \begin{bmatrix} 1 & 0 & 0 \\ 0 & -1 & 0 \\ 0 & 0 & 1 \end{bmatrix} \quad (5.37)$$

is the transform matrix for the solution construction purpose.

The solution to the tangential pyramidal load element are visualized in Figure 5.6(c, d).

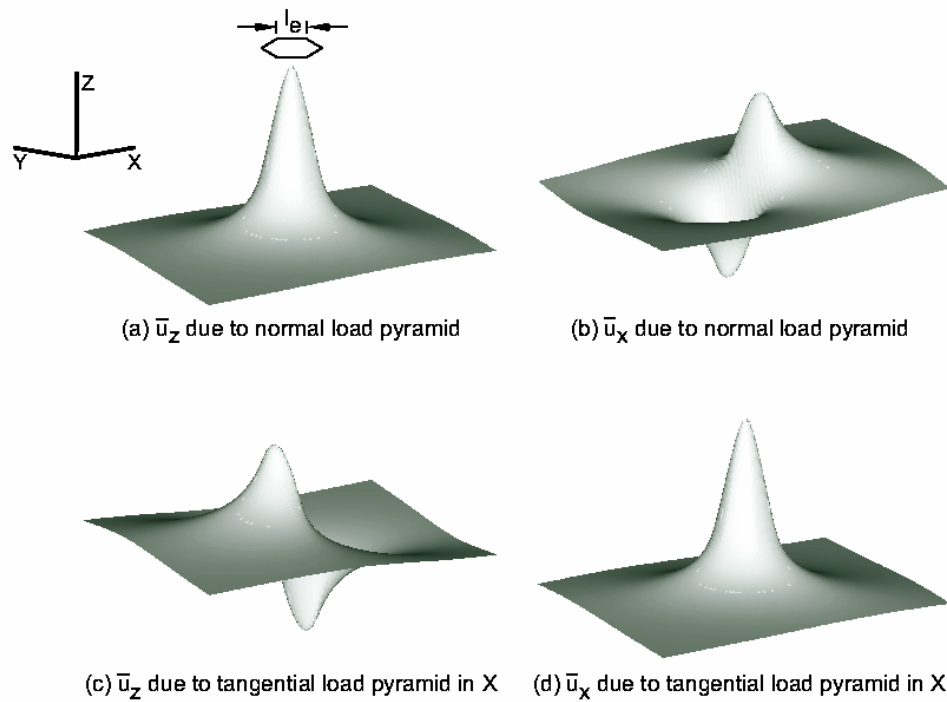


Figure 5.6 Displacement Profiles Due to a Single Pyramidal Load profile (Arbitrary Vertical Scaling): (a, b) Surface Displacements Due to Normal Load Pyramid, (c, d) Surface Displacements Due to Tangential Load Pyramid in X-Direction

Chapter 6

Discussion and Conclusion

The solution for surface displacements due to constant, linear, or bilinear load distribution over a triangular domain S has been obtained for both normal and tangential tractions. Identical equations are used to evaluate surface displacements regardless of whether the point of interest is inside or outside the domain S , consistent with the assertion of Svec and Gladwell [Svec and Gladwell, 1971]. A superposition method is suggested to construct solutions to more complicated load configurations.

The solution sets derived here have important implications for 3-D contact mechanics solution because:

- (1) The solution to linear loads over a triangular base is important in the formation of several useful loading elements, which are the key factors for a practical 3-D numerical solution. Figure 4.5 shows two of these kinds of loading elements. The solution to these loading elements can be obtained in closed form by combining some basic loading profiles (constant, linear, bilinear).

(2) Loading profiles such as those shown in Figure 4.5 provide several advantages over other load distributions or element shapes presented previously in the literature. First, the triangular footprint of the loading element allows great flexibility in capturing arbitrary loading domains S . Triangular elements can be assembled to define complicated boundaries on S , and typically the contact area can be approximated more accurately using fewer triangular elements than rectangular elements. In addition, these elements provide another advantage over other load elements. They can be employed to construct approximately a piecewise linear representation of the contact pressure (C^0 continuity of the load profile), while the constant load elements yield only a piecewise constant load description, and therefore non-continuous representation. This feature is discussed in detail in subsequent part (Part III).

These two important assets of the work presented here allow more efficient and accurate contact mechanics solutions for general 3-D contact geometries.

As discussed in subsequent part, the solution sets to normal and tangential tractions over equilateral triangular bases have been presented. Based on the fundamental work, the solution set to normal and tangential pyramidal loads have been developed, which serve as load elements in subsequent parts and play a key role in the success of Semi-Analytical Method for contact problems.

The normal load pyramid is constructed by employing the technique of coordinate rotation. Taking advantage of symmetry, only one set of solutions to a tetrahedral load element on an equilateral triangular base is used. However, the construction of tangential pyramid is more complicated, and at least three solution sets to three tetrahedral load elements are needed to construct tangential pyramidal load element.

All these work take advantage of the important properties of the solution sets derived in this part. Part of the work presented here has been reported in [Li, J. and Berger, E. J., 2001].

Part III

The Development of a Semi-Analytical Approach to 3-D Frictional Normal Contact Problem --- Non-Incremental Algorithm

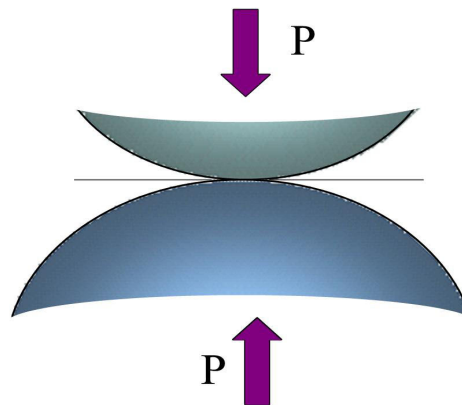
This approach treats contact phenomena as a static problem. The surface traction profiles are represented by sets of overlapping pyramidal load elements. Based on fully coupled governing equations, the algorithm of contact-detecting and stick/slip partitioning is designed as nesting iterations to fulfill contact boundary conditions. This approach requires no interpolation scheme for the field variables, which distinguishes it from other numerical techniques such as the FEM, BEM, and mesh less methods. A background grid is defined only on the contact surfaces. Computation shows that it is an efficient algorithm, which quickly shrinks initially assumed contact area to final converged area. Numerical examples are presented to show the accuracy and efficiency of the method.

Chapter 7

Contact Model and the Technique of Overlapping Load Elements

7.1 Contact Model

The problem to be solved is defined as: Frictional contact problem of two elastic bodies with arbitrary non-conformal 3-D continuous surfaces, to which only normal forces are exerted (Figure 7.1). The problem solved here is a static contact model.



Characteristics: Frictional Analysis, Arbitrary Continuous Surfaces, Dissimilar Materials

Outputs: Contact Area; Stick/Slip Zones, Surface Displacements; Tractions

Figure 7.1 The Contact Model to be Solved

7.2 The Technique of Overlapping Load Elements

Having developed the solution set to pyramidal load elements, we are ready to represent the arbitrary continuous surface traction profile by a group of pyramidal load elements. These load elements with suitable magnitudes are overlapped at the grid points of specially designed background mesh, such that the center and vertices of all the pyramids are located at grid points. The grid is defined by x-y coordinate while x and y take integer values, which is introduced in section 5.1. The scheme of overlapped pyramids on the grid points is visualized in Figure 7.2.

The reason to employ overlapped load element is to achieve approximate C^0 continuity of surface load profile. For the purpose of easy illustration, we consider the modeling method of surface load in 2-D cases. Figure 7.3 shows several models of surface load. (a) is the simple model of concentrated forces on discrete nodes, the sum of which is equal to the total load; (b) is the piecewise constant model, the sum of area of each bar represents the total load; (c) represents a piecewise continuous model or C^0 continuity curve, the area under the curve equals the total load; (d) is C^n ($n \geq 1$) continuous mathematical model.

In elasticity, the surface load such as (a) and (b) will lead to discontinuity of displacement fields. Although these models are used in many numerical methods such as FEA, generally speaking, they are not good for contact analysis.

If the contact surfaces are C^n continuous, obviously (d) is the best way to model surface tractions. However, as discussed in Chapter 2, very limited contact configurations can be solved analytically using such mathematical models. Therefore, (c) is the best model from a practical point of view.

The C^0 continuous representation is approximately achieved by a group of overlapped triangle load elements, the solutions of which are known and continuous, as shown in Figure 7.4. Denote by $f(x)$ the C^n continuous curve to be approximated; by p_i the height of i^{th} triangular element, by a the spacing between adjacent nodes. The height p_i takes the value of curve $f(x)$ at node x_i :

$$p_i = f(x_i) \quad (7.1)$$

It can be easily shown that:

$$\lim_{n \rightarrow \infty} \sum_{i=1}^n ap_i = \int_{b_1}^{b_2} f(x) dx \quad (7.2)$$

where, a is grid spacing, or half of the length of triangular side on X axis, ap_i is the area of i^{th} triangle, and the integral on the right hand side represent the area under curve $f(x)$. Therefore, the C^n curve is represented by a set of discrete points p_i ($i=0, 1, 2, \dots, n, n+1$). The area under curve $f(x)$ is approximated by the sum of area of a set of overlapped triangles with magnitude $p_i=f(x_i)$. In 3-D cases, we use pyramidal load elements instead of triangles. The above argument can be used in 3-D case in an analogous manner.

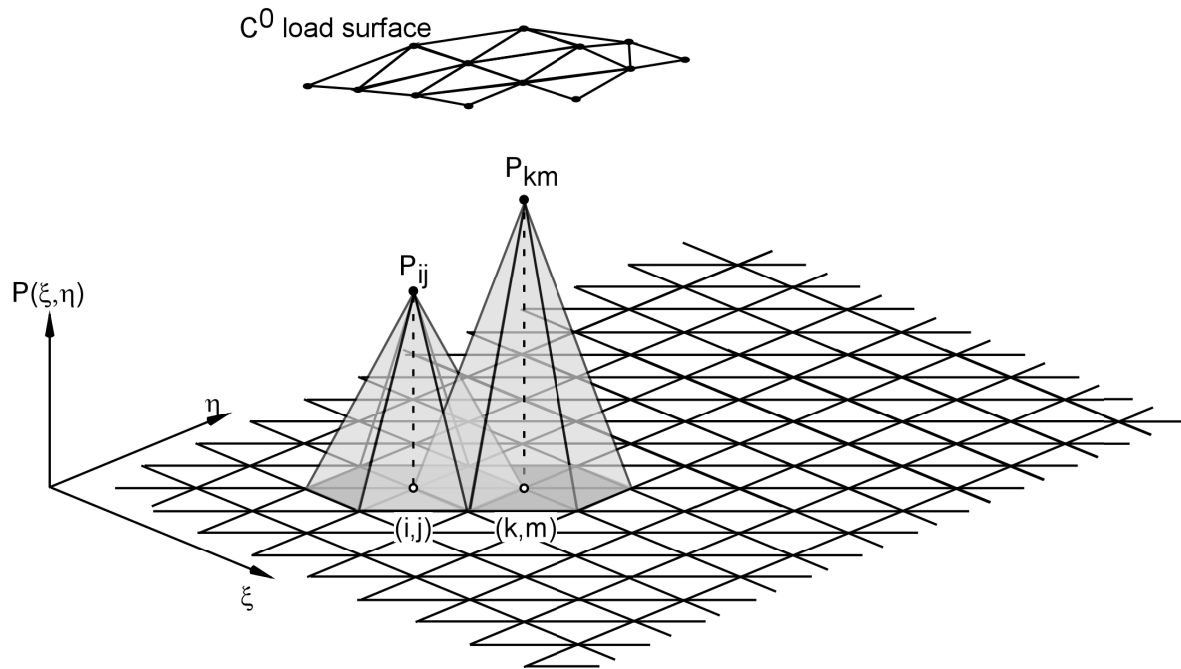


Figure 7.2 Overlapped Pyramidal Load Elements to Approximate C^0 Continuity Loading Profile; Adjacent Load Pyramids with Vertices at (ξ_i, η_j) and (ξ_k, η_m) Have Nodal Pressure values p_{ij} and p_{km} , Respectively

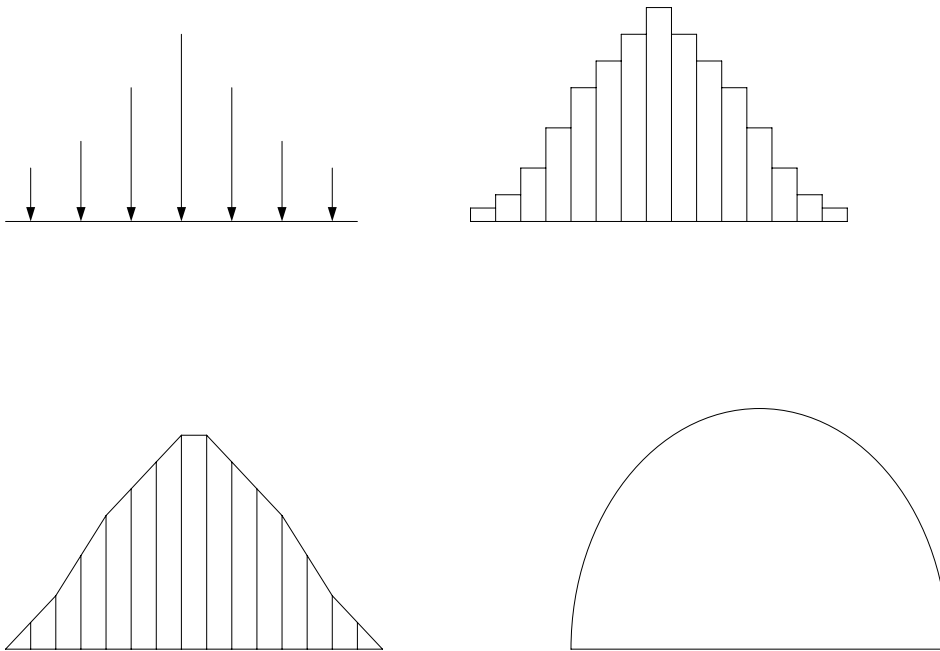


Figure 7.3 Modeling of Surface Load (a) Concentrated Forces; (b) Piecewise Constant; (c) C^0 Continuity; (d) C^n ($n \geq 1$) Continuity

As shown in Figure 7.2, we use a set of pyramids with magnitude p_{ij} at grid points. p_{ij} takes the value of load profile at node ij , written as:

$$p_{ij} = f(x_i, y_j) \tag{a) Concentrated Loads} \tag{7.3}$$

Similar to 2-D case, it can also be shown that:

$$\lim_{\substack{n \rightarrow \infty \\ m \rightarrow \infty}} \sum_{i=1}^n \sum_{j=1}^m \frac{\sqrt{3}}{2} l_e^2 p_{ij} = \iint_S f(x, y) dx dy \tag{7.4}$$

where, l_e is grid spacing, or the side length of hexagonal base of pyramid, $\frac{\sqrt{3}}{2}l_e^2 p_{ij}$ is the volume of pyramid ij , and the integral on right hand side is the volume under profile $f(x, y)$. This argument also applies to any arbitrary specified local area, which means that the sufficient number of pyramids can catch interesting detail of any load profile. In this way, C^n load profile $f(x,y)$ is represented by a set of discrete point p_{ij} , and the volume under profile $f(x,y)$ (the total global force) is approximated by the linear function of p_{ij} , which allow us to linearize system equations with minimal sacrifice of continuity of load profile.

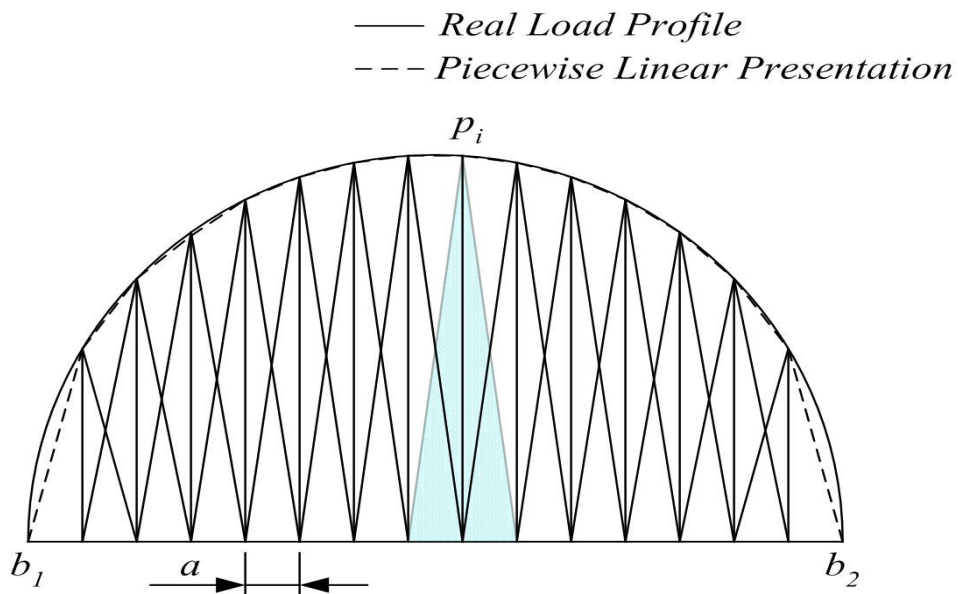


Figure 7.4 A Set of Overlapped Triangular Elements Approximates Continuous Surface Load Profile

Chapter 8

Algorithms for Contact Area Detecting, Stick/Slip Zone Partitioning, and Field Variables Computation

In this chapter, we develop equations for surface displacements due to normal and tangential surface tractions respectively. We also derive the equations governing contact area calculations, and conditions that allow us to partition the total contact area into stick and slip regions. Finally, the iteration scheme for the contact solutions is presented. The fundamental idea is to present surface tractions raised by contact by a set of overlapped pyramid load elements (Figure 7.2), which has been introduced in Chapter 7. The coordinate systems used in the development of system equations have already been introduced in chapter 5. Please refer to section 5.1 and Figure 5.1.

Because the system equations are based on the displacement solutions to a normal and two tangential loading elements, we introduce the following

notations: \bar{U}_{z-p} is the surface displacement solution in z direction due to a normal traction pyramid with unit amplitude centered at origin, given by:

$$\bar{U}_{z-p} = \frac{1-\nu}{2\pi G} C(X,Y) \quad (8.1)$$

where $C(X,Y)$ (and subsequent similar functions to be defined) are influence functions of surface location. This idea is extended by defining the other notations in Table 8.1.

Table 8.1 Displacement Fields Due to Unit Pyramid Traction Elements

Load Type	Z-Displacement	X-Displacement	Y-Displacement
Normal	$\bar{U}_{z-p} = aC(X,Y)$	$\bar{U}_{x-p} = -bD(X,Y)$	$\bar{U}_{y-p} = -bE(X,Y)$
Tangential in X	$\bar{U}_{z-qx} = bF(X,Y)$	$\bar{U}_{x-qx} = aG(X,Y,\nu_0)$	$\bar{U}_{y-qx} = cH(X,Y)$
Tangential in Y	$\bar{U}_{z-qy} = bI(X,Y)$	$\bar{U}_{x-qy} = cJ(X,Y)$	$\bar{U}_{y-qy} = aK(X,Y,\nu_0)$

Note: $\nu_0 = \frac{\nu}{1-\nu}$, $a = \frac{1-\nu}{2\pi G}$, $b = \frac{1-2\nu}{4\pi G}$, $c = \frac{\nu}{2\pi G}$

We notice that coefficients G and K are not only the function of surface location, but also of ν_0 . Computational result (See Table 8.2) shows that Poisson's ratio ν has remarkable effect on coefficient G . The peak value of $G(X, Y, \nu_0)$ changes 38% between $\nu = 0$ and $\nu = 0.27$. However, when ν varies from 0.27 to 0.32 (which

covers the majority of metals), the peak value of $G(X, Y, \nu_0)$ only changes 0.88%. Coefficient K varies according to ν in the same manner as G . In the contact problem that two different materials involved, using the average formula (Table 8.2) gives very good approximation.

Table 8.2 The effect of Poisson's ratio on $G(X, Y, \nu_0)$

ν	Normalized Peak value of $G(X, Y, \nu_0)$
0	1.0
0.27	1.3775
0.32	1.3896
$\nu_1=0.27, \nu_2=0.32, \text{ use average:}$ $\nu_0 = \frac{1}{2} \left(\frac{\nu_1}{1-\nu_1} + \frac{\nu_2}{1-\nu_2} \right)$	1.3836

In subsequent discussion, we use modified average value for the two-body contact problems, so that we calculate a single $G(X, Y, \nu_0)$ and $K(X, Y, \nu_0)$, instead of one influence function for each body. It is shown later that this approach brings us convenience in writing system equations in a neat way without introducing significant error.

8.1 Surface Displacements Due to Normal Traction

If we denote by \bar{U}_{ijkm} the surface displacement at point (X_i, Y_j) due to the existence of a pyramid loading element with amplitude P_{km} at point (ξ_k, η_m) , then the following relationships hold:

$$\bar{U}_{ijkm,Z} = \bar{U}_{Z-p}(X_i - \xi_k, Y_j - \eta_m)P_{km} = \frac{1-\nu}{2\pi G} C_{ijkm} P_{km} \quad (8.2)$$

where C_{ijkm} is an influence coefficient, the meaning of which is defined in Table

8.1. Similarly, we can write:

$$\bar{U}_{ijkm,X} = -\frac{1-2\nu}{4\pi G} D_{ijkm} P_{km} \quad (8.3)$$

$$\bar{U}_{ijkm,Y} = -\frac{1-2\nu}{4\pi G} E_{ijkm} P_{km} \quad (8.4)$$

with D_{ijkm} and E_{ijkm} having similar interpretations as influence coefficients relating loading at one location to displacement at another. Recall that this family of influence coefficients $(C,D,E)_{ijkm}$ can be determined using the analytical solutions provided earlier.

The displacements at the point (X_i, Y_j) can be expressed as a summation over all of the load points (k,m) :

$$\bar{U}_{ij,Z} = \frac{1-\nu}{2\pi G} \sum_k \sum_m C_{ijkm} P_{km} \quad (8.5)$$

$$\bar{U}_{ij,X} = -\frac{1-2\nu}{4\pi G} \sum_k \sum_m D_{ijkm} P_{km} \quad (8.6)$$

$$\bar{U}_{ij,Y} = -\frac{1-2\nu}{4\pi G} \sum_k \sum_m E_{ijkm} P_{km} \quad (8.7)$$

Further, the special case of displacement at the origin will be of interest and discussed subsequently; as such, we define for $(X=0, Y=0)$:

$$\begin{aligned} \bar{U}_{00km,Z} - \bar{U}_{ijkm,Z} &= \frac{1-\nu}{2\pi G} \underbrace{(C_{00km} - C_{ijkm})}_{-\hat{C}_{ijkm}} P_{km} \\ &= -\frac{1-\nu}{2\pi G} \hat{C}_{ijkm} P_{km} \end{aligned} \quad (8.8)$$

$$\bar{U}_{00km,X} - \bar{U}_{ijkm,X} = \frac{1-2\nu}{4\pi G} \hat{D}_{ijkm} P_{km} \quad (8.9)$$

$$\bar{U}_{00km,Y} - \bar{U}_{ijkm,Y} = \frac{1-2\nu}{4\pi G} \hat{E}_{ijkm} P_{km} \quad (8.10)$$

where the operators \hat{D}_{ijkm} and \hat{E}_{ijkm} are defined in an analogous manner to \hat{C}_{ijkm} for the X- and Y-direction deflections, respectively.

8.2 Surface Displacements Due to Tangential Traction

Consider next a tangential load distribution in the X- or Y-direction given by q_x or q_y . The tangential surface displacement due to tangential traction pyramid in X-direction with amplitude of $q_{km,X}$ at location (ξ_k, η_m) can be written as:

$$\bar{U}_{00km,z} - \bar{U}_{ijkm,z} = -\frac{1-2\nu}{4\pi G} \hat{F}_{ijkm} q_{km,X} \quad (8.11)$$

$$\bar{U}_{00km,X} - \bar{U}_{ijkm,X} = -\frac{1-\nu}{2\pi G} \hat{G}_{ijkm} q_{km,X} \quad (8.12)$$

$$\bar{U}_{00km,Y} - \bar{U}_{ijkm,Y} = -\frac{\nu}{2\pi G} \hat{H}_{ijkm} q_{km,X} \quad (8.13)$$

and the similar equations for the Y-direction are:

$$\bar{U}_{00km,z} - \bar{U}_{ijkm,z} = -\frac{1-2\nu}{4\pi G} \hat{I}_{ijkm} q_{km,Y} \quad (8.14)$$

$$\bar{U}_{00km,X} - \bar{U}_{ijkm,X} = -\frac{\nu}{2\pi G} \hat{J}_{ijkm} q_{km,Y} \quad (8.15)$$

$$\bar{U}_{00km,Y} - \bar{U}_{ijkm,Y} = -\frac{1-\nu}{2\pi G} \hat{K}_{ijkm} q_{km,Y} \quad (8.16)$$

8.3 Governing Equations for a Point to Fall within the Contact Area

Next, we consider two elastic bodies in normal approach, and we denote by $\bar{U}_{1,z}$ the normal displacement of body one at surface point (X, Y) , where a positive displacement is directed into body one. Further, we denote by $\bar{U}_{2,z}$ the normal displacement of body two at surface point (X, Y) , where a positive displacement is directed into body two. $h(X, Y)$ is defined as the separation distance between surface points of two bodies, when they come into contact with the external forces are zero. Figure 8.1 shows the normal contact configuration and the surface separation $h(X, Y)$ of the two bodies.

If a surface point (X, Y) falls within the contact area, then:

$$\bar{U}_{1,z}(X, Y) + \bar{U}_{2,z}(X, Y) + h(X, Y) = \Delta_z = \bar{U}_{1,z}(0, 0) + \bar{U}_{2,z}(0, 0) \quad (8.17)$$

where Δ_Z is the normal approach (i.e., surface interpenetration) of the centers of bodies one and two and is equivalent to the sum of the centerline displacements of bodies one and two at the surface. Equation (8.17) can be rewritten as:

$$[\bar{U}_{1,Z}(0,0) - \bar{U}_{1,Z}(X,Y)] + [\bar{U}_{2,Z}(0,0) - \bar{U}_{2,Z}(X,Y)] = h(X,Y) \quad (8.18)$$

which, when combined with equations (8.8), (8.11) and (8.14), yields the fully coupled equations for the surface normal displacement:

$$\lambda_1 \sum_k \sum_m \hat{C}_{ijkm} P_{km} + \lambda_2 \sum_k \sum_m \hat{F}_{ijkm} q_{km,X} + \lambda_2 \sum_k \sum_m \hat{I}_{ijkm} q_{km,Y} \quad (8.19)$$

$$\begin{cases} = -h(X,Y) & \text{inside } S \\ > -h(X,Y) & \text{outside } S \end{cases}$$

where

$$\lambda_1 = \frac{1-\nu_1}{2\pi G_1} + \frac{1-\nu_2}{2\pi G_2} \quad (8.20)$$

$$\lambda_2 = \frac{1-2\nu_1}{4\pi G_1} - \frac{1-2\nu_2}{4\pi G_2} \quad (8.21)$$

Note that the tangential traction expressions $q_{km,X}$ and $q_{km,Y}$ appear explicitly in the equations which determine contact area. Their relative importance in this equation (which will be discussed in the section on numerical results) is defined by the magnitude of the individual influence coefficients relating tangential tractions to normal surface displacements. Equilibrium in the Z-direction also requires the force balance constraint:

$$A_p \sum_k \sum_m P_{km} = P \quad (8.22)$$

where $A_p = \frac{\sqrt{3}}{2} l_e^2$ is the characteristic volume of a pyramid of uniform hexagonal base and unit height, and P is the total normal load applied to the contacting bodies.

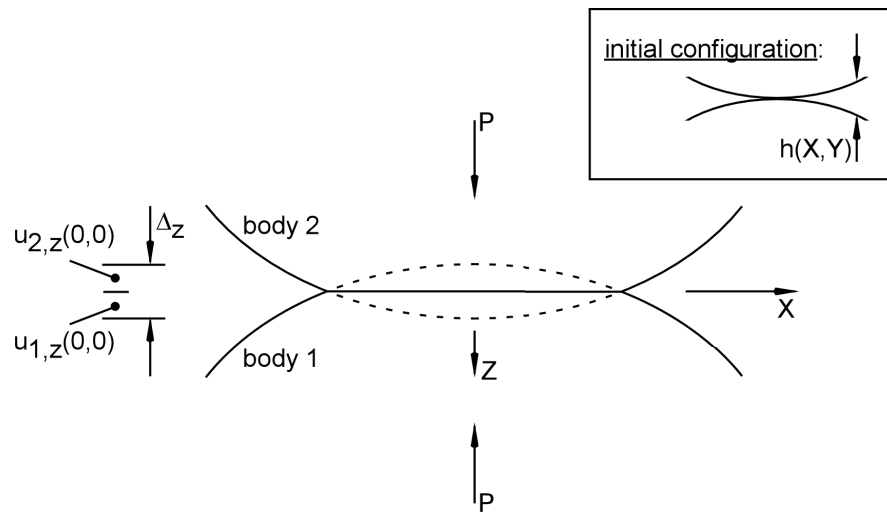


Figure 8.1 Relationships Among Far-Field Normal Motion Δz , Surface Displacements $\bar{U}_{1,z}$ and $\bar{U}_{2,z}$; Inset: Separation Distance $h(X,Y)$ Measured from the Initial Configuration

8.4 Governing Equations for a Point to Fall into Sticking Area

Consider a pair of surface points A_1 and A_2 on bodies one and two, respectively, which were coincident before external loads are applied; see Figure 8.2. Denote the X-direction motion of the centers of the two bodies as $\delta_{1,x}$ and $\delta_{2,x}$, and the X-direction tangential displacements of points A_1 and A_2 as $\bar{U}_{1,x}$ and $\bar{U}_{2,x}$. If this pair of surface points is in a sticking condition in the X-direction, then:

$$\bar{U}_{1,x}(X,Y) - \bar{U}_{2,x}(X,Y) = \delta_{1,x} - \delta_{2,x} = \Delta_x \quad (8.23)$$

This can again be rewritten taking advantage of equation (8.9), (8.12) and (8.15).

In sticking regions, the points A_1 and A_2 remain coincident, $\Delta_{1,x} - \Delta_{2,x} = 0$; recognizing that the displacements can be written relative to displacements at the origin $\bar{U}_{1,x}(0,0)$ and $\bar{U}_{2,x}(0,0)$, we write:

$$\underline{X-direction}: \lambda_3 \sum_k \sum_m \hat{D}_{ijkm} P_{km} - \lambda_4 \sum_k \sum_m \hat{G}_{ijkm} q_{km,x} - \lambda_5 \sum_k \sum_m \hat{J}_{ijkm} q_{km,y} = 0 \quad (8.24)$$

where

$$\lambda_3 = \frac{1-2\nu_1}{4\pi G_1} - \frac{1-2\nu_2}{4\pi G_2} \quad (8.25)$$

$$\lambda_4 = \frac{1-\nu_1}{2\pi G_1} + \frac{1-\nu_2}{2\pi G_2} \quad (8.26)$$

$$\lambda_5 = \frac{\nu_1}{2\pi G_1} + \frac{\nu_2}{2\pi G_2} \quad (8.27)$$

For sticking in the Y-direction, we can again define a bulk relative displacement in the Y-direction as $\Delta_Y = \delta_{1,Y} - \delta_{2,Y}$. Following the same procedure, we can write the governing equation in Y- direction:

$$\underline{Y - direction}: \lambda_3 \sum_k \sum_m \hat{E}_{ijkm} P_{km} - \lambda_5 \sum_k \sum_m \hat{H}_{ijkm} q_{km,X} - \lambda_4 \sum_k \sum_m \hat{K}_{ijkm} q_{km,Y} = 0 \quad (8.28)$$

with λ_3 , λ_4 and λ_5 having the same expressions as equations (8.25~8.27).

In the slipping regions, the loads are defined by the Coulomb friction equality:

$$q_{km,X} = \mu_X P_{km} \quad (8.29)$$

$$q_{km,Y} = \mu_Y P_{km} \quad (8.30)$$

where we introduce a vector notation for the friction coefficient defined as:

$$\vec{\mu} = \mu_X \vec{i} + \mu_Y \vec{j} \Rightarrow \vec{q}_{km} = \vec{\mu} P_{km} \quad (8.31)$$

The resultant friction coefficient has magnitude:

$$\mu_o = \sqrt{\mu_X^2 + \mu_Y^2} \quad (8.32)$$

The vector components can be expressed as:

$$\mu_X = \frac{q_X}{q_o} \mu_o \quad (8.33)$$

$$\mu_Y = \frac{q_Y}{q_o} \mu_o \quad (8.34)$$

where $q_o = \sqrt{q_X^2 + q_Y^2}$ is the resultant tangential traction magnitude, and the direction of the friction coefficient vector at any contact point is opposite the

direction of relative motion at that point. Since q_x and q_y are the unknowns in system equations, we cannot use above relations to obtain μ_x and μ_y directly. We then use the result from previous iterative step to compute μ_x and μ_y in current step. That is:

$$\mu_x(i) = \frac{q_x(i-1)}{q_o(i-1)} \mu_o \quad (8.35)$$

$$\mu_y(i) = \frac{q_y(i-1)}{q_o(i-1)} \mu_o \quad (8.36)$$

where, i is the index of iteration. In the beginning of iteration scheme, vector $\bar{\mu}$ is set in the direction of radius.

Finally, the overall tangential force balance of the system requires:

$$A_p \sum_k \sum_m q_{km,X} = Q_X \quad (8.37)$$

$$A_p \sum_k \sum_m q_{km,Y} = Q_Y \quad (8.38)$$

where Q_X and Q_Y are the total tangential loads applied to the two contacting bodies.

We note that in the slipping regions, the two points A_1 and A_2 do not remain coincident, and the extent of their relative motion is determined by the elastic

responses of the two materials, and the sliding friction shear stress at the interface.

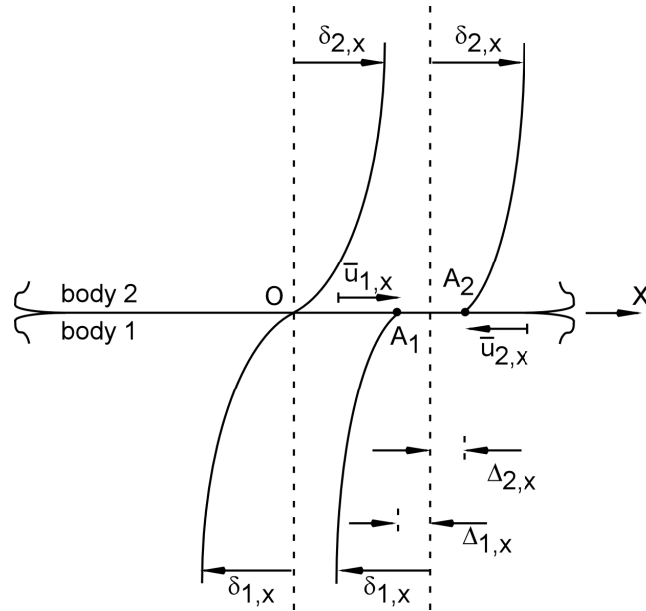


Figure 8.2 Tangential Interface Behavior Showing Points A_1 and A_2 , Originally Coincident, Undergoing Tangential Displacements $\bar{u}_{1,x}$ and $\bar{u}_{2,x}$. Sticking Regions Can Be Determined by Considering Interface Displacements Relative to Far-Field Displacements $\delta_{1,x}$ and $\delta_{2,x}$

8.5 Discrete Equations

Based upon the preceding discussion, the discrete system equations can be stated. The unknowns in this approach are the interface normal and tangential tractions at the nodes on the contact surface, P_{ij} , $q_{ij,x}$, $q_{ij,y}$ for all (i,j) on the contact surface. For N surface nodes, this results in $3N$ unknowns. The traction-

displacement equations (8.19, 8.24 and 8.28) contribute $3N-3$ equations, which are supplemented by the three force balance equations (8.22), (8.37), and (8.38). The coefficient matrix for the unknowns is constructed from the operators C_{ijklm} , D_{ijklm} , ... K_{ijklm} as well as the scalars $\lambda_i; i=1, \dots, 4$ described earlier in this section. Note that because the influence functions are constructed from analytical elasticity solutions, the coefficient matrix arising from these equations is fully populated. The surface displacement due to a point load on a half-space only goes to zero asymptotically as we move infinitely far from the load application point. While this implicit satisfaction of displacement boundary conditions does provide some modeling and discretization advantages (as described later), it also limits our use of sparse matrix storage approaches and sparse solvers. The coefficient matrix in this approach does not emerge with a banded characteristic of, for example, structured FEM techniques. Nonetheless, overall system equations of the form

$$[A]\{x\} = \{B\} \quad (8.39)$$

where $\{x\}^T = \{p_{ij}, q_{ij,x}, q_{ij,y}\}$ for all (i,j) node locations, can be assembled and solved at each iteration, and ultimately a convergent solution for contact area and stick zone size can be achieved.

8.6 Numerical Approach

There are three essential considerations in developing a numerical approach which takes full advantage of the analytical solutions presented here. There are two implementation/iteration issues related to (A) contact size and (B) stick zone size. The third consideration is load stepping and potential path dependence of the numerical solution. A substantial body of literature has addressed the path dependence issue [see related discussion on existence and uniqueness in the Chapter 2], so we first consider the nature of the solutions to the problem at hand. In the dissertation, we apply a novel semi-analytical strategy to solve normal contact problems with friction, in which the normal load is applied both quasi-statically and monotonically, with no global tangential loading. In solving axisymmetric indentation problems under these conditions, Spence [Spence, 1968] developed self-similar solutions which show that in fact the solution is unique (i.e., independent of load path), even in the presence of friction. He later reported [Spence 1975] axisymmetric indentation results valid for any power law indenters, which are functions of geometry, material properties, friction coefficient, and loading, and independent of load path. Non-axisymmetric indentation (as in one of the examples presented later) can be accommodated by Spence's framework as well, but a more general argument can be made in light of the work of Saeedvafa & Dundurs [Saeedvafa and Dundurs, 1988]. From their detailed examination of load paths, we can conclude that the normal contact problem with friction and no global tangential loading is essentially path-independent (their Regimes I and II). We therefore do not implement any load

stepping in the algorithm presented here, focusing rather on the iterations for contact size and stick zone size. Figure 8.3 highlights the nested looping structure with iteration on (A) contact area and (B) stick area, as described next.

A: Iteration on contact area

Iteration on the contact area is determined based upon the contact pressure constraint:

$$p_{ij} \geq 0 \quad \forall (i,j) \in S \quad (8.40)$$

for all (i,j) in S [where the force balance equation (8.22) is implicitly satisfied by solutions of the linear system (8.39)]. Iteration on the contact area involves taking the current contact area, calculating contact tractions based upon the stick or slip status of each contact node, and comparing the calculated contact tractions with constraint (8.40). If any $p_{ij} < 0$, then the contact area S is adjusted to include fewer nodes (i,j) as appropriate, and the calculations continue until the result converges. The contact area is then indicated by the boundary separating regions of $p_{ij}=0$ from non-zero pressures. As we shall see later, this approach allows determination of the contact size to an accuracy on the order of at least $l_q/3$, and in some cases much better.

B: Iteration on sticking area

The algorithm for iteration on stick zone within the contact area includes the nested iteration on contact domain S . Further, we employ a checking procedure which partitions the contact into sticking and slipping regions for the next iteration step according to the constraint:

$$|\bar{q}(X_i, Y_j)| \leq \mu_0 p(X_i, Y_j) \quad (8.41)$$

If the above constraint is satisfied, the node falls into the stick area. Otherwise, the node falls into the slip area. The iteration is continued by comparing solutions of the system equations (8.39) to this constraint, and adjusting the stick area until a consistent solution is obtained.

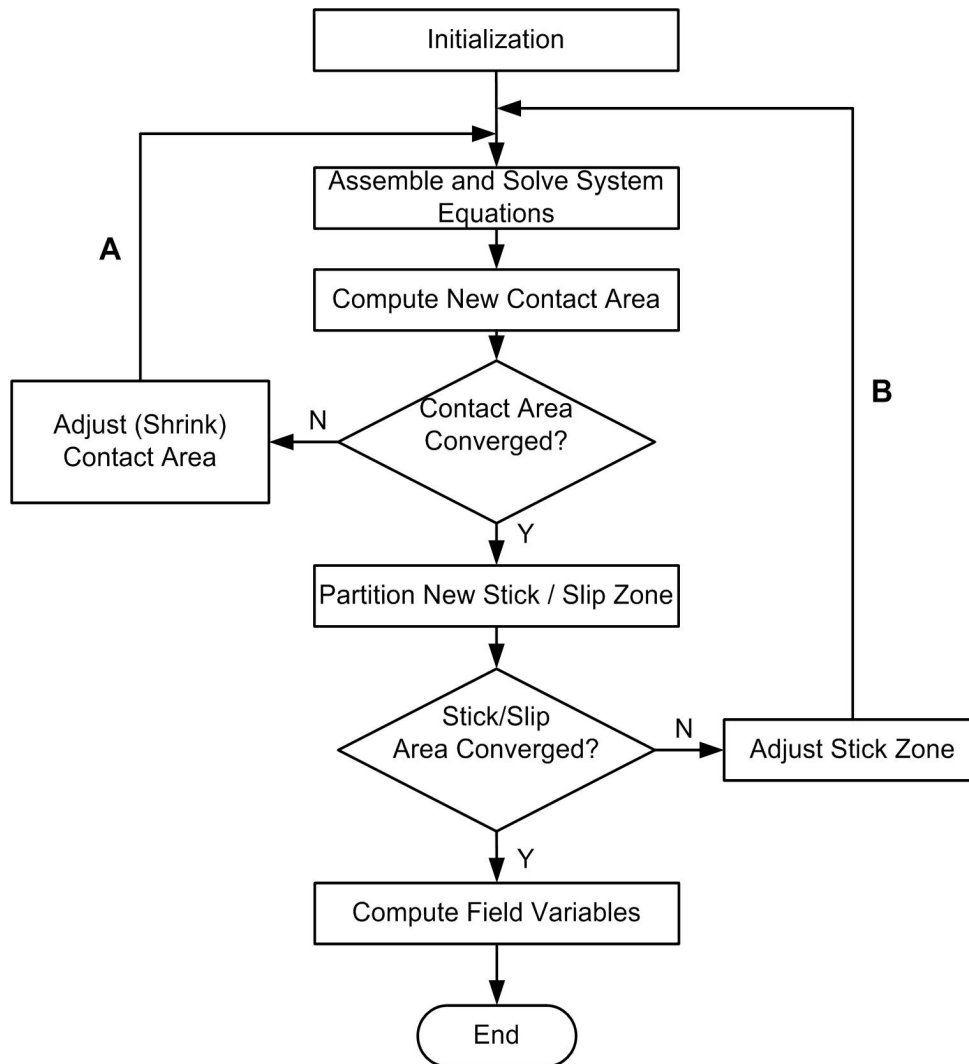


Figure 8.3 Flowchart for the Numerical Solution. An Internal Loop over Contact Area (A) Is Nested Within the Stick-Slip Region Iteration (B).

Chapter 9

Numerical Examples

The algorithm presented here has been implemented into a numerical framework and used to examine several example problems. The intent of this section is to look at several specific cases for which analytical solutions or previous numerical solutions are available to evaluate the accuracy and convergence behavior of the proposed method.

9.1 Normal Contact of Elastic Spheres Without Friction

First, consider the case of two dissimilar elastic spheres in normal contact, without friction, under a total normal load $P = 1000$ N. This example has been chosen to evaluate the validity of the equation formulation as well as the contact area iteration procedure.

Table 9.1 Properties of Material and Geometries

No.	Material	E ($\times 10^9$ N/m ²)	ν	Radius (m)
1	Steel, S.A.E 4068	206.84	0.27	0.100
2	Stainless	193.05	0.27	0.150

The algorithm presented here determines whether each surface node is within the contact area S , and therefore if we define the boundary of the contact area S simply by connecting the surface nodes (using nodes just inside S), then the contact region is defined by a piecewise linear function. Since we know that in this case the contact area is indeed a circle, we use a least-squares approach to define the best-fit circle to the solution.

$$a_i = \sqrt{X_i^2 + Y_i^2} + \frac{l_e}{2} \quad (9.1)$$

is the i^{th} radius estimate, and a is the estimated radius of the contact area given by:

$$a = \frac{1}{m} \sum_{i=1}^m a_i \quad (9.2)$$

Table 9.2 gives several computational results for various background meshes. A typical mesh scheme is shown in Figure 9.1. It will be useful to define two additional accuracy parameters, both of which measure errors related to the contact area S .

The radius error is defined as:

$$E_a = \frac{|a - a_o|}{a_o} \quad (9.3)$$

The radius standard deviation is defined as:

$$\sigma = \sqrt{\frac{\sum_{i=1}^m (a_i - a)^2}{m}} \quad (9.4)$$

where m is the number of points defining the contact area.

Table 9.2 Convergence Study, No Friction Case

Number of Initial Nodes	Length of Triangle sides ($\times 10^{-4}$ m)	Maximum Normal Traction ($\times 10^8$ N/m ²)	Contact Area, Radius a ($\times 10^{-4}$ m)	Wall Clock Time of Computation
11×11	2	8.573573	7.671789	Immediate
21×21	1	8.551941	7.341638	Immediate
31×31	0.75	8.547610	7.491091	1.5 min
41×41	0.50	8.545378	7.481721	8min
51×51	0.40	8.544563	7.466225	18min
Hertz's Solution		8.543278	7.475813	

Table 9.2 shows the convergence of the numerical solution as a function of mesh parameter l_e . Both contact pressure p/p_0 and contact radius a/a_0 converge quickly to the analytical solution, and the two error estimates also approach zero as the mesh is refined. We note that a convergent solution for the Hertz problem is obtained when the grid spacing becomes sufficiently small, say $l_e/a_0 \leq 0.1$.

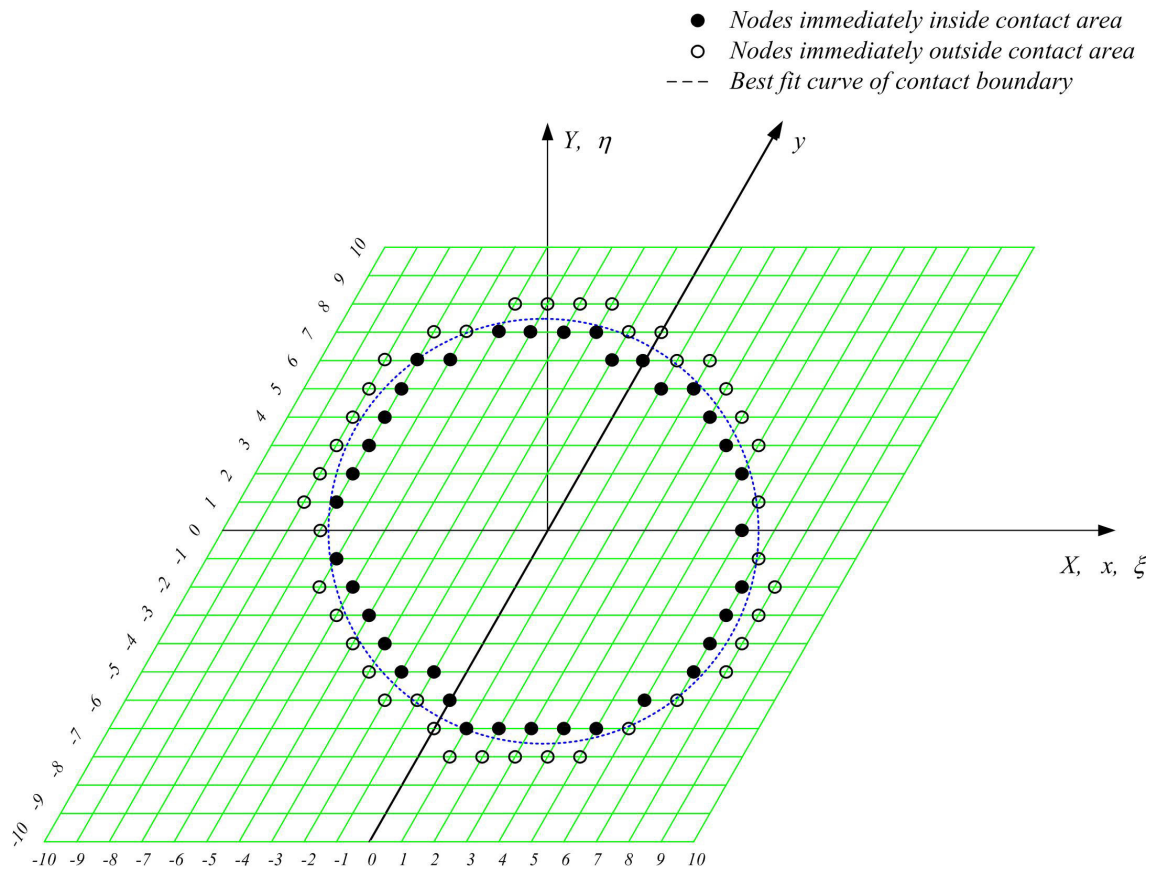


Figure 9.1 The Background Mesh and Curve Fit for Contact Area

9.2 Normal Contact of Elastic Spheres With Friction

We now examine the case of normal contact of dissimilar elastic bodies with friction under the action of an applied normal load P , with zero tangential load, $Q_x=Q_y=0$. Two recent numerical approaches [Kosior, F., Guyot, N., and Maurice,

G. 1999], [Guyot, N., Kosior, F., and Maurice, G., 2000], as well as an earlier analytical approach [Spence, D. A., 1975], provide results for comparison with the method described here. We consider two cases (one for each of the two numerical works cited above), both of which can be compared to the analytical solution of Spence. Two different mesh spacings were used to compare with the numerical results. The physical lengths of the nodal spacing are $l_e^1 = 3.5 \times 10^{-6}$ m and $l_e^2 = 5 \times 10^{-6}$ m, both of which are similar to the characteristic mesh sizes cited in [Kosior, F., Guyot, N., and Maurice, G. 1999], [Guyot, N., Kosior, F., and Maurice, G., 2000].

A typical numerical result for the calculation of resultant tangential traction q_o is shown in Figure 9.2, a 3-D contour plot in which the height of the contour indicates its value. Outside the contact zone, beyond the circular boundary of diameter $2a$, the tangential traction is identically zero, while within the contact zone it varies depending upon the local sticking or slipping state. In the slip annulus defined by $c < r < a$ (where r is a radial location measured from the center of contact), the tangential traction scales with the contact pressure by Coulomb's law, $q_o(X, Y) = \mu_o P(X, Y)$. Within the sticking region, $r < c$, the tangential traction does not scale directly with contact pressure, but rather locally assumes a value which allows for overall force equilibrium in the tangential direction. We finally

note that exactly at the center of contact $r=0$, the tangential traction falls to zero, as this is a point of symmetry in the geometry and loading.

Table 9.3 Numerical Result Compared with Previous Analytical and Numerical Solutions

Conditions		Method	p_0 (MPa)	a (μm)	c/a
P = 10N	$\mu = 0.0$	This Method	2092.5	47.40	
		Guyot	2133.4	47.80	
		Hertz	2091.4	47.78	
	$\mu = 0.1$	This Method	2154.2	46.61	0.511
		Guyot	2156.6	47.50	0.690
		Spence	-	-	0.530
	$\mu = 0.6$	This Method	2154.2	46.61	0.978
		Guyot	2169.7	47.50	0.990
		Spence	-	-	0.999
P = 31.5N	$\mu = 0.0$	This Method	3068.3	70.28	-
		Kosior	3069.0	70.70	-
		Hertz	3065.8	70.04	-
	$\mu = 0.1$	This Method	3163.8	68.43	0.533
		Kosior	3147.0	68.80	0.545
		Spence	-	-	0.535
	$\mu = 0.6$	This Method	3163.8	68.43	0.980
		Kosior	3167.0	67.60	0.961
		Spence	-	-	0.999

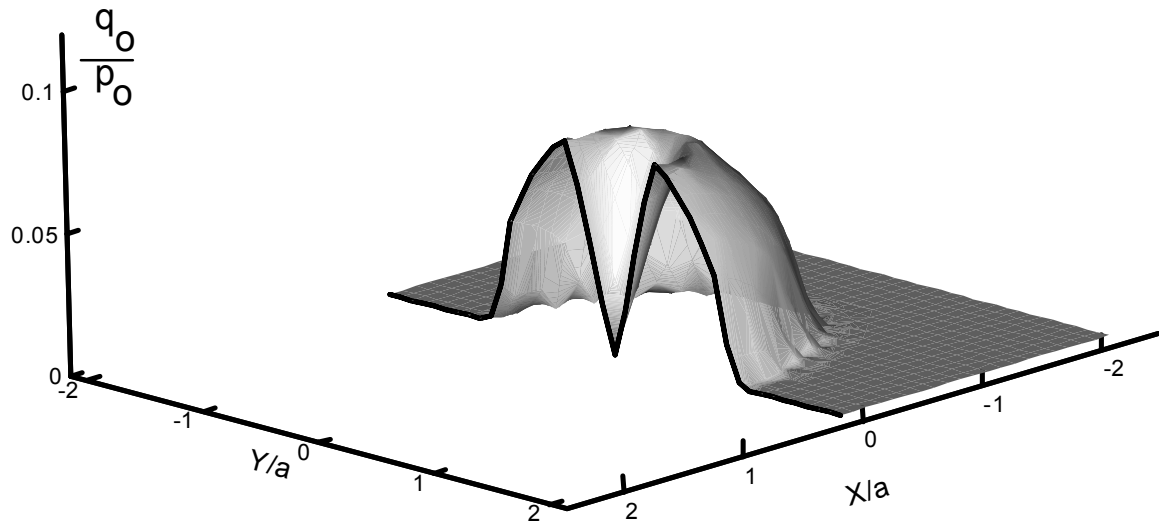


Figure 9.2 Contour Plot of Tangential Interface Traction q_0 for Normal Indentation of Dissimilar Materials (with Friction)

9.3 Contact of Crossed Elastic Cylinders

We next consider the contact of crossed elastic cylinders, a non-axisymmetric normal indentation problem which will test the robustness of the approach presented here. Two long, elastic cylinders of radius R_1 and R_2 with axes oriented at an angle ϕ are pressed together by a normal load P with no global tangential load. We consider one steel cylinder of radius $R_1 = 75$ mm, and one aluminum cylinder of radius $R_2 = 50$ mm, loaded by a normal force of $P = 10$ kN. The contact shape for a crossed cylinder contact problem is an ellipse of major semi-axis a and minor semi-axis b oriented at an angle θ from the x -axis, and in general $\theta \neq \phi$ (see the Appendix for an approximate analysis of the relationship

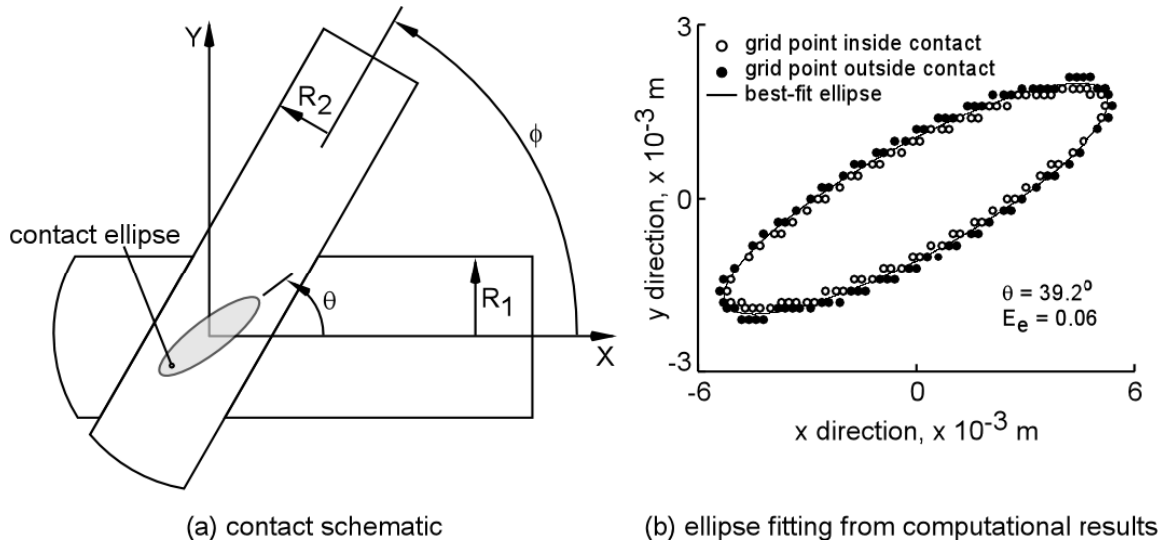


Figure 9.3 Crossed Cylinder Contact Analysis: (a) Contact Schematic, (b) Ellipse Fitting from Computational Results

between θ and ϕ). This situation is shown schematically in Figure 9.3(a), in which both the angles are defined. Part (b) of the figure shows a calculation for the best-fit ellipse as well as an error estimate for the curve fit. The open circles correspond to grid points immediately inside the contact region (for which the contact pressure $p_{ij} > 0$), while the closed circles correspond to grid points immediately outside the contact. The ellipse fitting error is defined as:

$$E_e = \frac{1}{Nb} \sum_{i=1}^N \sqrt{(x_i - \bar{x}_i)^2 + (y_i - \bar{y}_i)^2} \quad (9.5)$$

where $(x_i; y_i)$ are the coordinates of the grid points defined on the figure, N is the total number of points defining the contact boundary, and (\bar{x}_i, \bar{y}_i) are the

coordinates on the best-fit ellipse closest to the grid point $(x_i; y_i)$. The error is therefore interpreted as the mean distance of each grid point to the best-fit ellipse, normalized by the semi-minor axis b .

These results use $l_e = 0.225$ mm, and we first present a calculation for contact size in the absence of friction and $\phi = 90^\circ$, for which there exists an analytical solution [Young 1989, page 651]. In this case, $\theta = 90^\circ$, and the analytical solution for the ellipse axes is $a_a = 2.287$ mm and $b_a = 1.748$ mm. Our calculations for the best-fit ellipse result in $a_e = 2.303$ mm, $b_e = 1.781$ mm, $\theta = 89.5^\circ$, with ellipse fitting error $E_e = 0.05$. The average error in the estimates for $(a_e; b_e)$ is about 1.25% as compared to the analytical solution $(a_a; b_a)$. This calculation gives confidence that the numerical algorithm for contact calculations is correct, that the predicted ellipse axes are correct, and also that the background grid is sufficiently fine that the best-fit ellipse accurately represents the actual contact region. A number of other cases, both with friction and without, are shown in Figure 9.4 for $\phi = 30^\circ$; 45° ; 60° ; 90° . For the non-zero friction cases, the stick ellipse in the center of contact was fit with an ellipse in the same way as the contact zone. We note the increasing stick zone size with increasing friction, as expected, although the total contact size changes by only a few percent as in the Hertz problem discussed above. For $\mu = 0.5$, virtually the entire contact sticks; fully resolving this very small slip ellipse will require an extremely dense background grid. Angle θ always lags the cylinder orientation angle ϕ , and the ellipse aspect ratio a/b

becomes smaller as ϕ increases. In all cases, the error in the ellipse fit is on the order of 11% or less. Error is larger for the larger aspect ratio cases, for which resolving the semi-minor axis b demands a finer mesh. From this crossed cylinder example, we reinforce the idea that the approach described here is capable of accurately and efficiently solving non-conformal normal contact problems with friction.

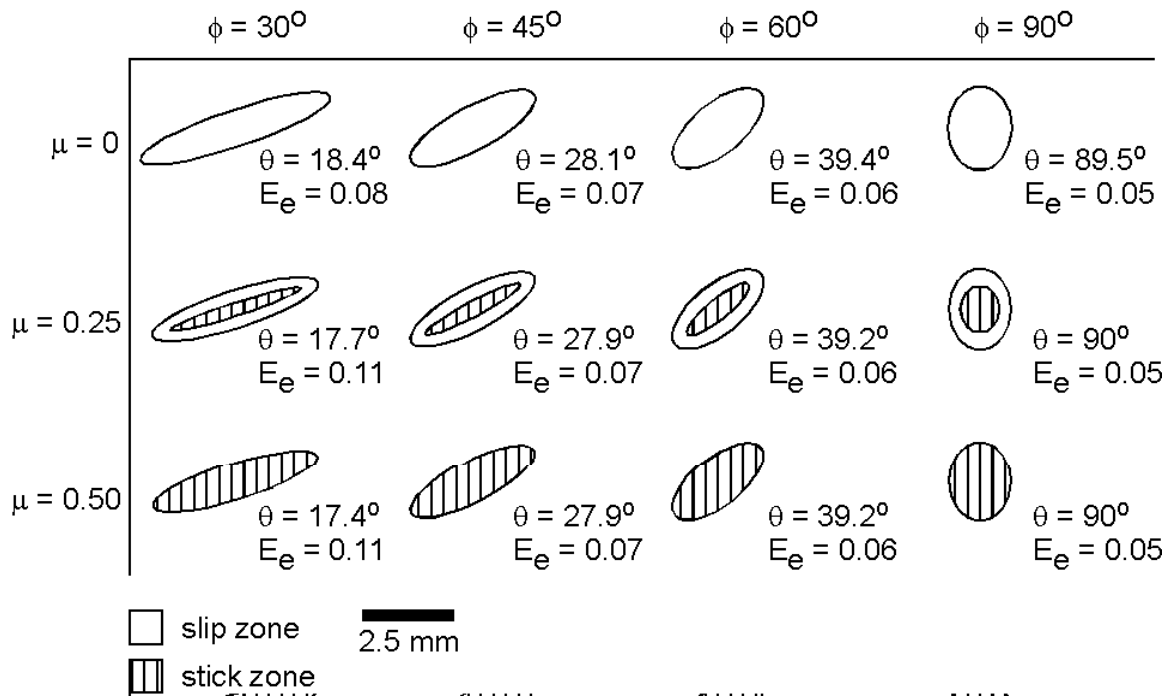


Figure 9.4 Crossed Cylinder Contact Results for Contact and Stick Zone Size with $\mu = 0; 0.25; 0.5$ and $\phi = 30^\circ; 45^\circ; 60^\circ; 90^\circ$. E_e is the Curve Fit Error from Equation (9.5)

Chapter 10

Discussion and Conclusion

The numerical solutions described here demonstrate the fidelity of this semi-analytical method for a variety of normal contact problems. Specifically, comparisons to analytical solutions (Hertz, Spence, Roark) and existing numerical results (Guyot, Kosior) are very good. The semi-analytical nature of this approach affords several convenient features for the numerical implementation:

- Boundary conditions for the contact mechanics problem are contained in the analytical solutions, so the size of the physical domain over which the background mesh is defined must be only slightly larger than the actual contact area, and the background grid is defined only on the contact surfaces
- Iteration on contact area and stick/slip boundary location uses the analytical displacement solutions, which reduces the computational cost of each iteration

- Displacement interpolation errors are eliminated by using the analytical solution for surface displacements
- Non-Hertzian contact configurations, including those with friction and non-quadratic surfaces, can be analyzed easily, so long as the underlying assumptions of the analytical displacement solution (i.e., we can consider the surfaces as elastic half-spaces) are not violated

As compared to the FEM and BEM approaches to contact mechanics, this method provides some advantages, the most important being its lack of interpolation of field variables. In this approach, the displacement at each node is related to loading at every other node through a non-zero influence function which is determined analytically. This allows us to describe the contact surface without formal elements or structured connectivity, because each node is implicitly connected to every other node. On the other hand, the resulting discrete equations do not retain the characteristic banded structure of FEM stiffness matrices, and in this sense our approach is similar to the BEM approach, in which fully-populated matrices result. Nonetheless, the numerical results presented here clearly show that the accuracy of this method is consistent with, and in some cases better than, more traditional numerical approaches.

The lack of underlying 'element' organization of the overlapping pyramid loading cells may suggest that this approach falls into the broad class of 'mesh

less' methods. However, this is not strictly the case, as this method makes no use of interpolation functions for the field variables (displacements), and instead uses the analytical surface displacement solutions developed elsewhere [Li & Berger 2001]. On the other hand, mesh less methods depend upon well-defined interpolation functions, regardless of the mesh less approach used (e.g., moving least squares [Lancaster & Salkauskas 1981], partition of unity [Babuska & Melenk 1997], hp-clouds [Duarte & Oden 1996], mesh less local Petrov-Galerkin [Atluri, Kim & Cho 1999], etc.). System stiffness matrices in mesh less approaches require numerical integration of the interpolation functions, and depending upon the interpolation scheme and mesh less approach, this sometimes requires use of background "integration cells" to facilitate quadrature. On the contrary, this approach circumvents all of these interpolation concerns by directly developing the influence coefficients from analytical surface displacement solutions.

We next consider the relationship between this work and the suggestions of Johnson [Johnson, 1985], who originally proposed this type of procedure. Johnson considered normal contact of frictionless surfaces for both line and point contacts. To describe the influence coefficients he used a variety of analytical solutions, depending upon the location of the point of interest relative to the loading point, and in fact his expressions for influence coefficients are exact for only a few nodes on the contact surfaces. By constructing the influence

coefficients from piecewise analytical solutions and approximations, he makes use of readily-available expressions.

This method is a substantial extension over Johnson's original work, although the procedure and underlying framework retain the same spirit. Here, we solve 3-D normal contact normal contact with friction 3-D problems with friction, and this non-trivial extension has been achieved after first developing the fundamental analytical surface displacement solutions for triangular (normal and tangential) loading profiles [Li & Berger 2001]. From these analytical solutions, the influence coefficients can be derived, the governing contact equations assembled, and the resulting system solved at each iteration step to determine contact area and stick zone size. The influence coefficients can be evaluated exactly at every point on the contact surface, although the computational price is the resulting fully-populated coefficient matrices.

A semi-analytical approach to general non-Hertzian normal contact mechanics problems has been described and validated against analytical solutions and previous numerical results for normal contact of dissimilar materials, with friction. This approach is fundamentally different from more traditional numerical approaches, and the key distinction is the lack of an underlying interpolation scheme for the field variables. Instead, we use an analytical solution for surface displacements due to a pyramid loading profile, and then the

total normal and tangential contact tractions can be assembled as a superposition of appropriately-scaled, overlapping pyramid sections. This approach employs iteration on contact size and stick zone to reach a convergent solution. The numerical results show high accuracy as compared to previous numerical and analytical solution. The sensitivity of the method allows us to capture changes in contact area due to friction, an observation supported elsewhere in the literature.

Having validated the numerical framework for normal contact problems with friction, the work was reported in [Li, J. and Berger, E. J., 2003].

Part IV

The Development of a Semi-Analytical Approach to 3-D Frictional Contact Problem with Tangential Load --- Incremental Algorithm

As discussed in section 2.2.2, due to the path-dependent nature of frictional force, in principle, any contact problems with friction involved should be treated as dynamic models. The work done also shows difficulty when using non-incremental algorithm to the cases that global tangential force exist, although the non-incremental algorithm seems to have the capacity to consider tangential force (see section 8.4). Therefore, in order to handle general 3-D contact problems, it is necessary to develop incremental algorithm. This part presents the development of such an algorithm, which is based also on the idea of overlapped pyramids.

Chapter 11

Modeling of Frictional Contact

We first discuss several useful contact models, then present related contact conditions. The contact model employed by the author is derived from these models.

11.1 Elastodynamic Model

For the purpose of simplification, we consider that a linear elastic body, occupying a space $\Omega \in R^N$ (for 3-D problem, $N=3$), comes into contact with a rigid foundation, over part Γ_c of its boundary Γ . The body force density is $\vec{b} = (b_1, b_2, \dots, b_N)$, and prescribed displacements \vec{U}_d are applied to boundary Γ_d , and traction t onto the parts Γ_t . We also assume that: $\Gamma = \Gamma_c \cup \Gamma_d \cup \Gamma_t$. Γ_c is called contact boundary, which means the boundary of Ω that possibly comes into contact (Figure 11.1).

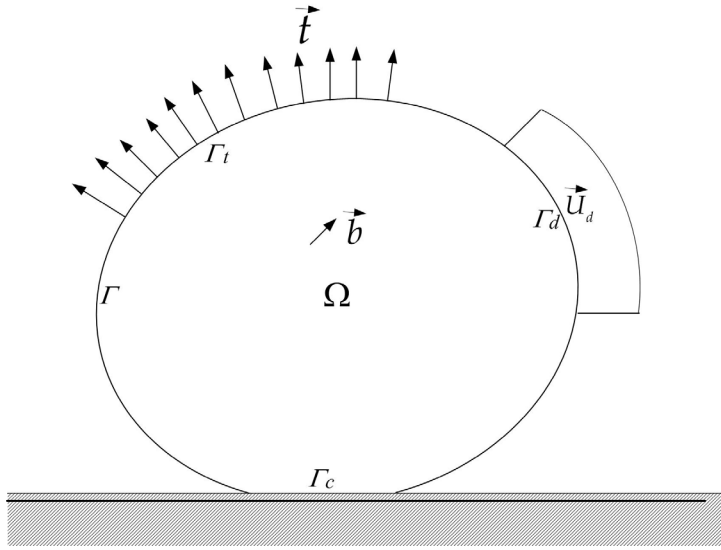


Figure 11.1 The Elastodynamic Model

Assume the material of elastic body possesses isotropic properties. The elastodynamic model presented here is based on the Oden and Martins' model [Oden and Martins, 1985], except the modification that the spring constraint has been taken away. It is reasonable since we do not consider the significant motion of contact bodies. From elasticity, we have:

$$\sigma_{ij}(\vec{u}) = E_{ijkl} \vec{u}_{k,l} \quad (11.1)$$

where σ_{ij} is the stress tensor, $\vec{u}_{k,l} = \partial \vec{u}_k / \partial x_l$, $1 \leq i, j, k, l \leq N$ is the derivative of displacements, and E_{ijkl} is the elasticities, which satisfy:

$$E_{ijkl} = E_{jikl} = E_{ijlk} = E_{klij}, \quad E_{ijkl} \in L^\infty(\Omega), \quad (11.2)$$

In Ω , for every symmetric tensor A_{ij} , α is a positive constant in following inequality:

$$E_{ijkl} A_{kl} A_{ij} \geq \alpha A_{ij} A_{ij} \quad (11.3)$$

And the elasticities also satisfy:

$$\sup_{1 \leq i, j, k, l \leq N} \|E_{ijkl}\|_{\infty} \leq M. \quad (11.4)$$

For a time interval $[0, T]$, the equations governing this elastodynamics problem are written as follows:

$$\sigma_{ij}(\bar{u})_{,j} + b_i = \rho \ddot{u}_i, \text{ in } \Omega \text{ and } (0, T), \quad (11.5)$$

where, ρ is mass density, and $\partial\rho/\partial t = 0$, $\rho \in L^{\infty}(\Omega)$, $\rho \geq \rho_0 > 0$; the particle acceleration is:

$$\ddot{u}_i \equiv \partial^2 u_i / \partial t^2 \quad (11.6)$$

stress and displacement relations are written as:

$$\sigma_{ij}(\bar{u}) = E_{ijkl} \bar{u}_{k,l} \quad (\sigma_{ij} = \sigma_{ji}). \quad (11.7)$$

The boundary conditions are:

$$\bar{u} = \bar{u}_d \quad \text{on } \Gamma_d, t \in [0, T], \quad (11.8)$$

$$\sigma_{ij}(\bar{u})n_j = t_i \quad \text{on } \Gamma_t, t \in [0, T], \quad (11.9)$$

Initial conditions:

$$\bar{u} = \bar{u}_0, \quad \dot{\bar{u}} = \bar{u}_1 \quad \text{in } \Omega \text{ and } t=0. \quad (11.10)$$

11.2 Quasi-Static Model

The quasi-static model is obtained from dynamic model by neglecting the inertial force term. The quasi-static problem is to find the fields of displacement and stress tensor such that:

$$\operatorname{div} \bar{\sigma} + \bar{b} = 0 \quad \text{in } \Omega, 0 < t < T, \quad (11.11)$$

$$\sigma_{ij}(\bar{u}) = E_{ijkl} \bar{u}_{k,l} \quad (\sigma_{ij} = \sigma_{ji}) \quad \text{in } \Omega, 0 < t < T, \quad (11.12)$$

$$\bar{\sigma} \cdot \bar{n} = \bar{t} \quad \text{on } \Gamma_t, 0 < t < T \quad (11.13a)$$

$$\bar{u} = \bar{u}_d \quad \text{on } \Gamma_d, 0 < t < T, \quad (11.13b)$$

$$\bar{u} = \bar{u}_0, \quad \text{in } \Omega \text{ and } t=0. \quad (11.14)$$

The model covers two frequently used boundary conditions:

- The resultant forces exerted on the body on contact boundary are given;
- The displacement fields on the contact boundary are given.

11.3 Contact Conditions on Contact Boundary

We consider a special case: both the elastic body and the rigid foundation have flat surfaces and are infinite half spaces. Denote by g the initial gap, or separation between the contact boundary and rigid foundation, measured along the outward normal direction of Γ_c (Figure 11.2).

There are two different ways to model contact boundary conditions: Signorini's condition and Oden's power law model. The latter provide certain insight of frictional contact phenomenon. The basic ideas for both models are cited in the following two sections.

11.3.1 Signorini's Contact Condition

Figure 11.2 (a) and (b) show the status before and after an elastic body comes into contact with a rigid foundation. The contact boundary is treated as an ideal surface, the property of which is described only by the coefficient of friction μ .

Because the elastic body cannot penetrate the rigid foundation, we have:

$$u_N - g \leq 0 \quad \text{on } \Gamma_c \quad (11.15)$$

where, u_N is the normal surface displacement of elastic body, g is the initial gap before contact. Notice that contact stresses are compressive, therefore:

$$\sigma_N \leq 0 \quad \text{on } \Gamma_c \quad (11.16)$$

On contact boundary Γ_c , the following relation holds:

$\sigma_N(u_N - g) = 0$, which means:

$$\begin{cases} \text{contact} : & u_N - g = 0 \\ \text{separation} : & \sigma_N = 0 \end{cases} \quad (11.17)$$

The above three equations represent Signorini's contact condition on Γ_c . Let

$\dot{u} = \partial \bar{u} / \partial t$ denote the derivative of displacement with respect to time, then the

Coulomb's law of friction is written as:

$$\begin{cases} |\bar{\sigma}_T| < -\mu \sigma_N & \text{then } \dot{u}_T = 0 \\ |\bar{\sigma}_T| = -\mu \sigma_N & \text{then } \dot{u}_T = -\lambda \bar{\sigma}_T \text{ for some } \lambda \geq 0 \end{cases} \quad (11.18)$$

11.3.2 Oden's power law of friction

In reality, however, the surface is not perfect. The surface properties greatly depend on the machining processes and working environments. Figure 11.2 (c) and (d) show the status before and after an elastic body comes into contact with a rigid foundation. On summarizing experimental work, Oden and his colleagues proposed a non-linear, non-local law of friction [Oden and Martins, 1985], which can better address the real behavior of contact surfaces than classic Coulomb's law of friction. The normal compliance is written as power law:

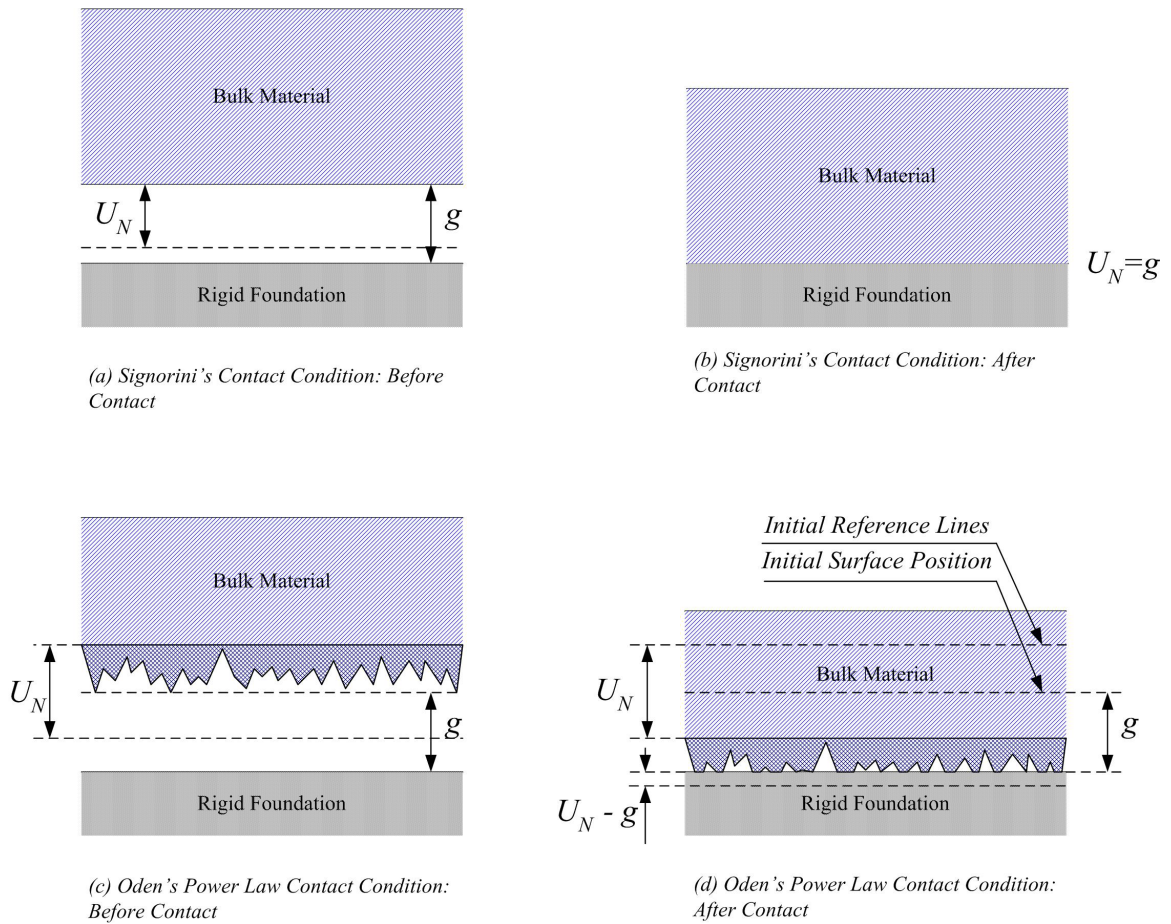


Figure 11.2 The Contact Problem of Two Infinite Half Spaces (See similar discussion in [Oden and Martins, 1985] and [Klarbring, Mikelic and Shillor, 1988])

$$-\sigma_N = c_N (U_N - g)_+^{m_N} \quad (11.19)$$

where the constants $c_N > 0$, $m_N > 0$ are all related to the physical characteristics of the surface. The friction law is then generalized into the form:

$$\begin{cases} |\bar{\sigma}_T| < c_T (u_N - g)_+^{m_T} & \text{then } \dot{u}_T = 0 \\ |\bar{\sigma}_T| = c_T (u_N - g)_+^{m_T} & \text{then } \dot{u}_T = -\lambda \bar{\sigma}_T \text{ for some } \lambda \geq 0 \end{cases} \quad (11.20)$$

The classic Coulomb's law of friction can be retrieved by setting $c_T = \mu c_N$, and $m_T = m_N$.

11.4 Incremental Model

As discussed in section 2.2.2, the widely adopted way to deal with quasi-static problem is incremental method. This section is to derive the incremental model by using Oden's power law of friction. Divided time interval $[0, T]$ into $N+1$ segments (t_n, t_{n+1}) , $n = 0, 1, 2, \dots, N$ and $0 = t_0 < t_1 < \dots < t_{N+1} = T$.

Let the time derivative of displacements \bar{u} be approximated by finite difference:

$$\dot{\bar{u}}(t_{n+1}) \approx (\bar{u}(t_{n+1}) - \bar{u}(t_n)) / (t_{n+1} - t_n) \quad (11.21)$$

Introduce following notation to simplify the formula:

$$\bar{u}^n = \bar{u}(t_n) \quad (11.22)$$

Then we can write:

$$\bar{u}^{n+1} = \bar{u}^n + \Delta\bar{u}^n, \quad \bar{t}^{n+1} = \bar{t}^n + \Delta\bar{t}^n, \quad \bar{b}^{n+1} = \bar{b}^n + \Delta\bar{b}^n \quad (11.23)$$

here, Δ denotes the increment at current load step. We further write \bar{u}^n as the sum of incremental solutions:

$$\bar{u}^n = \bar{u}^0 + \sum_{i=0}^{n-1} \Delta u^i \quad (11.24)$$

where \bar{u}^0 is initial displacement.

Oden et al. [Oden and Martins, 1985] and Klarbring et al. [Klarbring, Mikelic and Shillor, 1988] derived the incremental formula by using the method of virtual power of normal stress and frictional force. Their work shows that the incremental problem is equivalent to the following time independent boundary value problem:

$$\operatorname{div} \bar{\sigma}(\Delta\bar{u}^n) + \Delta\bar{b}^n = 0 \quad \text{in } \Omega \quad (11.25)$$

$$\Delta u^n = 0 \quad \text{on } \Gamma_d \quad (11.26)$$

$$\bar{\sigma}(\Delta\bar{u}^n) \cdot \bar{n} = \Delta\bar{t} \quad \text{on } \Gamma_t \quad (11.27)$$

$$\bar{\sigma}_N = -c_N (u_N^n + \Delta u_N^n - g)_+^{m_T} \quad \text{on } \Gamma_c \quad (11.28)$$

$$\left\{ \begin{array}{l}
 |\bar{\sigma}_T(\bar{u}^n + \Delta\bar{u}^n)| < c_T(u_N^n + \Delta u_N^n - g)_+^{m_T} \quad \text{then } \Delta\bar{u}_T^n = 0 \\
 |\bar{\sigma}_T(\bar{u}^n + \Delta\bar{u}^n)| = c_T(u_N^n + \Delta u_N^n - g)_+^{m_T} \\
 \quad \text{then } \Delta\bar{u}_T^n = -\lambda \bar{\sigma}_T(\bar{u}^n + \Delta\bar{u}^n) \text{ for some } \lambda \geq 0
 \end{array} \right. \quad (11.29)$$

Chapter 12

The Incremental Algorithm for Contact Boundary

Problems

The model presented in section 11.4 is a complete model to describe the behavior of the elastic body under the various applied forces (or tractions) / displacements, as well as body force. Now we simplify this model to concentrate on contact behavior, in other words, only contact area, surface tractions, surface displacements, and partition of stick and slip zone of contact boundary Γ_c are to be found. We use Signorini's law in order to further simplify the model, which means the properties of real surfaces are modeled into only one parameter: coefficient of friction. Because this simplified model can be retrieved from the power law model, the existence and uniqueness issue are covered by the power law model. Pre-developed traction-displacement relationships are used to formulate the solution.

12.1 The Derivation of Contact Model for Two Elastic Bodies

Model One: A flat elastic body rests on a flat rigid foundation.

Since we consider both bodies as infinite half spaces, the contact condition will be the same everywhere, only one single point represents the solution to all the body. The model can be written as follows:

At loading step $n+1$ ($n = 0, 1, 2, \dots, N$):

Lose contact: $\sigma_N = \sigma_T = 0$

Come into contact: $\sigma_N < 0$ and:

$$\sigma_N(\bar{u}^n + \Delta\bar{u}^n) < 0 \Rightarrow \left\{ \begin{array}{l} \text{Sticking Zone :} \\ \left| \bar{\sigma}_T(\bar{u}^n + \Delta\bar{u}^n) \right| < -\mu\sigma_N(\bar{u}^n + \Delta\bar{u}^n) \\ \Rightarrow \Delta\bar{u}^n = 0 \\ \\ \text{Slipping Zone :} \\ \left| \bar{\sigma}_T(\bar{u}^n + \Delta\bar{u}^n) \right| = -\mu\sigma_N(\bar{u}^n + \Delta\bar{u}^n) \\ \Rightarrow \exists \lambda \geq 0, \Delta\bar{u}^n = \lambda\bar{\sigma}_T(\bar{u}^n + \Delta\bar{u}^n) \end{array} \right. \quad (12.1)$$

The above equation and inequality serves as criteria that a surface point fall into stick or slip zone, or a node changes contact conditions.

Model Two: The Curved Elastic Body to Flat Rigid Foundation

Since the elastic body is curved in contact boundary, the contact conditions are different from point to point. However, we can use the flat-flat model in a point-wise manner, taking into account the fact that the initial gap is different from

point to point, not all of points fall into contact or separate. Therefore, an algorithm needs to be developed to determine which nodes are falling into contact and which are not.

Model Three: The Curved Elastic Body to Curved Elastic Body

Finally, we will reach our goal: the contact problem of two non-conforming elastic bodies. Note that in this case: (1) Both bodies are elastic, therefore any points within two bodies have displacements. (2) Both bodies are curved, therefore, the initial gap should take into account the two parts. This can be formulated by modifying some constants from model No. 2.

12.2 Algorithms for Contact Area Detecting, Stick/Slip Zone Partitioning, and Field Variables Computation

Let $h(X, Y, t)$ denote the initial gap between the body and foundation when they come into contact but contact stress is zero. Follow the detailed procedure discussed in [Li and Berger, 2002, or Part III of the dissertation], we can write:

For all the surface nodes on contact boundary, the following relation holds (See Figure 8.2):

$$\lambda_1 \sum_k \sum_m \hat{C}_{ijkm} P_{km} + \lambda_2 \sum_k \sum_m \hat{F}_{ijkm} q_{km,X} + \lambda_2 \sum_k \sum_m \hat{I}_{ijkm} q_{km,Y} \quad (12.2)$$

$$\begin{cases} = -h(X, Y, t) & \text{within contact area } S \\ > -h(X, Y, t) & \text{outside contact area } S \\ < -h(X, Y, t) & \text{outside contact area } S, \text{ penetration takes place} \end{cases}$$

where

$$\lambda_1 = \frac{1-\nu_1}{2\pi G_1} + \frac{1-\nu_2}{2\pi G_2} \quad (12.3)$$

$$\lambda_2 = \frac{1-2\nu_1}{4\pi G_1} - \frac{1-2\nu_2}{4\pi G_2} \quad (12.4)$$

Keep in mind that P_{km} , $q_{km,X}$ and $q_{km,Y}$ are functions of time, and \vec{C}_{ijkm} , etc., are the constants with respect to time. By taking derivative of equation (12.2) with respect to time (t), and approximating derivatives by finite differences, we have:

$$\lambda_1 \sum_k \sum_m \hat{C}_{ijkm} \Delta P_{km}^n + \lambda_2 \sum_k \sum_m \hat{F}_{ijkm} \Delta q_{km,X}^n + \lambda_2 \sum_k \sum_m \hat{I}_{ijkm} \Delta q_{km,Y}^n = -\Delta h^n \quad (12.5)$$

where, the symbol Δ denotes the increment, superscript n denotes the loading step, they keep the same meanings for following derivation.

Equilibrium in the Z-direction also requires the force balance constraint:

$$A_p \sum_k \sum_m P_{km} = P_{total} \quad (12.6)$$

where $A_p = \frac{\sqrt{3}}{2} l_e^2$ is the characteristic volume of a pyramid of uniform hexagonal base and unit height, and P_{total} is the total normal load applied to the contacting bodies.

We take derivative of equation (12.3) with respect to time (t) , and approximate derivatives by finite differences:

$$A_p \sum_k \sum_m \Delta P_{km}^n = \Delta P_{total}^n \quad (12.7)$$

In sticking regions, the points A_1 and A_2 remain coincident (See Figure 8.3), $\Delta_{1,X} - \Delta_{1,X} = 0$; recognizing that the displacements can be written relative to displacements at the origin $\bar{U}_{1,X}(0,0)$ and $\bar{U}_{2,X}(0,0)$, we write:

$$\underline{X-direction}: \lambda_3 \sum_k \sum_m \hat{D}_{ijkm} P_{km} - \lambda_4 \sum_k \sum_m \hat{G}_{ijkm} q_{km,X} - \lambda_5 \sum_k \sum_m \hat{J}_{ijkm} q_{km,Y} = 0 \quad (12.8)$$

$$\underline{Y-direction}: \lambda_3 \sum_k \sum_m \hat{E}_{ijkm} P_{km} - \lambda_5 \sum_k \sum_m \hat{H}_{ijkm} q_{km,X} - \lambda_4 \sum_k \sum_m \hat{K}_{ijkm} q_{km,Y} = 0 \quad (12.9)$$

where

$$\lambda_3 = \frac{1-2\nu_1}{4\pi G_1} - \frac{1-2\nu_2}{4\pi G_2} \quad (12.10)$$

$$\lambda_4 = \frac{1-\nu_1}{2\pi G_1} + \frac{1-\nu_2}{2\pi G_2} \quad (12.11)$$

$$\lambda_5 = \frac{\nu_1}{2\pi G_1} + \frac{\nu_2}{2\pi G_2} \quad (12.12)$$

Again we obtain finite difference equations from (12.6)~(12.7):

X – direction :

$$\lambda_3 \sum_k \sum_m \hat{D}_{ijkm} \Delta P_{km}^n - \lambda_4 \sum_k \sum_m \hat{G}_{ijkm} \Delta q_{km,X}^n - \lambda_5 \sum_k \sum_m \hat{J}_{ijkm} \Delta q_{km,Y}^n = 0 \quad (12.13)$$

Y – direction :

$$\lambda_3 \sum_k \sum_m \hat{E}_{ijkm} \Delta P_{km}^n - \lambda_5 \sum_k \sum_m \hat{H}_{ijkm} \Delta q_{km,X}^n - \lambda_4 \sum_k \sum_m \hat{K}_{ijkm} \Delta q_{km,Y}^n = 0 \quad (12.14)$$

In slip region, the surface tractions fulfill Coulomb's law. In general, we write:

$$|\vec{q}_{km}^n| = u P_{km}^n, \quad \exists \lambda \geq 0, \quad \Delta \vec{u}_T^n = \lambda \vec{q}_{km}^n, \quad (12.15)$$

and

$$|\vec{q}_{km}^n| = \sqrt{q_{km,X}^2 + q_{km,Y}^2} \quad (12.16)$$

Because (12.16) is a non-linear equation of q_X and q_Y , we cannot integrate equations (12.15-12.16) into system equations. We introduce the concept of vector of coefficient of friction to linearize the equation:

$$\bar{\mu} = \begin{Bmatrix} \mu_X \\ \mu_Y \end{Bmatrix} \quad (12.17)$$

The component of $\bar{\mu}$ can be written as:

$$\mu_X(X, Y, t) = \left| \frac{q_X}{q} \right| \mu \quad (12.18a)$$

$$\mu_Y(X, Y, t) = \left| \frac{q_Y}{q} \right| \mu \quad (12.18b)$$

where $q = |\vec{q}|$ is the resultant tangential traction magnitude. The resultant friction coefficient has the constant magnitude:

$$\mu = \sqrt{\mu_X^2 + \mu_Y^2} \quad (12.19)$$

Since q_X and q_Y in current load step are the unknowns in system equations, we cannot use above relations to obtain μ_x and μ_y directly. We then use the result from previous iterative step to compute μ_x and μ_y in current step. That is:

$$\mu_X^n(i) = \left| \frac{q_X^n(i-1)}{q_0^n(i-1)} \right| \mu_o \quad (12.20a)$$

$$\mu_Y^n(i) = \left| \frac{q_Y^n(i-1)}{q_0^n(i-1)} \right| \mu_o \quad (12.20a)$$

where i is the index of iteration. In the beginning of iteration scheme, vector $\bar{\mu}$ is set in the direction of radius. Note that the components of $\bar{\mu}$ are always positive.

In practice, therefore, the equation (12.15-12.16) are rewritten as:

$$q_{km,X}^n = \mu_X^n P_{km}^n \text{sign}(\Delta u_{TX}^n) \quad (12.21)$$

$$q_{km,Y}^n = \mu_Y^n P_{km}^n \text{sign}(\Delta u_{TY}^n) \quad (12.22)$$

$$\Delta \bar{u}_T^n = \Delta u_{TX}^n \bar{i}_X + \Delta u_{TY}^n \bar{j}_Y \quad (12.23)$$

where, \bar{i}_X and \bar{j}_Y are unit vector in X- and Y- direction respectively. Δu_{TX}^n and Δu_{TY}^n are X- and Y- component of $\Delta \bar{u}_T^n$ respectively. Because $\Delta \bar{u}_T^n$ is unknown, in the iteration, we use the result of previous computational step instead:

$$\Delta u_{TX}^n(i) \approx \Delta \bar{u}_T^n(i-1) \bullet \bar{i}_X \quad (12.24)$$

$$\Delta u_{TY}^n(i) \approx \Delta \bar{u}_T^n(i-1) \bullet \bar{j}_Y \quad (12.25)$$

where, the letter i represents the number of iterative step. The convergent iteration will ensure the final results are current for this loading step.

Finally, the overall tangential force balance of the system requires:

$$A_p \sum_k \sum_m \Delta q_{km,X}^n = \Delta Q_X^n \quad (12.26)$$

$$A_p \sum_k \sum_m \Delta q_{km,Y}^n = \Delta Q_Y^n \quad (12.27)$$

12.3 Discrete Equations and Numerical Approach

For each load step, the system equations are similar to non-incremental algorithm. They are assembled and solved in the same way as discussed in section 8.5. Only the meanings of unknowns are different: all the unknowns represent the value of increments.

Figure 12.1 presents a general flowchart that outlines that numerical procedure. Due to the nature of contact problems, the procedures such as contact detecting, stick/slip zone partitioning, determining of the direction of shear traction, etc., require iterations. There are two important iterative procedures in this numerical approach, which are presented in detail next.

12.3.1 Iteration on Expanding Contact Area

In a non-incremental algorithm, the contact area keeps shrinking from initial pre-described large area until final convergence. The incremental algorithm, however, is a two-way road; it can expand or shrink contact and stick zone whenever it is necessary. For example, when a normal load starts from zero to its maximal value monotonically, the contact zone should expand monotonically.

Expanding becomes necessary when the contact area in current step is too small. The expanding is implemented in such a way that it enlarges the current contact

area by a ring. In Figure 12.2, the solid dots represent current contact area, while the hollow dots show the expanded area. This approach has an advantage of “following the current shape of contact area”. Sometimes it will save computational time if contact area expands more than one ring at a time, this is realized simply by repeating above procedure.

We use equation (12.2) as a criterion to judge whether a contact area is too small. When the contact area is too small for the loads, the equation takes minus sign somewhere outside contact area, which means penetration has taken place. The contact zone, therefore, needs to be expanded.

The penetration is checked after the current step field variables have been computed, because penetration checking is based on current value, rather than increments.

12.3.2 Iteration on Shrinking Contact Area

Shrinking contact area is discussed in section 8.6 (under A: Iteration on contact area). The procedure is still used in the incremental algorithm. All the nodes falling into contact area must fulfill:

$$p_{ij}^n = p_{ij}^{n-1} + \Delta p_{ij}^n \geq 0 \quad \forall (i, j) \in S \quad (12.28)$$

After system equations are solved, each node in current contact zone is examined against the above criteria. If any node has $p_{ij}^n < 0$, then this node is eliminated from contact zone.

12.3.3 Iteration on Partitioning Stick / Slip Zone

The partitioning of stick/slip zone is based upon the Coulomb's law used in point-wise manner. For all the nodes in stick:

$$|\vec{q}(X_i, Y_j)| < \mu_0 p(X_i, Y_j) \quad (12.29)$$

For all the nodes in slip, we have:

$$|\vec{q}(X_i, Y_j)| = \mu_0 p(X_i, Y_j) \quad (12.30)$$

It happens all the time in the loading procedure when stick and slip nodes interchange. The following criteria guide the change of status:

(i) If a node in stick in current step has the shear traction that:

$$|\vec{q}(X_i, Y_j)| \geq \mu_0 p(X_i, Y_j) \quad (12.31)$$

then it becomes slip node in next step.

(ii) If a node in slip in current step has zero slip velocity:

$$\Delta \vec{u}_T^n = \vec{0} \quad (12.32)$$

then this node becomes stick in next step.

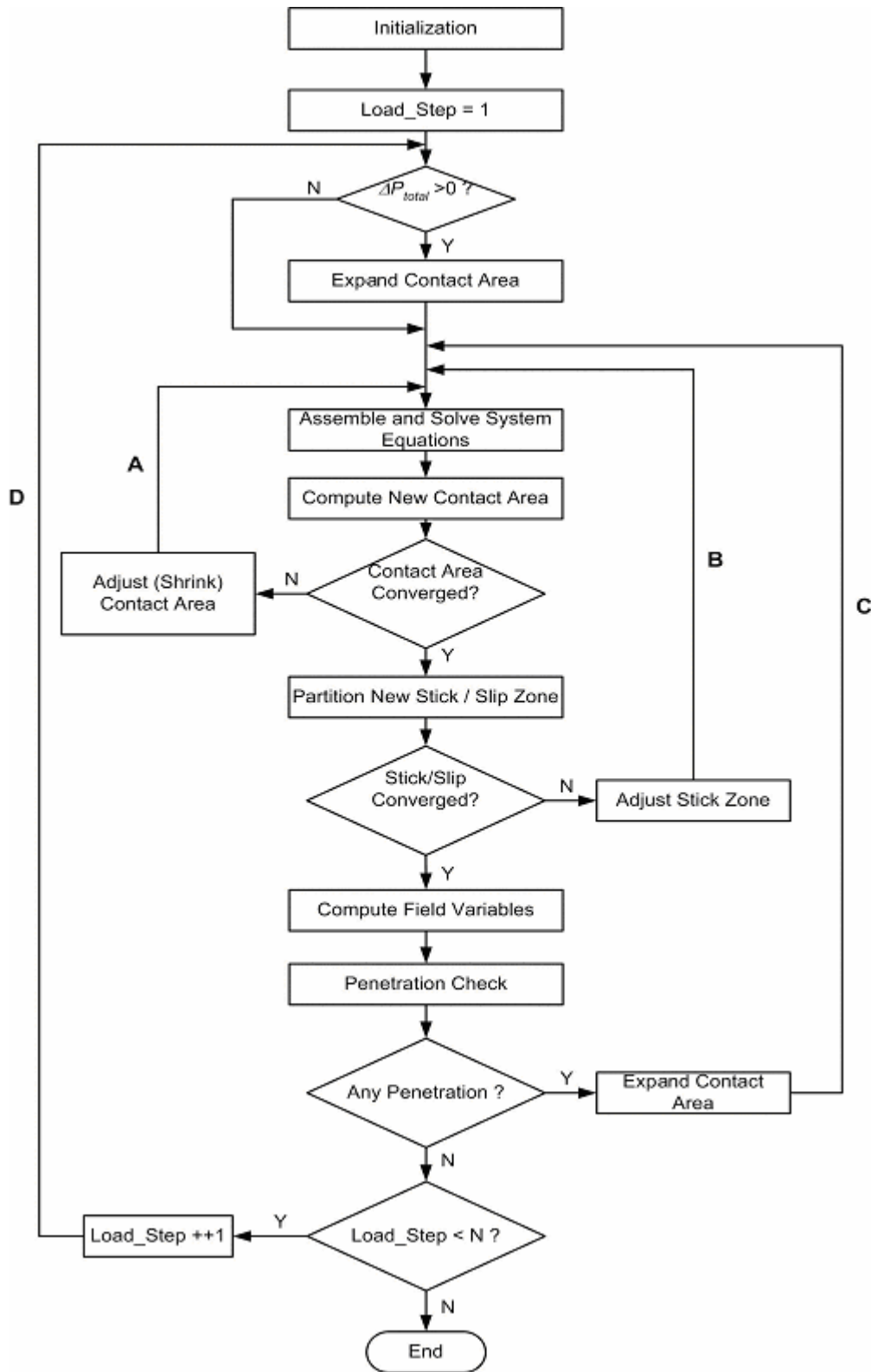


Figure 12.1 The Flowchart of Numerical Framework

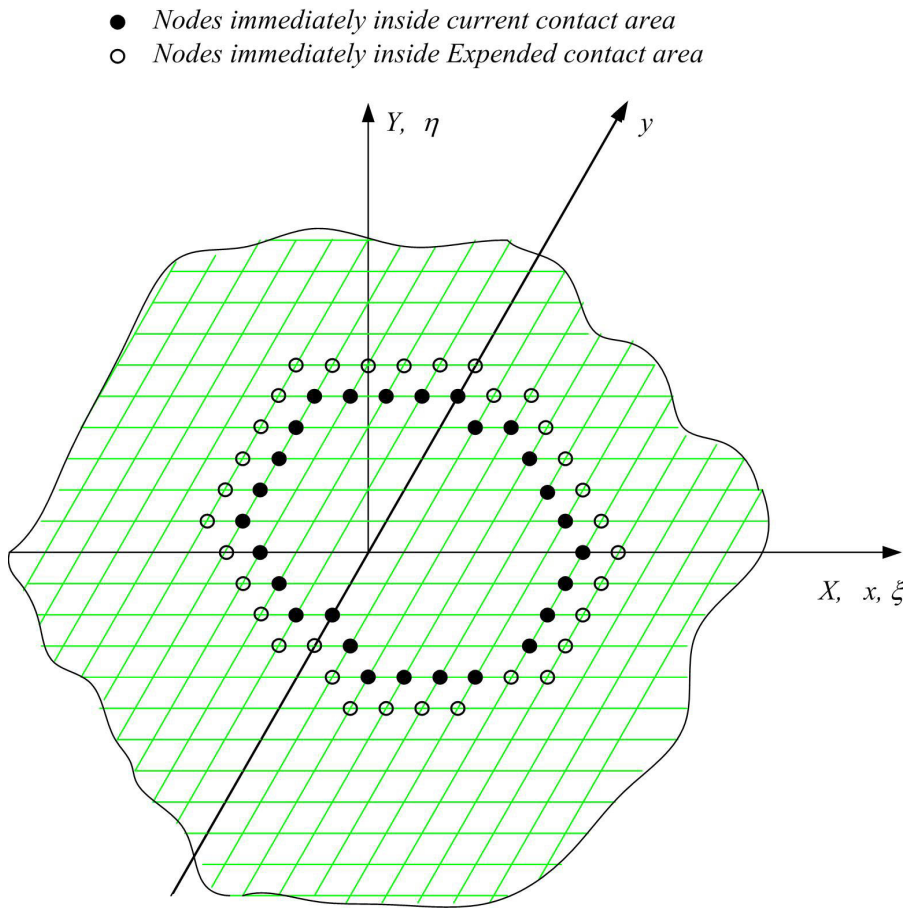


Figure 12.2 The Expanding of Contact Area

Chapter 13

Numerical Examples

The incremental algorithm has been implemented into a numerical framework, which has been used to examine several contact problems. These problems are used to validate the algorithm and show the capacities of the algorithm. This algorithm is primarily developed to accommodate the need of general 3-D contact problem with friction and tangential force(s). One of major application of such a contact model is fretting contact problems. The fretting contact problems are usually divided into two categories: similar material problems and dissimilar material problems, due to the fact that they have totally different behaviors. We refer material similarity to the elastic properties of materials of contacting bodies. Dundur's parameter is introduced to measure the similarity of material:

$$\beta = \frac{\frac{1-2\nu_1}{G_1} - \frac{1-2\nu_2}{G_2}}{\frac{1-\nu_1}{G_1} + \frac{1-\nu_2}{G_2}} \quad (13.1)$$

For the same material, $\beta=0$.

13.1 Contact Problem with Similar Materials

First, we consider the contact problem with similar materials ($\beta \approx 0$), we can see from equation (12.2), (12.8)~(12.9), the normal traction and tangential tractions are decoupled. It means that tangential tractions will not affect normal traction in entire contact area; the tangential traction in stick zone can be independently computed while tangential tractions in slip zone can be obtained by Coulomb's law and slip velocity.

Furthermore, if Poisson's ratio is zero, the tangential tractions in X- and Y-directions are decoupled also.

13.1.1 Cattaneo-Mindlin's Solution

This problem was first studied by Cattaneo [Cattaneo, 1938], and later on, by Mindlin [Mindlin, 1949], [Mindlin and Deresiewicz, 1953] independently. They provided an analytical solution that is widely used today. Their works were based on an educated guess on tangential surface with stick zone. The theory has been validated by fretting experiments [Mindlin, 1952], [Johnson, 1955].

Because it is very important in modeling fretting contact problem, we briefly introduce Cattaneo-Mindlin problem first:

Suppose an elastic sphere with radius R contacts against an elastic half-space with identical material, the contact conditions fulfill all the Herzian assumptions except that there is friction between surfaces and tangential force is exerted. Hertzian theory predicts the normal traction arises as the result applied normal load P :

$$p(r) = p_0 \sqrt{1 - \left(\frac{r}{a}\right)^2}, \quad r \leq a \quad (13.2)$$

where p_0 is the maximal normal traction, which occurs at the center of contact area:

$$p_0 = \frac{3P}{2\pi a^2} \quad (13.3)$$

and a is the radius of contact area:

$$a = \sqrt[3]{\frac{1-\nu^2}{E} \frac{3PR}{4}} \quad (13.4)$$

When a tangential load $Q_x < \mu P$ is applied, the shear traction in slip zone is related to normal traction by Coulomb's friction law:

$$q(r) = \mu p(r) = \mu p_0 \sqrt{1 - \left(\frac{r}{a}\right)^2}, \quad c \leq r \leq a \quad (13.5)$$

where c is the radius of stick zone.

In stick zone, the shear traction is the superposition of two parts, written as:

$$\begin{aligned}
 q_x(r) &= \mu p_0 \sqrt{1 - \left(\frac{r}{a}\right)^2} - \mu p_0 \frac{c}{a} \sqrt{1 - \left(\frac{r}{c}\right)^2} \\
 &= \mu p_0 \left(\sqrt{1 - \left(\frac{r}{a}\right)^2} - \frac{c}{a} \sqrt{1 - \left(\frac{r}{c}\right)^2} \right), c \leq r \leq a
 \end{aligned}
 \tag{13.6}$$

By applying the equilibrium condition along X- direction, the following relationship is obtained:

$$\frac{c}{a} = \sqrt[3]{1 - \frac{Q}{\mu P}}
 \tag{13.7}$$

Figure 13.1 shows the plot of surface traction distribution of Cattaneo-Mindlin problems. The Cattaneo-Mindlin's solution is accurate only when Poisson's ratio is zero. Munisamy, et al. [Munisamy, Hill, and Nowell, 1994] studied the contact problem with non-zero Poisson's ratio. They found that relative transverse displacements result within slip zone and are maximized along the lines $y = \pm x$.

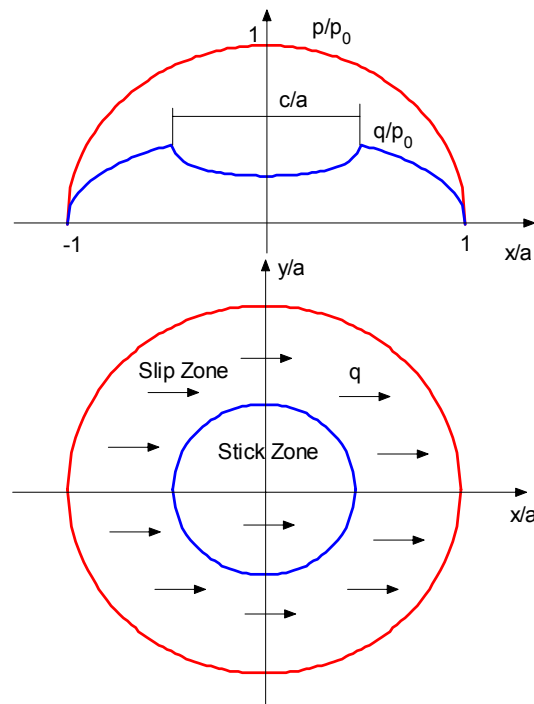


Figure 13.1 Cattaneo-Mindlin's Solution

13.1.2 Numerical Example

The following example comes from a fretting fatigue experiment [Tur, Fuenmayor and Rodenas, 2002]. Two pads with sphere top are push against the specimen having rectangular cross-section. The force F is applied to specimen while force N is applied to each pad. Both sphere and foundation are made of aluminum alloys. The slip zone and maximal shear traction are to be found. The problem is modeled as the following contact problem: an elastic body is in

contact with elastic foundation. The material properties and geometry data are listed in Table 13.1.

Table 13.1 Contact Configuration Data

Parameter	E (10 ⁹ N/m ²)	ν	μ	P (N)	Q (N)	Radius (m)
Sphere	71.1	0.33	1.2	1000	10800	0.050
Foundation	71.1	0.33				Infinity

Table 13.2 Loading Step

Step No.	1~10	11~37	Total	Note
ΔP (N)	100	0	1000	
ΔQ_x (N)	0	40	10800	

The computation shows that when only normal load increments ΔP is applied (step No. 1~10), both contact zone and surface normal traction increase monotonically. The whole contact area is in stick, no slip takes place. Then, when tangential load increment ΔQ is applied, a slip ring appears from the contact boundary, all the points with which have the same slip direction. Along with the applying of increments ΔQ , the slip zone grows in size towards center. The contact zone, stick and slip area keep the property of axi-symmetry.

Figure 13.2(a)~(h) are the plots of the result comparing with Cattaneo-Minlin's solution. It is clear that the numerical results are very close to analytical solution.

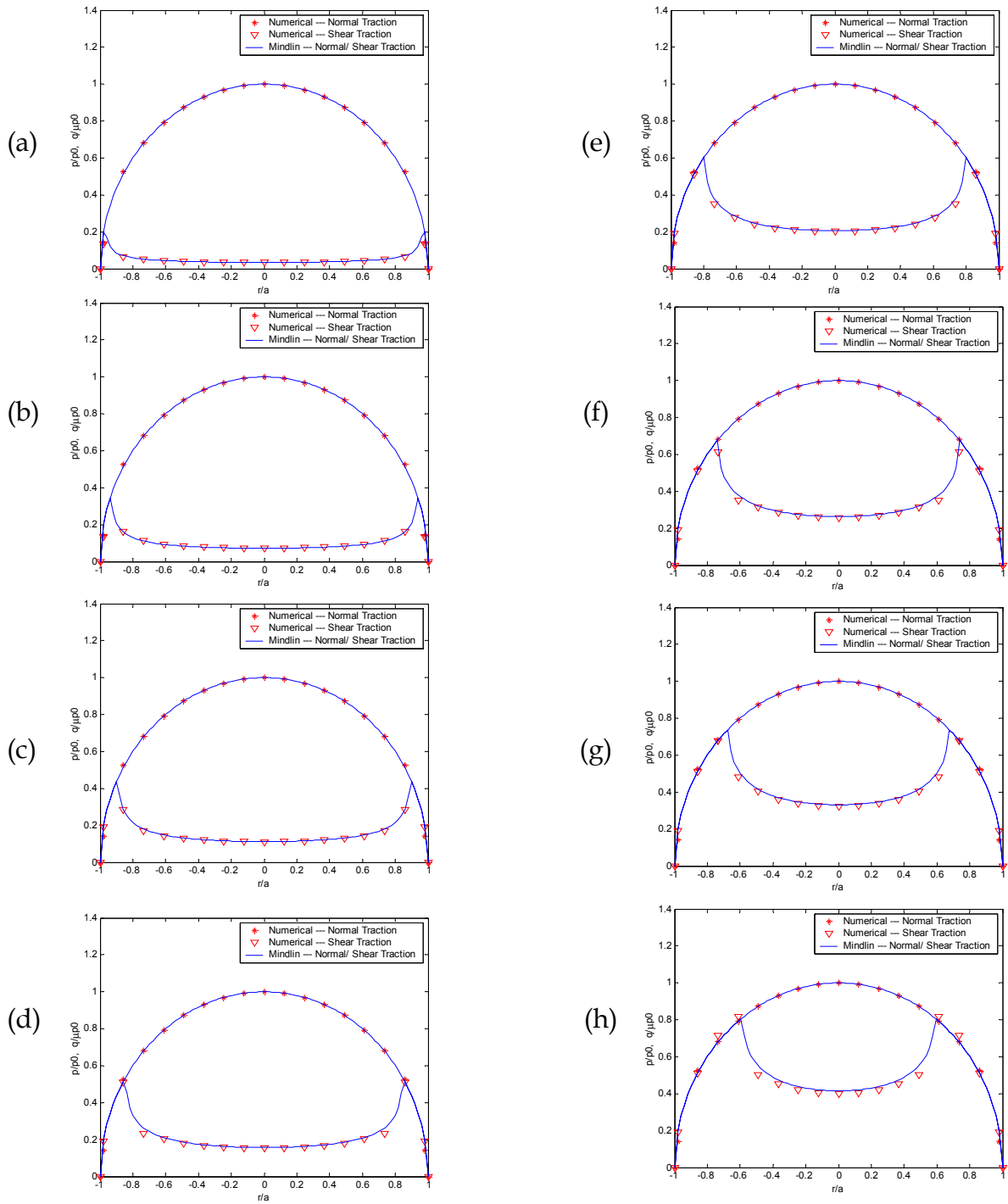


Figure 13.2 Numerical Results Compare with Cattaneo-Minlin's Solution, Along X-Direction

Figure	(a)	(b)	(c)	(d)	(e)	(f)	(g)	(h)
Step	13	16	19	22	25	28	31	34
$Q / \mu P$	0.1	0.2	0.3	0.4	0.5	0.6	0.7	0.8

The result shows that the numerical solution is valid for similar material contact problems. Our results also show that when Poisson's ratio is not zero, there exists transverse shear traction; while in Mindlin's solution, there is no transverse shear traction because it is based on the assumption that Poisson's ratio is zero.

13.2 Contact Problem with Dissimilar Materials

Next, we consider the contact problems with dissimilar material. We first briefly examine previously studied cases in this category, then present a case and compare the computational result with these cases.

13.2.1 Nowell, Munisamy and Hill's works

Nowell et al. [Nowell and Hill, 1988] studies the contact problem of dissimilar elastic cylinders under normal and tangential loading. Unlike the result predicted by Mindlin's solution, the distribution of shear traction is skew-symmetric when there is no tangential force is applied. Further, when tangential force is monotonically applied, the stick zone becomes irregular in shape and shift in the direction of tangential force (see Figure 13.3).

Munisamy, et al. [Munisamy, Hill, and Nowell, 1994] examined the axisymmetric Hertzian contact subject to shearing forces. They employed Goodman approximation to decouple normal and tangential tractions. The normal traction

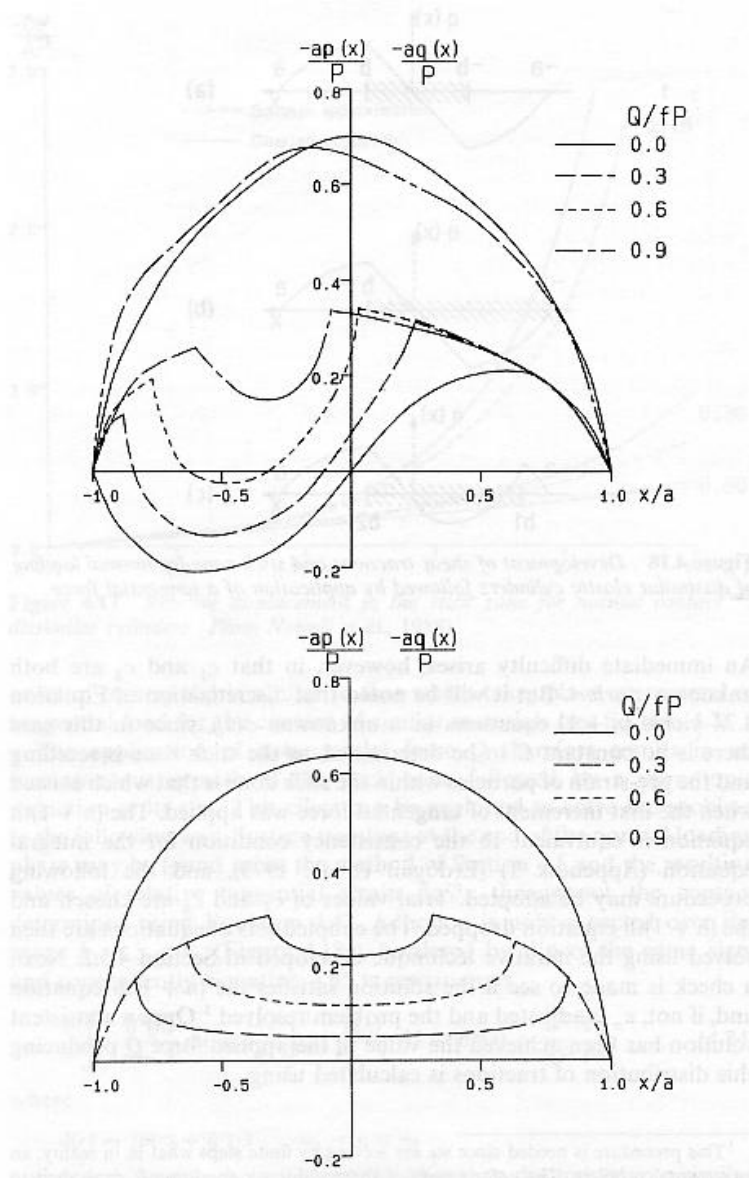


Figure 13.3 The Analytical Solutions for 2-D Cases. (Above) Solution to Dissimilar Materials Obtained from Goodman's Approximation, It Shows That the Shape and Location of Stick Zone Change When Tangential Force Is Applied; (Bottom) Mindlin's Solution for Similar Materials (From [Hills, Nowell, and Sackfield, 1993])

was predicted by Hertzian solution. Then, they discretized the contact into a mesh of squares, uniform traction elements of unknown magnitudes $q_{x,i}, q_{y,i}$; the governing integral equations were linearized into algebraic equations. Their numerical result showed that:

- (1) In elastically similar cases, if Poisson's ratio is not zero, the transverse shear traction is not negligible;
- (2) The elastic dissimilarity (measured by parameter β) has remarkable effect on bulk relative shear displacement (see Figure 13.4);
- (3) Tangential force will dramatically change the distribution of shear tractions, and both the shape and location of stick zone (see Figure 13.5).

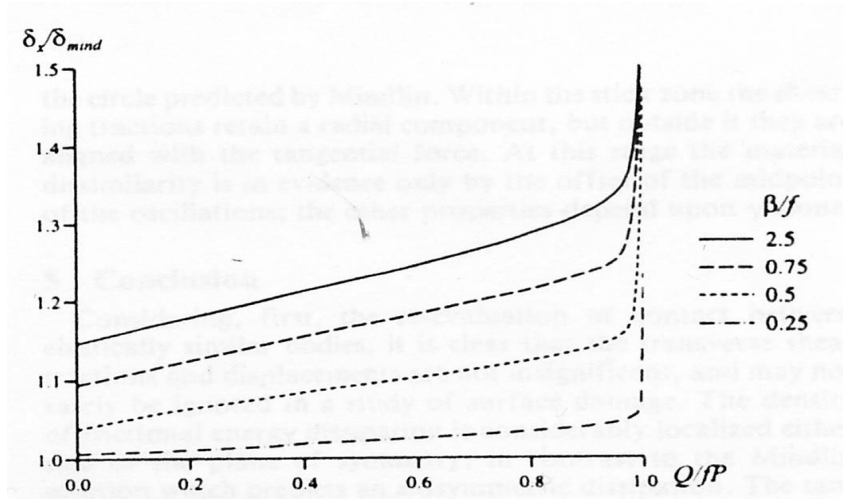


Figure 13.4 Initial Tangential Compliance of the Numerical Scheme Compared with Mindlin's Approximation (From [Munisamy, Hill, and Nowell, 1994]). δ_x Is the Bulk Relative Shear Displacement, δ_{mind} Is the Value Given by Mindlin's Approximation

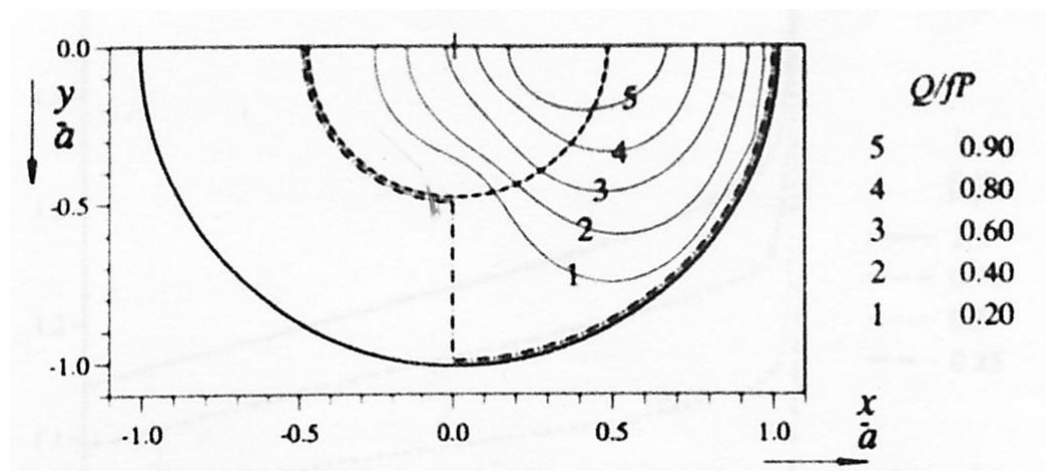


Figure 13.5 Evolution of Stick Zone for Contact Between Dissimilar Elastic Materials. Dashed Line Corresponds to Normal Loading Alone and Chain Line to a Subsequent Infinitesimal Tangential Force (From [Munisamy, Hill, and Nowell, 1994]).

13.2.2 Numerical Example

As a case to show the capability of the numerical solution, we examine the problem that we used in Chapter 9: an elastic (with relatively high Young's modulus) indenter with a sphere top contacts an aluminum foundation. The only difference is that in addition to normal force P , a tangential force Q is also applied to the indenter. The material properties and geometry data are listed in Table 13.3.

Table 13.3 Contact Configuration Data

Parameter	E (10^9N/m^2)	ν	μ	P (N)	Q (N)	Radius (m)
Sphere	432	0.32	0.1	31.5	3	0.001
Foundation	72	0.32				Infinity

Table 13.4 Loading Schedule

Step No.	1~10	11~40	Total	Note
ΔP (N)	3.15	0	31.5	
ΔQ_x (N)	0	0.1	3	

Again, we apply normal force first, then tangential force. In order to simulate the loading procedure as accurately as possible, we use relatively small increments for tangential load. The schedule of loading steps is shown in Table 13.4.

It is observed that in the first 10 steps (when only normal force applied), both the contact area and normal traction increase monotonically (Figure 13.6). However, the relationships are not linear. It was found that even though there is no tangential force applied, the slips take place within contact area Figure 13.7(a); further, unlike similar material case, the shear traction is positive in one half but negative in another half - skew-symmetric. When tangential load increments applied, the shape of stick zone and the distribution of shear traction change dramatically.

First, we examine the situation when only normal force is applied. Comparing the result we obtained here with the result from non-incremental algorithm (see Table 13.5), it can be concluded that: for a normal contact problem (no tangential force applied), both non-incremental and incremental solution (with monotonic increments) give excellent results, comparing with analytical solution.

Next, we examine the contact behavior when tangential increments are applied. From loading step No. 11 to No. 35, no more normal force applied; the tangential force applied with the same increments: 0.1N. It is worthy to give special attention to step no.11, in which only a small amount of tangential force is applied. The stick/slip zones, however, change dramatically Figure 13.7(b)), the right side of stick boundary reaches the contact boundary, the stick zone becomes very large and the shape becomes irregular.

Table 13.5 Comparison Among Non-incremental, Incremental and Spence Solution

Parameters Solutions	Background Mesh	Maximal normal traction p_{\max} (10^9N/m^2)	Contact Radius a (10^{-5}m)	Stick Radius c (10^{-5}m)	c / a
Non- incremental	41×41	3.16380	6.843		0.533
Incremental	21×21	3.211257	6.966087	3.541842	0.508
Spence					0.535

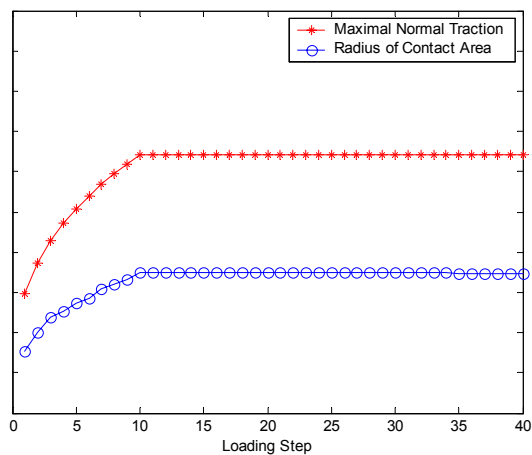


Figure 13.6 The History of Contact Area and Normal Traction

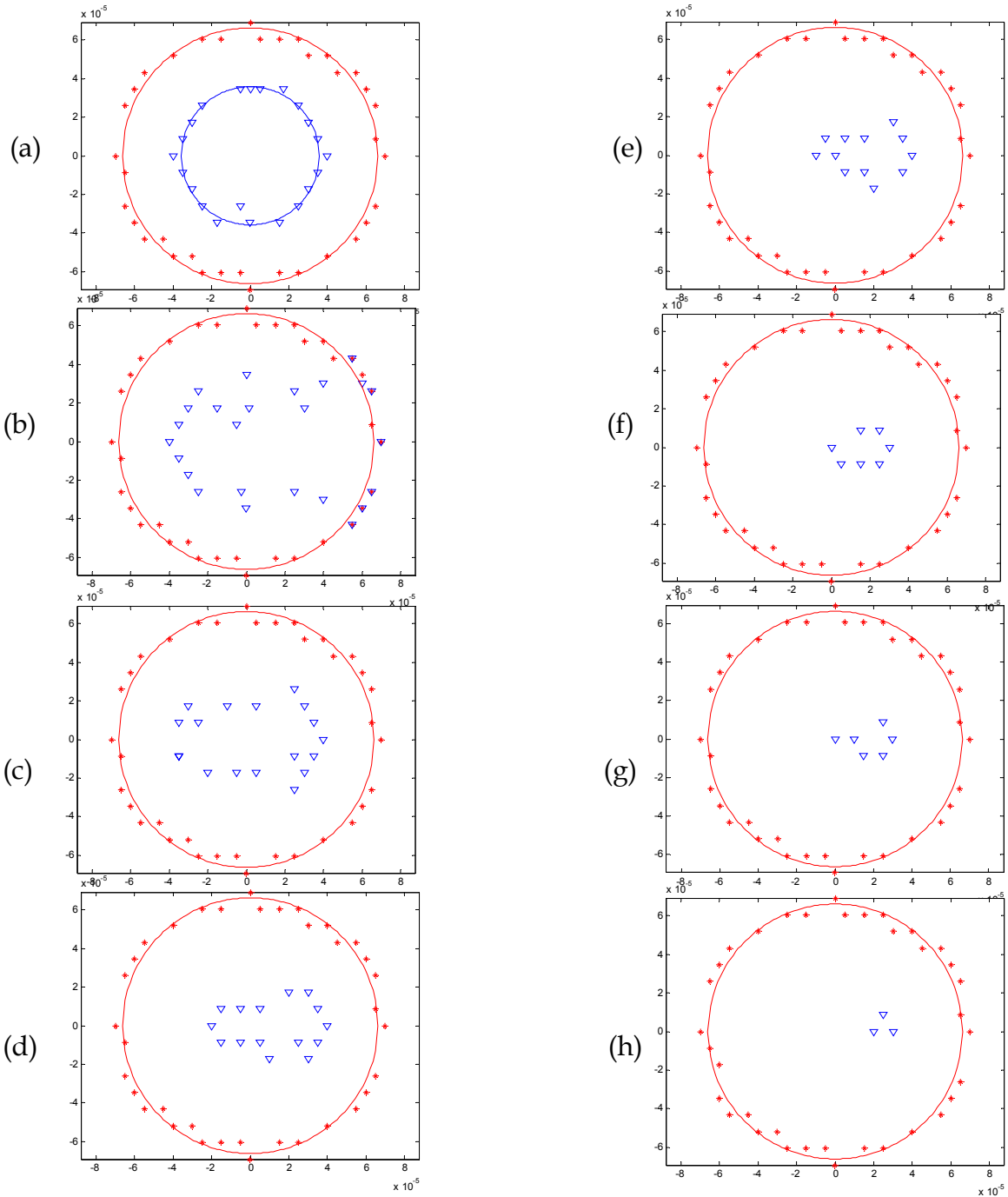


Figure 13.7 History of Contact and Stick Area, * -- Nodes Immediately Inside Contact Boundary; ∇ -- Nodes Immediately Inside Stick Boundary; Solid Line -- Curve fit of Nodes

Figure	(a)	(b)	(c)	(d)	(e)	(f)	(g)	(h)
Step	10	11	12	15	20	25	30	35
Q / μP	0	0.0317	0.0635	0.1587	0.3175	0.4762	0.6349	0.7937

At next step, the stick zone leaves contact boundary and begins to shrink, the shape is still irregular. The stick zone keeps shrinking all the way to about $Q/\mu P \approx 0.9$, after that, the entire contact area is in slip condition. In the procedure, the shape becomes more and more like ellipse. However, it is no longer located at center as the normal contact cases (Figure 13.7(c-h)).

Compare the numerical result with Munisamy et al.'s result, we can see that Figure 13.7(a-h) yields similar information as their result (Figure 13.5) in three aspects: (1) The initial shapes of contact and stick zones (before tangential force is applied); (2) The shape change of stick zone along with $Q/\mu P$; (3) The Location change of stick zone along with $Q/\mu P$. While Munisamy's solution is based on Goodman's approximation, but the case they chose fulfills the criterion: $\beta\mu < 0.1$, which is believed can yield good result. Our method has no such restriction, but the case we chose fulfills the criterion also: $\beta\mu = 0.017$. Therefore, it is reasonable to use Munisamy's solution to serve the validation purpose.

There is still no analytical solution available for 3-D fretting contact with dissimilar materials, and the numerical result is not perceptible intuitively.

However, the result we obtained can be illustrated as follows:

For the purpose of clarity, we look at the section-cut view of surface traction distribution (Figure 13.8). Before any tangential force is applied, there exist two

slip zones with opposite shear tractions: $(-a, -c)$ and (c, a) ; the stick zone $(-c, c)$ at the center surrounded by slip zones. When an increment ΔQ is applied, it must be balanced by the rearrangement of surface shear traction. It causes the shear traction in one slip zone (right side) to decrease in magnitude and increase in another (left side). Therefore, one side (right) becomes stick instantaneously because $|q| < \mu p$, while the other side (left) increase slip area due to the increased shear traction $q > \mu p$, which violates Coulomb's friction law.

After a certain amount of tangential force is applied, the shear traction in left side will change direction and grows in magnitude, and new slip with the same direction as the other slip zone appears in the side. On the other hand, the size of another slip zone keeps growing when gradually increasing tangential force. As the result, the stick zone can no longer stay at the center of contact area.

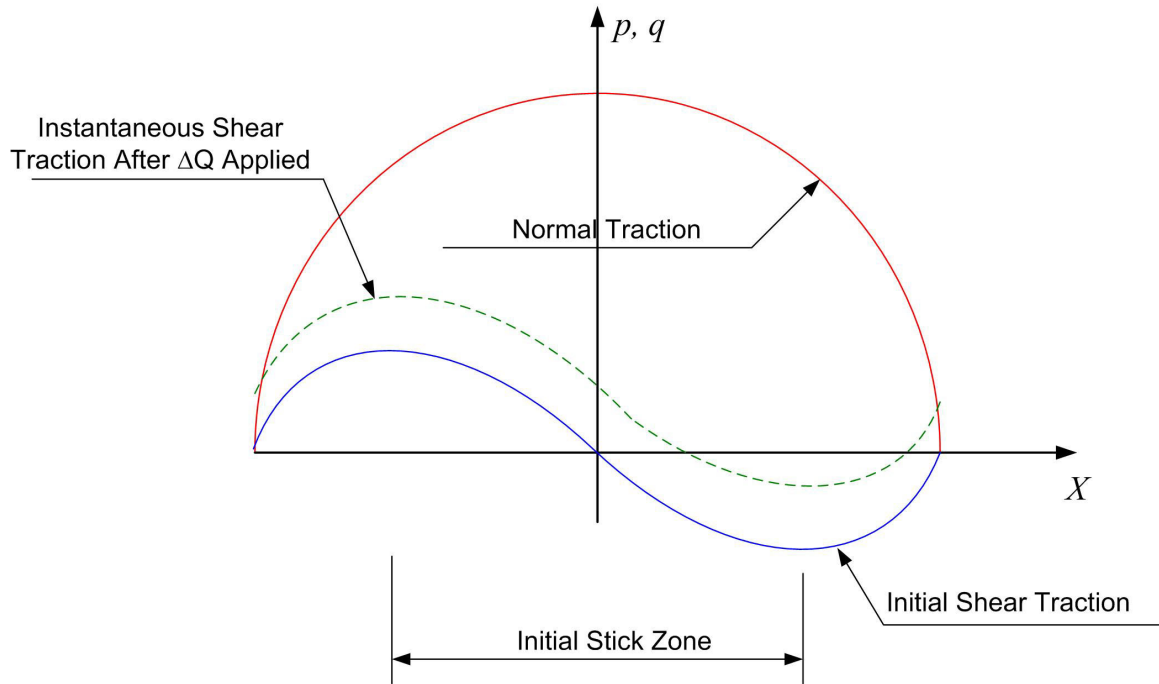


Figure 13.8 The Illustration of the Change of Stick Zone

Chapter 14

Discussion and Conclusion

In this part, an incremental algorithm has been developed to accommodate 3-D frictional contact problem with tangential forces. Because friction force is path-dependent, the frictional contact problem is treated as a dynamic model. In most of the cases that the acceleration is not significant, the inertial force can be ignored, and quasi-static model is adopted. One of the most popular ways to deal with quasi-static problem is incremental method. The incremental algorithm presented here also follows the concept of superposition of pyramid loading element to approximately achieve C^0 continuity presentation of actual traction distribution. The case studies show this method has been successfully used in both non-incremental and incremental algorithm, yielding excellent result comparing with analytical solution and previously available numerical solution.

The contact detecting and stick/slip partitioning algorithm are much more complicated than non-incremental formula. For each loading step, the system equations are assembled and solved in a similar way as non-incremental solution. However, the contact area keeps shrinking during the iterations in non-incremental solution, while incremental solution allows expanding and shrinking. The partition of stick and slip zone allows stick and slip nodes to

change between two statuses. The algorithm and corresponding numerical framework have been examined and validated against analytical solutions, using several example cases. The results show that:

- (1) For the frictional normal contact cases (only normal force applied), the algorithm gives the results very close to those from non-incremental solution, as well as Spence' s analytical solution.
- (2) For the frictional contact problems with similar materials, the algorithm gives the result very close to Cattaneo-Mindlin's analytical solution in the whole range from $Q/\mu P = 0 \sim 0.9$. For the tangential load $Q/\mu P > 0.9$, the solution gives the result that whole contact region is in slip, or only 1~2 nodes in stick. The author expects that the result can be further improved by increasing the density of background mesh.
- (3) For the frictional contact problems with dissimilar materials, we use the work by Munisamy, et al [Munisamy, et al, 1994]. to validate the algorithm and numerical framework. It is found that our results are very close to theirs. The comparison gives the confidence that the numerical solution reflects the real mechanism of contact. Further, Nowell and Hill have done analytical solution for a 2-D plain strain case [Hill, Nowell & Sackfield, 1993]. Their results for two elastic cylinders can be used to compare with our result in a analogous manner. It is also found that stick/slip zones behaviors in a way similar to 2-D contact problem.

Reference

Alart, P., Curnier, P., 1986, Contact discret avec frottement: unicite de la solution convergence de l'algorithme, *Document, Laboratoire de mecanique appliquee, Ecole Polytechnique Federale de Lausanne, Lausanne*

Andersson, L.-E., 1991, A quasistatic frictional problem with normal compliance, *Nonlinear Analysis*, 16, 347-369

Andersson, L.-E., 1995, A global existence result for a quasistatic contact problem with friction, *Advanced Materials Science and Applications* , 5, 249-286

Andersson, L.-E., 1999, A quasistatic frictional problem with a normal compliance penalization term, *Nonlinear Analysis*, 37, 689-705

Atluri, S. N., Kim, H. G. and Cho, J. Y., 1999, A critical assessment of the truly mesh less local pttrov-galerkin (mlpg) and local boundary integral equation(lbie) methods, *Computational Mechanics*, 24, 348-372

Babuska, I. and Melenk, J. M. , 1997, The partition of unity method, *International Journal for Numerical Methods in Engineering*, 40, 727-758

Barber, J. R., Ciavarella, M., 2000, Contact Mechanics, *International Journal of Solids and Structures*, 37, 29-43

Bryggman, U. and Sodererg, S. , 1986, Contact conditions in fretting, *Wear*, 110, 1-17

Campos, L. T., Oden, J. T. and Kikuchi, N. , 1982, A numerical analysis of a class of contact problems with friction in elastostatics, *Computer Methods in Applied Mechanics and Engineering*, 34, 821-845

Cattaneo, C., 1938, Sul contatto di due corpi elastici Distribuzione locale degli sforzi, *Reconditi dell Accademia Nazionale dei Lincei*, 27, 342-348, 434-436, 474-478

Ciavarella, M. , 1998a, The generalized cattaneo partial slip plane contact problem -- theory, *International Journal of Solids and Structures*, 35(18), 2349-2362

Ciavarella, M. , 1998b, Tangential loading of general three-dimensional contacts, *ASME Journal of Applied Mechanics*, 65, 998-1003

Cocus, M., 1984, Existence of solutions of Signorini problems with friction, *International Journal of Engineering Science* , 22, 567-575

Demkowicz, L., Oden, J. T., 1982, On some existence and uniqueness results in contact problems with non-local friction, *Nonlinear Analysis*, 6, 1075-1093

Duarte, C. and Oden, J. T. , 1996, Hp-cloud: A mesh less method to solve boundary-value problems, *Computer Methods in Applied Mechanics and Engineering*, 139, 237-262

Duvaut, G., Lions, J. L., 1976, Inequalities in mechanics and physics, *Springer, Berlin*

Dydo, J. R. and Busby, H. R. , 1995, Elasticity solutions for constant and linearly varying load applied to a rectangular surface patch on the elastic half-space, *Journal of Elasticity*, 38, 153-163

Eterovic, A. L. & Bathe, K. J., 1991, On the treatment of inequality constraints arising from contact conditions in finite element analysis, *Computers and Structures*, 40, 203-209

Fujimoto, T., Kagami, J., Kawaguchi, T., Hatazawa, T., 2000, Micro-displacement characteristics under tangential force, *Wear*, 241, 136-142

Goodman, L. E. , 1962, Contact stress analysis of normally loaded rough spheres, *ASME Journal of Applied Mechanics*, 29, 515-522

Guyot, N. Kosior, F. and Maurice, G., 2000, Coupling of finite elements and boundary elements methods for study of the frictional contact problem, *Computer Methods in Applied Mechanics and Engineering*, 181, 147-159

Hertz, H. , 1897, On the contact of elastic bodies, *J. reine und angew Math*, 92, 56-57

Hills, D. A. and Sackfield, A. , 1987, The stress field induced by normal contact between dissimilar spheres, *ASME Journal of Applied Mechanics*, 54, 8-14

Hills, D. A., and Mugadu, A., 2002, An overview of progress in the study of fretting fatigue, *Journal of Strain Analysis*, v37, n6, 591-601

Hills, D. A., Nowell, D. and Sackfield, A. , 1993, *Mechanics of Elastic Contacts*, Butterworth-Heinemann Ltd

Hills, D. A., Nowell, D. & O'Connor, J. J. , 1988, On the mechanics of fretting fatigue, *Wear*, 125, 129-146

Janovasky, V., 1980, Catastrophic features of Coulomb friction model, *Technical*

Report KNM-0105044/80, Charles University, Prague

Janovasky, V., 1981, Catastrophic features of Coulomb friction model, *The mathematics of finite elements and applications, Academic Press, London*, 259-264

Jaruusek, J., 1983, Contact problems with bounded friction, *Coereive case. Czecheslovak Math. J.*, 33, 237-261

Johnson, K. L., 1955, Surface interactions between elastically loaded bodies under tangential forces, *Proceedings of the Royal Society(London)*, A230, 531-548

Johnson, K. L., 1961, Energy dissipation at spherical surfaces in contact transmitting oscillating forces, *Journal of Mechanical Engineering Science*, 3(4), 362-368

Johnson, K. L., 1985, Contact Mechanics, *Cambridge Unicersity Press, Great Britain*

Kalker, J. J. and van Randen, Y. , 1972, A minimum principle for frictionless elastic contact with application to non-Hertzian half-space contact problems, *Journal of Engineering Mathematics*, 6(2), 193-206

Kato, Y., 1987, Signorini's problem with friction in linear elasticity, *Journal of*

Applied Mechanics(Japan), 4, 237-268

Kikuchi, N. & Oden, J. T., 1988, Contact Problems in Elasticity: A Study of Variational Inequalities and Finite Element Methods, *Society for Industrial and Applied Mathematics, Philadelphia*

Klarbring, A., 1990, Derivation and analysis of rates boundary-value problems of frictional contact , *European Journal of Mechanics*, A1, 53-85

Klarbring, A., Mikelic, A., Shillor, M., 1990, Duality applied to contact problems with friction, *Applied Mathematics and Optimization*, 22, 211-226

Klarbring, A., 1984, Contact problems with friction - using a finite-dimensional description and the theory of linear complementarity, *Linkoping Studies in Science and Technology, Linkoping Institute of Technology, Linkoping, Sweden*, Thesis No.20

Klarbring, A., 1987, Contact problems with friction by linear complementarity, *Unilateral problems in structural analysis*, 2, 197-219

Klarbring, A., 1990, Examples of non-uniqueness and non-existence of solutions to quasistatic contact problems with friction, *Ingenieur-Archiv*, 60, 529-541

Klarbring, A., 1986a, General contact boundary conditions and the analysis of frictional systems, , *International Journal of Solids and Structures*, 22(12), 1377-1398

Klarbring, A., 1986b, A mathematical programming approach to three-dimensional contact problems with friction, *Computer Methods in Applied Mechanics and Engineering*, 58, 175-200

Klarbring, A., Mikelie, A., Shillor, M., 1988, Frictional contact problems with normal compliance, *Nonlinear Analysis*, 13, 935-955

Kosior, F. Guyot, N. and Maurice, G., 1999, Analysis of frictional contact problem using boundary element method and domain decomposition method, *International Journal for Numerical Methods in Engineering*, 46, 65-82

Lancaster, P. & Salkauskas, K., 1981, , Surfaces generated by moving least squares methods, *Mathematics of Computation*, 37, 141-158

Lancaster, P. and Salkauskas, K., 1981, Surfaces generated by moving least squares methods, *Mathematics of Computation*, 37, 141-158

Li, J., 2000-2002, CAE reports, *Computer-Aided Engineering Laboratory, University of Cincinnati*

Li, J. and Berger, E. J., 2001, A Boussinesq-Cerruti solution set for constant and linear distribution of normal and tangential load over a triangular area, *Journal of Elasticity*, 63, 137-151

Li, J. and Berger, E. J., 2003, A semi-analytical approach to three-dimensional normal contact problems with friction, *Computational Mechanics*, v30, 310-322

Li, S., Qian, D., Liu, W.-K. & Belytschko, T., 2001, A mesh-free contact-detection algorithm, *Computer Methods in Applied Mechanics and Engineering*, 190, 3271-3292

Litewka, P. & Wriggers, P., 2002, Frictional contact between 3D beams, *Computational Mechanics*, 28, 26-39

Love, A. E. H., 1927, *A Treatise on the Mathematical Theory of Elasticity*, 4th edition, Cambridge University Press

Love, A. E. H., 1929, The stress produced in a semi-infinite solid by pressure on part of the boundary, *Philosophical Transactions of the Royal Society, London*, A228:377

Martin, J. A. C., Oden, J. T., 1987, Existence and uniqueness results for dynamic contact problems with nonlinear normal and friction interface laws, *Nonlinear*

Analysis, 11, 407-428

McVeigh, P. A., Farris, T. N., 1997, Finite Element analysis of fretting stresses, *Journal of Tribology*, 119, 797-801

Mindlin, R. D., 1949, Compliance of elastic bodies in contact, *ASME Journal of Applied Mechanics*, 16, 259-268

Mindlin, R. D. and Dereciwicz, H., 1953, Elastic spheres in contact under varying oblique forces, *ASME Journal of Applied Mechanics*, 20, 327-344

Mindlin, R. D., Mason, W. P., Osmer, T. F. and Dereciwicz, H., 1952, Effect of an oscillatory tangential force on the contact surfaces of elastic spheres, *Proceedings of the First National Congress of Applied Mechanics*, , 203-208

Mitsopoulou, E. N., Doudoumis, I. N., 1987, A contribution to the analysis of unilateral contact problems with friction, *Solid Mechanics Archives*, 12, 165-186

Munisamy, v, Hills, D. A. and Nowell, D., 1994, Static axisymmetric Hertzian contacts subject to shearing forces, *ASME Journal of Applied Mechanics*, 61, 278-283

Necas, J., Jarusek, J., Haslinger, J., 1980, On the solution of the variational

inequality to the Signorini problem with small friction, *Bolletino UMI*, 5, 796-811

Oden, J. T. & Pires, E. B., 1983, Non-local and nonlinear friction laws and variational principles for contact problems in elasticity, *Journal of Applied Mechanics*, 50, 67-76

Oden, J. T. and Martins, J. A. C., 1984, Models and computational methods for Dynamic Friction Phenomena, *Computer Methods in Applied Mechanics and Engineering*, 52, 527-634

Pantuso, D., Bathe, K. J. & Bouzinov, P. A., 2000, A Finite element procedure for the analysis of thermo-mechanical solids in contact, *Computers and Structures*, 75, 551-573

Paris, F. & Garrido, J. A., 1989, An incremental procedure for friction contact problems with the boundary element method, *Engineering Analysis with Boundary Elements*, 0006(4), 202-213

Rabier, P. J. & Oden, J. T., 1987, Solution to Signorini contact problems through interface models - I. Preliminaries and formulation of a variational equality, *Nonlinear Analysis*, 11, 1325-1350

Rabier, P. J. & Oden, J. T., 1988, Solution to Signorini contact problems through interface models - II. Existence and uniqueness theorem, *Nonlinear Analysis*, 12, 1-17

Rabier, P., Martins, J. A. C., Oden, J. T. & Campos, L., 1986, Existence and local uniqueness of solutions to contact problems in elasticity with nonlinear friction laws, *International Journal of Engineering Science*, 24(11), 1755-1768

Rajeev P. T., and Farris, T. N., 2002, Numerical analysis of fretting contacts of dissimilar isotropic and anisotropic materials, *Journal of Strain Analysis*, v37, n6, 503-517

Saeedvafa, M. & Dundurs, J., 1988, An example for load-path dependence in elasticity with friction, *Journal of Theoretical and Applied Mechanics*, 7(2), 211-226

Soderberg, S., Bryggman, U. and McCullough, T., 1986, Frequency effects in fretting wear, *Wear*, 110, 19-34

Spence, D. A., 1968, Self-similar solutions to adhesive contact problems, *Proceedings of the Royal Society (London)*, A305(1480), 55-80

Spence, D. A., 1975, The Hertz contact problem with finite friction, *Journal of*

Elasticity, 5(3-4), 297-319

Spence, D. A., 1985, Frictional contact with transverse shear, *Journal of mechanics and applied mathematics*, v39, Pt. 2, 233-251

Svec, O. J. and Gladwell, G. M. L., 1971, AN explicit Boussinesq solution for a polynomial distribution of pressure over a triangular region, *Journal of Elasticity*, 1, 167-170

Szolwinski, M. P., Farris, T. N., 1996, Mechanics of fretting fatigue Crack formation, *Wear*, 198, 93-107

Tur, M. Fuenmayor, J., and Rodenas, J. J., 2002, Influence of bulk stress on contact conditions and stress during fretting fatigue, *Journal of Strain Analysis*, v37, n6, 479-492

Vingsbo, O. and Soderberg, S., 1988, On fretting maps, *Wear*, 126, 131-147

Waterhouse, R. B., 1992, Fretting fatigue, *International Materials Review*, 37(2), 77-97

Young, W. C., 1989, Roark's Formulas for Stress and Strain, sixth edition,

McGraw-Hill, Inc., New York

Zavarise, G., Wriggers, P. & Schre^oer, A, 1998, A method for solving contact problems, *International Journal for Numerical Methods in Engineering*, 42, 473-498